Effects of the Post-Heat Treatment (Furnace Cooling) on the mechanical strength and dimensional accuracy of 3D printed PEEK in FDM method

Yunxiang Deng

A thesis submitted in fulfilment of the requirements for the degree Doctor of Philosophy

School of Aerospace, Mechanical and Mechatronic Engineering

Faculty of Engineering

University of Sydney

May 2026

Statement of Originality

This is to certify that the content of this thesis is my own work. This thesis has not been submitted for any other degree or purpose.

I certify that the intellectual content of this thesis is the product of my own work, and that all assistance received in preparing this thesis and all sources have been acknowledged.

Yunxiang Deng

Acknowledgement

The present work was completed between July 2022 and February 2026 at the University of Sydney, Australia.

First and foremost, I would like to express my gratitude and appreciation to Dr Li Chang for the research and scientific support and concerns regarding my research progress. Without his strong support, it would be impossible to perform this thesis. During the research period, it was Dr Li Chang who trained me as an independent qualified researcher to properly complete the period of one decent project from the initial stage of thinking to the final revision of the manuscript.

Secondly, I would like to thanks to the research fellow of Dr Boyang Wan for the help on the finite element analysis of the proposed experimental model. Many thanks to Dr Hanyu Li and Yu Zhao for their help on the microscopy analysis and vibration signal processing.

My special thinks to the technical staff who provided me lots of help in the laboratories. They are Dr Shaocong Dai and Dr Hongjian Wang from the material labs. Dr Mehdi Eizadjou and Dr Wen Hao Kan from the Sydney Manufacturing Hub (SMH).

I am grateful to the University of Sydney for having me this opportunity of researching in this excellent environment. I would like to express my appreciation to the faculty staff for their efficient and friendly support to my research.

Also, I acknowledge the use of [ChatGPT (GPT 5.5), OpenAI, https://chatgpt.com] to perform a grammar check in Chapter 1.1, Chapter 1.3–1.5, and Chapter 7 Conclusions and Outlook.

Finally, this work is dedicated to my parents for their patience and support.

Sydney, February 2026

Yunxiang Deng

Authorship Attribution Statement

Chapter 3 of this thesis has been published as [**Y. Deng**, and L. Chang, "Effects of Post-Heat Treatment on Mechanical and Tribological Properties of 3D-Printed PLA and PEEK Structures," Polymers 2026, Vol. 18, vol. 18, no. 2, p. 253, Jan. 2026, doi: 10.3390/POLYM18020253.]. I designed the study, obtained the experimental data, and wrote and revised the draft of the manuscript.

Chapter 4 of this thesis has been published as [**Y. Deng**, Y. Zhao, B. Wan, and L. Chang, "Effects of re-entrant auxetic structure on friction-induced vibrational behaviour of 3D printed PLA in sliding wear process," Friction, Aug. 2025, doi: 10.26599/FRICT.2025.9441172.] I designed the study, obtained the experimental results, and wrote the drafts of the manuscript.

Chapter 5 of this thesis currently has submitted to the Journal of Tribology International [**Y. Deng**, B. Wan, H. Li, Y. Zhao, L. Chang, "Reducing Friction-induced Vibration and Wear of Carbon Fiber Reinforced PLA Composites with the Re-entrant Auxetic Structure using 3D Printing Technology"]. Beside Chapter 5.1, I designed and performed the experiments, interpreted data and wrote the manuscript.

Conference Paper

Y. Deng, and L. Chang, Effects of the Post-heat Treatment on Mechanical and Tribological behaviour of 3D Printed PEEK. 4th Asia-Pacific International Conference on Additive Manufacturing (APICAM), Melbourne, Australia, 30 June to 3 July 2025.

In addition to the authorship attribution statements above, in cases where I am not the corresponding author of a published item, permission to include the published material has been granted by the corresponding author.

[Yunxiang Deng, 09-02-2026]

As supervisor for the candidature upon which this thesis is based, I can confirm that the authorship attribution statements above are correct.

[Li Chang, 09-02-2026]

Abstract

In recent decades, the production of polymeric parts using fused deposition modelling (FDM) has gained significant attention in the field, owing to its design flexibility, low cost, and time-efficient prototyping capabilities. Nevertheless, the inherently as-built limitation constrains the performance and challenges the broader applications. To address these limitations, the post-heat treatment or annealing has long been applied as one the critical post processing techniques for enhancing the materials properties and its performance. Despite the beneficial effects of the post-heat treatment on the mechanical strength, its effect on the long-term tribological performance with the involvement of complex structures are limited. While it is often assumed that improvements in mechanical properties lead to enhanced tribological performance, tribological properties are not intrinsic material properties. Instead, they are instead dependent strongly on the specific system and operating conditions in which a material or structure has to function. Among the tribological studies, the friction-induced vibration (FIV) is a critical issue, causing unwanted noise, wear, and potential system failure. Although the proposed active or passive controls can mitigate FIV, they inevitably increase the complexity in the design and implementation of the whole system. The re-entrant auxetic structure was employed in this study as the solution, characterized by Negative Poisson's ratio (NPR). Notably, the performance of AM-fabricated parts remains highly sensitive to the external environmental stimuli, particularly temperature.

Therefore, this thesis systemically investigated the effects of post-heat treatment on the dimensional accuracy, mechanical performance and tribological performance of FDM-printed polymers and polymers composites incorporating with complex structures under environmental temperature conditions. This work of great importance as it demonstrates the post-heat treatment is an effective method for tailoring and optimizing the mechanical behaviour of printed polymers while also emphasizing the necessity of systematically evaluating its influence on the tribological performance of printed engineering parts subjected to different sliding conditions and thermally demanding conditions.

This thesis started from comprehensive exploration on the effects of post-heat treatment on the mechanical performance by measuring the tensile and compressive strength of the FDM-printed neat PLA and PEEK. It was found that the heat-treated specimen had a higher mean absolute deviation (MAD) at 0.263 mm compared to the standard one with 0.141 mm. Detailed dimensional measurements further revealed shrinkage of the samples due to the crystallization-

induced volumetric shrinkage and relief of the residual stress. For the mechanical performance, both polymeric samples exhibited enhanced mechanical properties by increasing their elastic modulus and yield strength due to increased degree of crystallinity and enhanced interlayer bonding. Nevertheless, the post-heat treatment induced the reduction in ductility of PLA but enhanced ductility of PEEK.

The investigation to the effects of the proposed post-heat treatment on the tribological performance of 3D-printed PLA and PEEK structures was made afterwards. The focus was on investigating the friction-induced vibration (FIV) behaviour of embedding re-entrant auxetic structures on the wear model of 3D-printed PLA under dry sliding wear process. It was found that during the sliding wear process, the friction-induced vibration was effectively suppressed with the embedded re-entrant auxetic structures thanks to exceptional energy absorption behaviour. Further, this effect is more pronounced at the larger re-entrant internal angle, in this case the 60 degrees, owing to a more negative value of NPR in the horizontal direction. Also, the presence of re-entrant auxetic structure led to a more stable coefficient of friction (CoF) pattern within a lower CoF range, and the wear loss of the re-entrant wear model was reduced by avoiding the surface fatigue wears thanks to the energy absorption and vibration insulation capacities. The SEM revealed a wear mechanism transition from adhesive wear to mild abrasion with the increased of re-entrant auxetic angles from 20 degrees to 60 degrees. This is likely attributed to the reduction in frictional heating from the experimental results. Building upon the understanding of the wear mechanism of AM-fabricated filaments incorporating with the complex structures in controlling FIV within tribological applications, the post-heat treatment was applied to the neat PLA and high-performance polymer PEEK structures to further understand its effects on the time-dependent tribological performance of materials, particular with complex structures. The result revealed that the increased stiffness enabled the re-entrant structures to more effectively reduce FIV during the sliding process of specimens. However, heat treatment produced contrasting effects on the wear performance of the two polymers. The specific wear rate of the heat-treated PLA sample with the re-entrant structure increased from $2.36 \times 10^{-5}\ mm^3/(N \cdot m)$ to $4.5 \times 10^{-4}\ mm^3/(N \cdot m)$, while it decreased for the PEEK sample from $3.18 \times 10^{-6}\ mm^3/(N \cdot m)$ to $6.2 \times 10^{-7}\ mm^3/(N \cdot m)$. Microscopic observations revealed that this difference was due to the variations in the brittleness of the treated materials, which influenced wear debris formation and the formation of the transfer film on the steel counterface.

Meanwhile, a limitation lies within the abovementioned work, which is the significant deformation required of energy absorption due to the auxeticity. Given the inherently low strength of neat PLA, only relatively low loads could be applied to ensure the auxetic structure deformed within elastic range. To overcome this constrain and consider the research trend of carbon fibre reinforced polymers (CFPRs) with complex structure designs, this study was extended to investigate the structural design and material selection using high-performance CFRPs composites under different loading conditions. It was found that the FDM-printed CFPRs re-entrant wear model still succeeds to suppress the FIV and associated noise in the polymer-steel sliding pair conditions. Also, such an effect became more noticeable with the higher degree of internal re-entrant angles. Nevertheless, the finite element analysis (FEA) demonstrated that the usage of a larger re-entrant angle creates higher stress concentrations within the structure, especially at the nodes and joints, which increasing the risk of premature failure. For the wear resistance, the microscopy analysis showed that severe fibre damages were greatly prevented with the re-entrant auxetic structures, leading to the significant decrease in the specific wear rate.

Finally, this study was extended to investigate environmental temperature effects, given the sensitivity of AM-fabricated parts performance to the external environmental stimuli and its importance for the long-term service life in the engineering applications, thereby enabling further optimization for thermally demanding conditions. Variable testing environmental regimes were applied based on the glass transition temperature (T_g) determined from DMA results of the neat PLA and neat PEEK. It was found that the FDM-printed PLA and PEEK structures was functional to suppress the friction-induced vibration, even when approaching their glass transition temperatures. However, operating near the glass transition temperature introduced a sudden increase in the specific wear rate for both polymers. This likely to attributed to the observed surface morphology on SEM and changed viscoelastic behaviour.

This thesis systematically investigated the effects of the post-heat treatment on the dimensional accuracy, mechanical performance of 3D printed neat PLA and PEEK, as well as the subsequent tribological performance of the developed self-tunning absorber (re-entrant auxetic wear model) under elevated temperature conditions. Furthermore, the coupled roles of structural design and material selection was evaluated with the utilization of CFRPs under various loading conditions. Overall, the outcome of this thesis contributed to enable and further optimize the AM-fabricated parts with post heat treatment for engineering applications, particularly in the tribological applications operating under thermally demanding conditions.

List of Tables

List of Figures

Nomenclature

FDM	Fused deposition modelling
DLP	Digital lighting processing
SLS	Selective laser sintering
EBM	Electron beam melting
VP	Vat photopolymerization
PBF	Power bed fusion
MJ	Material Jetting
ME	Material Extrusion
CLIP	Continuous liquid interface production
TPP	Two-photon polymerization
MJF	Muti-jet fusion
DMLS	Direct metal laser sintering
DIW	Direct ink writing
FFF	Fused filament fabrication
PLA	Polylactic acid
CF-PLA	Carbon fibre reinforced polylactic acid
PEEK	Polyether ether ketone
ABS	Acrylonitrile butadiene styrene
PC	Polycarbonates
CFRPs	Carbon fibre reinforced polymers
DIC	Digital image correlation
HPPs	High-performance polymers
PI	Polyimide
PEI	Polyetherimide

PPS	Polyphenylene sulfide
FEA	Finite element analysis
ML	Machine learning
HIP	Hot isostatic pressing
NPR	Negative Poisson's ratio
FIV	Friction-induced vibration
NPRM	Negative Poisson's ratio metamaterials
FETO	Functional element topology optimization
SLM	Selective lasering melting
HEA	CoCrFeMnNi high-entropy alloy
SFRP	Short carbon reinforced polyamide
MAD	Mean absolute deviation
T_g	Glass transition temperature
h	Length of re-entrant vertical strut (mm)
l	Length of re-entrant inclined strut (mm)
t	Thickness of the strut cross-section (mm)
θ	Re-entrant angle between the vertical and inclined struts (°)
β	The length ratio of h/l
ε_{axial}	Axial strain
ε_{trans}	Transverse strain
ν_{xy}	Poisson's ratio along x direction
ν_{yx}	Poisson's ratio along y direction
DMA	Dynamic mechanical analysis
DSC	Differential scanning calorimetry

SWR	Specific wear rate
LVDT	Linear variable differential transformer
w_t	Time-dependent wear rate
Δh	Height loss
AV	Average vibration
HT	Heat-treated
PLA-HT	PLA with post-heat treatment
PEEK-HT	PEEK with post-heat treatment
AVP	Absorbed vibration percentage
SEM	Scanning electron microscopy
EDS	Energy-dispersive X-ry spectroscopy
AFM	Atomic force microscopy
CoF	Coefficient of friction
Re-20/Re20	Re-entrant Auxetic 20 Degrees
Re-30/Re30	Re-entrant Auxetic 30 Degrees
Re-45/Re45	Re-entrant Auxetic 45 Degrees
Re-60/Re60	Re-entrant Auxetic 60 Degrees
R_a	Surface Roughness (μm)
Solid	Solid benchmark
Solid-HT	Solid benchmark heat treated
Re60-HT	Re-entrant auxetic 60 degrees heat treated
Solid/Re60 PLA	PLA samples with re-entrant auxetic structures (Re60) and without re-entrant auxetic structures (Solid)

Solid/Re60 PLA-HT	PLA heat treated samples with re-entrant auxetic structures (Re60) and without re-entrant auxetic structures (Solid)
Solid/Re60 PEEK	PEEK samples with re-entrant auxetic structures (Re60) and without re-entrant auxetic structures (Solid)
Solid/Re60 PEEK-HT	PEEK heat treated samples with re-entrant auxetic structures (Re60) and without re-entrant auxetic structures (Solid)
wt.%	Weight concentration percentage
EA	Energy absorption
REAS	Re-entrant auxetic structure
Solid benchmark/Solid-5N	Solid benchmark under applied load of 5 N
Solid benchmark/Solid-10N	Solid benchmark under applied load of 10 N
Re60-5N	Re-entrant auxetic 60 degrees under applied load of 5 N
Re60-10N	Re-entrant auxetic 60 degrees under applied load of 10 N
Re60-PLA-Room	Re-entrant auxetic 60 degrees made in PLA tested under room temperature
Re60-PEEK-Room	Re-entrant auxetic 60 degrees made in PEEK tested under room temperature
Re60-PLA-X°C	Re-entrant auxetic 60 degrees made in PLA tested under the temperature at X°C

Re60-PEEK-X°C	Re-entrant auxetic 60 degrees made in PEEK tested under the temperature at X°C

Table of Contents

Chapter 1 Introduction

1.1 Background

Over the past decades, there have been a rapid development and advancement in additive manufacturing, which enables the creation of the complex functional 3D component by building materials layer by layer in a wide range of advanced materials selections, such as polymers and metals [1], [2]. In particular, the production of polymeric parts using fused deposition modelling (FDM) has gained significant field, owing to its design flexibility, lost cost, and time-efficient prototyping capabilities [3].

The most common polymers used in FDM technology include acrylonitrile butadiene styrene (ABS), polylactic acid (PLA), and polycarbonates (PC), etc [4], [5], [6]. Among these, PLA filament stands out as the most widely used material in 3D printing due to its low cost, ease of processing, biodegradability, and biocompatibility [6]. These attributes make PLA attractive for a variety of applications, particularly in the biomedical field [7]. Nevertheless, PLA exhibits limitations that restrict its broader engineering applications, such as low toughness and poor heat resistance [6]. To address these limitations, the carbon fibre reinforced polymer composites (CFRPs) and high-performance polymers (HPPs) were employed. Over the past decades, the utilization of AM-fabricated CFRPs has emerged to meet industrial demands and applications [8], [9], [10], not only due to their inherently outstanding mechanical properties and lightweight characteristics, but also to their ease of manufacturing processes [11]. Among the studies, the sliding friction and wear behaviour of 3D-printed CFRPs are critical not only for the tribological studies but also for ensuring the long-term service life of the engineering applications [12]. Nevertheless, the research on the design of 3D-printed CFRPs, especially with respect to the structural design for enhancing the wear resistance remains limited [12], [13]. For HPPs, the processing of high-performance polymers (HPPs), such as polyimide (PI), polyetherimide (PEI), and polyether ether ketone (PEEK), through 3D printing has attracted significant attention recently [14], [15], [16], [17], [18]. In particular, PEEK has been extensively studied due to its out-standing physicochemical properties, including excellent heat resistance, mechanical strength, corrosion resistance, biocompatibility [19], [20], [21], [22], and high wear resistance [23]. These qualities make PEEK an ideal material for a wide range of applications, such as aerospace, medical, and tribological systems [24], [25], [26], [27]. Although the intrinsic inherent advantages of PEEK facilities the applications in various engineering field, the existing fabrication challenges in FDM [15] and the research gap in the

understanding of the tribological performance of the AM-fabricated HPPs impede the further development [28], [29]. Additionally, the neat PEEK continued to suffer from severe wear and shown insufficient tribological behaviour under the dry sliding conditions, which significantly challenged the long-term services life of the AM-fabricated PEEK component [30], [31], [32].

Meanwhile, the inherently as-built limitation of FDM method, such as the reduction in strength and the degradation of the material properties constrains the performance and challenges the broader applications [33]. Extensive research is conducted to enhance the performance of the FDM printed component. Among these, the post heat treatment or annealing has been applied as one the critical post processing techniques for enhancing the mechanical properties and its performance [34]. Despite the beneficial effects of the post-heat treatment on the mechanical strength, its effect on the long-term tribological performance with the involvement of complex structures are limited [35], [36]. While it is often assumed that improvements in mechanical properties lead to enhanced tribological performance, tribological properties are not intrinsic material properties. Instead, they are instead dependent strongly on the specific system and operating conditions in which a material or structure has to function.

Among the tribological studies, friction-induced vibration (FIV) is common and critical issue. FIV occurs when the frictional forces cause the mechanical oscillation in the system during the sliding wear process, and this oscillation poses the significant challenges in the mechanical system, resulting in the unwanted noise, wear and potential system failure [37]. Mitigating and controlling the FIV is vital for improving the reliability and longevity of the machinery and thus minimizing the downtime and operational costs. Although, extensive analytical and experimental research has been conducted to develop the control methods based on the precedent analysis of mechanisms [38], [39], [40], [41], [42], the proposed control system inevitably introduced extra complexity and cost of the mechanical system.

To address this challenge and limitation, the re-entrant auxetic structures (metamaterials) were employed due to the unique characteristics of Negative Poisson's ratio (NPR). The development of re-entrant auxetic structures was constrained by the challenges associated with manufacturing such complex geometry structures back then, until the recent development the additive manufacturing techniques [43], [44]. Taking the advantages of energy absorption ability [45], [46] and vibration ability [47], the re-entrant auxetic structures are in favourable in various engineering applications, particularly in the exploration of the band gap characteristics to isolate the vibration and sound [48], [49], [50]. Nevertheless, the existed

limitations of re-entrant auxetic structures included as-built printed defects, the dimension distortion and surface quality in selective lasering melting (SLS) with metals [51], or the balance between the stiffness and auxetic behaviour of applications [52] challenges the further development. Further, to the best of our knowledge, the auxetic materials/structures have not been directly used in tribological applications. The main challenges not only lied of the friction-based metamaterials potentially suffering from wear [53] but also the larger deformation from auxetic behaviour required for energy absorption [54], [55], [56].

Finally, the performance of AM-fabricated parts is highly sensitive to the external environmental stimuli or the external operating conditions, in particular under the influence of temperature, which significantly challenges the performance outcomes of the consistency and reliability in the applications [57], [58]. Although, the literature has reported the critical influence of environmental temperature in the thermal properties and mechanical performance [59], [60], as well as the wear behaviour of the 3D-printed components [61], [62], the effects of environmental temperature on the tribological performance of HPPs embedded in the complex structures remains unexplored [63], [64], [65].

Overall, in view of the overlapping research gaps of the FDM-printed parts with post heat treatment in the tribological context incorporating with functional complex structures, as well as the critical issue needs to control the friction-induced vibration (FIV), the objectives of this study were defined.

1.2 Objective of study

The main objective of this research thesis is to systematically investigate the effects of the post-heat treatment on the dimensional accuracy and mechanical performance of 3D-printed neat PLA and PEEK, as well as the subsequential tribological performance embedded in the re-entrant auxetic structures under elevated environmental temperature conditions. Meanwhile, the effect of CFRPs on the tribological behaviour of the developed self-tunning absorber under loading conditions was systematically studied. Collectively, the outcome of this research thesis contributed to enable and further optimize the AM-fabricated components through post-processing techniques to explore and enhance the functional performance and extending the application in the thermally demanding operations. The specific objectives to achieve these aims are systematically outlined as follows:

1. Explore and characterize the effect of proposed post-heat treatment on the dimensional accuracy and mechanical performance of FDM-printed neat PLA and PEEK.
2. Investigate the subsequential post-heat treatment on the tribological performance of the 3D-printed PLA and PEEK, but included the effect of the complex structure design, i.e., the re-entrant auxetic structures.
3. Examine and establish the structural design and advanced material selection of the developed self-tunning absorber (the complex structure design embedded to the wear model to reduce the friction-induced vibration) fabricated using carbon fibre reinforced PLA composites under diverse operational environments.
4. Evaluate and analyse the effect of environmental temperature on the tribological performance of the 3D-printed neat PLA and PEEK structures.

1.3 Additive manufacturing of polymers and polymer composites

1.3.1 Development of additive manufacturing techniques

Over the past decade, there have been rapid advancements in additive manufacturing, which enable the creation of complex 3D components by adding material layer by layer, using a wide range of engineering materials such as polymers, metals, ceramics, and concrete [1], [2]. Distinct additive manufacturing techniques were developed, such as the Fused deposition modelling (FDM), Digital lighting processing (DLP), Selective laser sintering (SLS), Electron beam melting (EBM) and so on [66]. According to the ASTM standard, the additive manufacturing techniques were categorized with vat photopolymerization (VP), powder bed fusion (PBF), material jetting (MJ), and material extrusion (ME) [67]. Each technique offers distinct advantages in polymer filaments fabrication according to the unique working characteristics, enabling a broader choice of the technique based on the applications and targeted properties of the polymer and polymer composites [68].

Vat photopolymerization (VP) selected the liquid photosensitive polymers (liquid resins) in a vat to fabricate the 3D model design using radiation, the Ultraviolet (UV) light and visible light. Taking the advantages of light-curing process, VP technique provides high printing accuracy and resolution, which can be reached to micrometre scale. With the invention of the stereolithography (SLA) technology, the usage of light curing process has been applied to various manufacturing and application fields and further evolved into techniques, such as the digital lighting process (DLP), continuous liquid interface production (CLIP), and Two-photon polymerization (TPP). Nevertheless, although the targeted characteristics of high printing accuracy and resolution offered by VP technique, the inherently limitations such as the limited choice of material only with photopolymer resins, the inferior mechanical and thermal performance, and limited vat scales deserved a thorough consideration [69].

Powder bed fusion (PBF) selected the powdered materials to fuse through various ignition sources to fabricate the complex three-dimensional design layer-by-layer. With the development of the PBF techniques, four subsets were developed: electron beam melting (EBM), multi-jet fusion (MJF), selective laser sintering (SLS), and direct metal laser sintering (DMLS) [70]. Taking the advantage of no requirements with support structures, larger varieties of powdered materials selections and design freedom, PBF technique offered broaden applications in multiple fields, such as aerospace, biomedical, and automotive manufacturing. Nevertheless, the core of PBF technique lies in the carefully control of the processing strategies

to maintain the appropriate printing environments and parameters for the targeted mechanical properties, whereas conducting the necessary post-processing to achieve the desired surface finish [71]. In addition, the low cost-efficiency and slow production rates compared with other techniques required attention [72].

Material jetting (MJ) fabricated the three-dimensional design in which the photopolymer (liquid droplets) was selectively jetted onto the building platform and cured typically with UV lights layer-by-layer. Taking the advantage of this unique manufacturing approach, the MJ technique offered a thin layer thickness in micrometres scale for printing the quality-demanded parts and targeted properties of low surface roughness texture. Nevertheless, the limitation of the low mechanical and thermal performance was shared with VP technique due to the inherently material nature of liquid photopolymer [73]. In addition, the long-term aging and the exposure to the lights and humid environment facilitated the mechanical degradation, thereby influencing the durability of the cured parts [74]. Overall, although the availability of the printing scale in micrometres and targeted low surface roughness texture was predominant, the MJ technique of the selectively liquid photopolymer droplets in advanced application still existed numerous technology challenges, such as the limited selection of high-performance material for MJ technique and the critical need to further enhance the printing process, etc [75].

Material extrusion (ME) fabricated the target objects layer-by-layer by melting and extruding the thermoplastic polymer filaments through the printing nozzle. The ME technique is the most common and widely used additive manufacturing technique at the current stage and can be categorized into two methods: direct ink writing (DIW), and fused deposition modelling (FDM) or fused filament fabrication (FFF) [76]. The DIW technique printed the design model layer-by-layer by melting and extruding the rheological materials through the nozzle. Taking the advantages of cost-effective and wide selection of the materials, the DIW technique gained increasing research interests. Although limitation of the printing accuracy and stability poses the challenge of the development of DIW techniques, the introduced method such as machine vision and real-time monitoring had improved the printing the quality of the print [76], [77]. The FDM technique fabricated the three-dimensional model layer-by-layer by melting and extruding the polymer filaments on the build platform through the printing nozzle and solidifies upon cooling. The production of the production of polymeric parts using fused deposition modelling (FDM) has gained significant attention in the field, owing to its design flexibility, low cost, and time-efficient prototyping capabilities [3], [78]. Nevertheless, the limitations of the FDM method, such as the reduction in strength and the degradation of the material

properties constrain the prevailing industrial applications [33], [79]. Extensive research is conducted to enhance the performance of the FDM printed component [80], such as the optimization of the printing parameters [81], conducting the heat treatment [82], establish a design-compensation approach by performing a virtual pre-processing with the model [83], and so on. As reported by literature, the optimization of the printing settings indeed improved the mechanical strength, but certain issues remained regarding the interlayer bonding of the 3D printed parts, internal residual stress [34].

1.3.2 Advanced Material: additive manufactured polymers and polymer composites

Thanks to the emerging and developing additive manufacturing, increasing attention has been directly towards the advanced 3D printed polymers and polymer composites owing to intrinsically advanced material properties, ease of fabrication, customized reinforced schemes, and compatible to multiple fields [76], [84], [85]. The specific material selection for the discussed additive manufacturing techniques depends on the application needs of the desired properties. In this research thesis, the main focus was on the selected thermoplastic filament of polymer and polymer composites fabricated with FDM technique, namely polylactic acid (PLA), carbon fibre reinforced polylactic acid (CF-PLA), and polyether ether ketone (PEEK).

Polylactic acid (PLA)

The most common polymers used in FDM technique include acrylonitrile butadiene styrene (ABS), polylactic acid (PLA), and polycarbonates (PC), etc. [4], [5]. Among these, PLA filament stands out as the most widely used material in 3D printing due to its low cost, ease of processing, biodegradability, and biocompatibility [6].

Polylactic acid (H-[$OCHCH_3CO]_n$-OH) is a renewable thermoplastic polymer matrix and an aliphatic polyester made from lactic acid [86]. Thanks to the development of the additive manufacturing and a broader recognition of the sustainable material, a significant amount research trend raised to 3D printing PLA since 2015 [87]. Taking the advantages of good compatibility [88], [89] and ease of processing in a low melting point [90], low cost [91], the 3D printed PLA has been applied in multiple fields, such as medical [92], aeronautical [93] , and so on. For instance, DeStefano et al. [94] provided a comprehensive review of the important role of PLA in contemporary medical field owing to its compatibility and tuneable mechanical properties. Their review highlighted the great potential of integrating the PLA with the additive manufacturing in the field of customized regenerative medicine.

Despite the inherently limitations in material properties compared to other polymers in FDM applications, such as lack of flexibility and potential wrapping due to high thermal expansion coefficients, these limitations can be addressed at certain stage with the incorporation of fillers and modifications of the printing parameters [87]. For instance, Raj et al. [95] reviewed the case studies of 3D printed PLA in the engineering applications in accordance with the optimization of the printing parameters. In particular, tailoring the factors such as the infill density, layer height or printing orientation could essentially alternate the tensile strength and stiffness of the material in order to meet the specific energy requirements. Their case studies provided a guidance for optimizing the 3D printed PLA based structures to the potential engineering applications. Olam et al. [96] investigated the mechanical behaviour of the proposed PLA/TiO_2/Hydroxyapatite composites filaments in FDM through experimental tests. The result revealed that adding the fillers of TiO_2 and Hydroxyapatite indeed improved the stiffness, hardness and surface profile compared to the neat PLA. Their findings demonstrated that the utilization of PLA composites materials extended it potential with biomedical applications. Rodríguez-Reyna et al. [97] investigated the effects of the controlled heat treatment on the mechanical performance of 3D printed PLA and ABS FDM parts. The results revealed that the proposed treatment temperature and duration improved the mechanical strength and rigidity of PLA, while enhancing the toughness of the ABS owing to the increased degree of crystallinity and interlayer diffusion. Their findings demonstrated that the utilization of post-heat treatment is an approach to improve the structural integrity and mechanical properties of the materials for the engineering applications. Taşcıoğlu et al. [98] investigated the influence of critical printing parameters on the surface roughness and dimensional accuracy of the 3D printed PLA parts, while considering different post treatment methods, such as chemical smoothing and thermal treatment to further enhance the properties. The results revealed that integrating the optimized settings of the lower layer height with the proposed printing temperature and extrusion speed with the thermal treatment can improve the finished surface profile and the dimensional accuracy. Their findings demonstrated the achievement of integrating the printing parameters with the post treatment to enhance the surface profile and mechanical strength for purpose of a high quality and precision printed PLA part.

The abovementioned work demonstrated the feasibility and functionality of different strategies to enhance the mechanical properties and overall performance of the 3D printed PLA in order to broaden the applications. Also, experimental research and the comprehensive critical reviews established the decent understanding of the key mechanisms of the PLA performance

under diverse operating conditions. Building upon these, in this research thesis, the 3D printed Polylactic acid was selected as the initial filament material.

Further, despite the potential printing defects of the FDM PLA parts, utilization of the natural fibre reinforced PLA composites could address these issues [99] and broad the wider range of the applications [100]. Therefore, the selection of neat PLA at the first sight set the fundamental tone to the subsequent research comparison with the carbon fibre reinforced PLA composites (CF-PLA).

Carbon fibre reinforced polylactic acid (CF-PLA)

Carbon fibre reinforced polymers are composed of the carbon fibre to the load-bearing to the original polymer matrix which provides the stability against the environmental degradation [101]. Among the categories of the reinforced carbon fibre, the discontinuous or short fibres are widely applied [11]. Taking the advantages of lightweight and outstanding mechanical properties [102], in the last decade, the additively manufactured CFRPs have emerged to fulfil the industrial demand for the fabrication of end-user parts without the need for multiple manufacturing process or specialized moulding tools [8], [9], [10]. For instance, Zhang et al. [103] investigated the syncretical effects of the 3D printed fibre orientation with the topology optimization of the printing path on the mechanical strength of the carbon reinforced polymer composites in additive manufacturing. The result revealed that the optimised fibre orientation, aligning with principal stress direction achieved a higher strength to 305% and stiffness to 256% compared to the conventional path. Their findings provided a practical route to fabricate the carbon fibre reinforced polymer composites in a lightweight and enhanced loading bearing capacity in order to replace the metal parts. Lu et al. [104] investigated the impact behaviour of the reinforced concrete beam and carbon fibre reinforced concrete beam, while capturing the deformation process and strain evolution with the digital image correlation (DIC) method. The result revealed that the carbon fibre reinforced concrete beam had an enhanced stiffness, vibration damping ability, and a delayed crack initiation compared to the simply reinforced concrete beam. Their findings demonstrated integrating the carbon fibre reinforcement with the advanced optical measurements provided a practical route to investigate the dynamic response to support the structural design in applications. Harnden et al. [105] investigated the effects of the multifunctional structure carbon fibre composites system on the piezoelectric-based energy harvesting in additive manufacturing. The result revealed that the proposed carbon reinforced multifunctional structure were able to harvest the energy through mechanical

deformation, while holding a remarkable stiffness and strength. Their findings demonstrated the utility of the CRRPs multifunctional structure significantly enhance the system efficiency and reliability under different operating conditions.

The abovementioned work demonstrated the application of the CFRPs, and as reported by literature, a significant research interest also focused on the test of the tensile and flexural properties of the additive manufacturing CFRPs [106]. Meanwhile, the sliding friction and wear behaviour of the 3D printed CFRPs are critical for the tribological study and applications [12]. For instance, Man et al. [107] investigated the effects of fibre orientation, volume fraction and friction contact interfacial quality on the friction and wear behaviours of the 3D printed carbon fibre reinforced PA6 composites. The result revealed that although the friction behaviour strong affected by the fibre orientation, the utilization of CFRPs significantly enhanced the wear resistance and reduced wear loss. This is likely to be attributed to the stabilized load transfer and the suppressed polymer deformation. Lin et al. [108] investigated the effect of the incorporation of nano-silica coating on the friction and wear performance of the 3D printed CFRPs PEEK. The result revealed that the utilization of the nano-silica coating improved the wear and friction performance owing to the promotion of the denser microstructure in accordance with the nano-silica dispersion and interfacial compatibility.

Nevertheless, despite these advancements, research on the design of printed CFRPs, especially with respect to structure design for improved wear resistance, remains limited [12], [13]. Therefore, more studies need to be conducted regarding the wear behaviour of the additive manufacturing CFRPs involved with the complex structure design. This research gap also matches the aim of later Chapters of developing high tribological performance FDM-printed engineering structures using CFRPs based on our previous work [109].

Polyether ether ketone (PEEK)

As discussed with the selection of neat PLA and associated CF-PLA set the fundamental tone in this research thesis. The attention must now be paid to high-performance polymers (HPPs), such as polyimide (PI), polyetherimide (PEI), and polyether ether ketone (PEEK) in order to meeting the demands of high-end engineering applications [14], [15], [16], [17], [18]. In this research thesis, polyether ether ketone (PEEK) emerges as the critical next step due to its outstanding physicochemical properties, including excellent heat resistance, mechanical strength, corrosion resistance, biocompatibility [19], [20], [21], [22], and high resistance to wear [23]. Thanks to the emerging and rapid development of the additive manufacturing, PEEK nowadays

can be processed and printed into complex geometries that were implausible for the conventional manufacturing [2], [110]. For instance, Etchegaray-Bello et al. [111] investigated the effects of fibre reinforced PEEK and polyphenylene sulfide (PPS) composites on the thermal running behaviour and the residual mechanical performance of the battery enclosure applications in the electron vehicle. The result revealed that the reinforced PEEK composites had an excellent thermal stability and ability to retain the original material properties compared to the PPS composites confirmed by the microscopic results on the matrix damage and crack. Their findings demonstrated the utilization of the high-performance polymer composites to ensure the safety and structural integrity of battery enclosures. Overall, these qualities make PEEK an ideal material for a wide range of applications, such as aerospace, medical, and tribological systems [24], [25], [26], [27].

However, the fabrication of PEEK via fused deposition modelling (FDM) or fused filament fabrication (FFF) presents several challenges. For instance, due to the relatively high printing temperature required, thermal residual stress can accumulate, leading to distortion and interlayer delamination [15]. Consequently, 3D-printed PEEK parts often exhibit inferior mechanical properties compared to conventionally injection-molded PEEK, primarily due to printing-induced defects such as weak interlayer bonding, distortion, and delamination [16], [17]. To address these limitations, extensive research has focused on optimizing FDM process parameters for PEEK [16], [17]. Wang et al. [17] employed finite element analysis (FEA) to simulate the melting behaviour and fluidity of PEEK to identify suitable printing parameters for achieving adequate surface quality and enhanced mechanical performance. Their study concluded that a higher nozzle temperature of 440 °C and a reduced layer thickness of 0.1 mm improved part density, reduced internal defects, and strengthened interlayer and infill bonding. Tafaoli-Masoule et al. [16] applied a Taguchi design of experiments (DoE) approach to systematically investigate the influence of FDM parameters such as nozzle temperature, bed temperature, print speed, and layer thickness on the tensile strength and elongation at break of printed materials. Rosa-Sainz et al. [112] studied and tested the utilization of PEEK, focusing on the experimental formability as the customized cranio-maxillofacial prosthesis. The result revealed that under the optimized processing conditions, the thermoformed patient-specialized shape from printed PEEK sheet exhibited an excellent thermoforming ability and the ability to maintain the dimensional accuracy. Their findings demonstrated a practical guideline to the design of biocompatible customized medical prosthesis in 3D printed PEEK. Feng et al. [113] investigated the utilization of the machine learning (ML) techniques to optimize the printing

parameters setting of the PEEK in FDM method. The result revealed that the comprehensive training on the effects of multiple critical printing parameters enables the proposed machine learning algorithm to effectively identify the appropriate printing parameters to achieve enhanced material performance. Their findings demonstrated that the potential of the employment of the machine learning algorithm to overcome the printing defects and challenge on the neat PEEK in FDM method. Nevertheless, despite the discussed advantages of PEEK, fully overcoming the intrinsic defects associated with the FDM processing of HPPs remains challenging. The high melting temperatures of HPPs, combined with natural cooling and thermal gradients during printing, inevitably compromise the degree of crystalline perfection in printed parts, thereby adversely affecting their mechanical properties. As a result, post-processing treatments have become a necessary step to enhance the structural integrity and overall performance of printed polymer components [114].

Further, as reported by literature, many researchers focused not only on the medical field as the biomaterial-based implant [115] but also develop and test the matrix composite to meet the demands of various applications [116]. However, the friction and wear behaviour of 3D manufactured PEEK displayed as a critical role to the current applications, and a research gap existed in between [28], [29]. For instance, Reddy et al. [28] investigated the wear behaviour of 3D printed based on the found issue of significant damage to both teeth and implant during mastication caused by wear and friction in order to develop a lost cost implant oral solution. Abhay et al. [117] investigated the wear resistance, colour stability, and the displacement resistance of the 3D printed PEEK crown compared to the zirconia crown through in the analytics-based mastication and accelerated aging. Hintze et al. [118] provided a comprehensive assessment of the friction and wear behaviour of neat PEEK and its associated composites under both dry and lubricated sliding conditions. The results revealed that the neat PEEK exhibited moderate wear resistance and the incorporation of different fillers enhanced the wear resistance. In addition, the sliding with lubricants further stabilized the frictional behaviour and protected from the surface damage compared to the dry sliding conditions. Their finding addressed an existing gap in the understanding of the tribological performance of the high-performance polymers in additive manufacturing.

Although the above discussion underscored the importance of the wear and tribological properties of PEEK, the neat PEEK continued to suffer with severe wear and exhibited insufficient tribological behaviour under the dry sliding, which challenge the durability and service life of the PEEK component despite their intrinsic inherent advantages [30], [31], [32].

Among the strategies to address this challenge, a new pathway with a multifunctional complex structure design to improve the tribological behaviour of PEEK overcome the tribological limitations of the monolithic PEEK [119].

1.4 Post-processing strategies for additively manufactured polymers and polymer composites

1.4.1 Post-processing strategies

The emerging and rapid development of the additive manufacturing has expanded the frontier of the material science and instigated a revolution in the manufacturing industry as discussed in the Chapter 1.1. Within this fundamental shift, the post-processing strategies act as a critical role in transforming the fabricated raw engineering components into the industry-level standards by addressing the inherently limitations of additive manufacturing techniques [120]. Up to now, various post-treatment methods have been developed to improve the performance of FDM-printed components [121]. For instance, Li et al. [122] investigated the chemical treatment, such as the hot vapor chemical smoothing, on the surface roughness of the printed PLA parts. The result was promising, showing a significant reduction in surface roughness of the 3D-printed PLA components through the optimized Taguchi L16 experimental design. Pricci et al. [123] studied the experimentally validated digital twin of the ironing process in extrusion-based additive manufacturing. The result demonstrated that the optimized ironing parameters can remarkably enhance tensile strength. In particular, the combination of ironing temperature, pressure, and speed improved the ultimate tensile strength by improving the layer bonding and reducing surface defects. Moradi et al. [124] investigated the effect of the utilization of CO_2 laser beam cutting as a post-processing technique on the dimensional accuracy and edge quality of the FDM-printed PLA parts. The results demonstrated that the optimized laser parameters can significantly improve dimensional accuracy by reducing the kerf width and taper and producing high-quality cuts.

In general, the common post-processing techniques can be summarized into eight categories: cleaning, support structure removal, surface finishing, ultrasonic finishing, surface coating, hot isostatic pressing (HIP), and heat treatment [120].

Cleaning

Cleaning is a crucial and fundamental post-processing strategies to remove the residual particles or any unnecessary parts after the print. According to Kantaros et al. [120], the available tool include brushing, air blowing, precision water jetting, etc. Their quantitative

assessment on different tools revealed that approximately 85% of the unnecessary parts could be effectively removed with a fundamental brushing and air blowing. Further, the usage of the prevision water jetting improves the efficiency up to 98%. Nevertheless, this post-processing strategies could potentially distorted the fabricated parts during cleaning, particularly in the complex design.

Support structure removal

The support structure removal is another crucial and essential post-processing strategies to remove the temporary support generated during the printing process to support the overhang of the target three-dimensional design. This technique encompasses wide methods from the manual removing with different tools to the advanced water jetting or dissolved with chemical solution, depending on the selected AM techniques and materials [75], [120]. However, this technique shared a similar limitation of potentially damage the part during removing process as the cleaning strategies discussed above.

Surface Finishing

The surface finishing technique offers a critical approach to refine the surface texture by removing microscopic irregularities as-built surfaces and enabling polishing for the target characteristic from raw AM fabricated parts [125]. The methodologies could be generally categorized with mechanical approaches and the chemical treatments. For mechanical methods, the technique, such as grinding and sanding, was applied to refine the surface texture. On the other hand, the chemical treatment served the same propose as the mechanical one but focused on the solvent or dissolution [120]. The broad genres of surface finishing post-processing techniques enabled the flexibility in achieving the required characteristics of the AM fabricated parts based on the selected materials and working conditions. Meanwhile, the improved surface texture significantly affected the performance of the printed parts with the fatigue resistance and tribological performance. Nevertheless, the limitation of excessive polishing potentially resulted in the detrimental effect on the surface. Also, the difficult in achieving actual practicality across different product scales in the industry-level requirement still challenges the development of the surface finishing techniques [125].

Meanwhile, electropolishing was one of existing important surface finishing techniques, which typically applies to the AM fabricated metal parts and components. This technique emersed the printed model in the electrolyte solution while applying the electron current to target smooth surface finish by removing the irregularities observed in the microscopy [126]. For instance,

Beamud-González et al. [127] quantified improvement of the surface roughness of the AISI 316L stainless steel after applying the electropolishing. The results demonstrated that the surface roughness significantly reduced to 0.035 μm from the raw fabricated condition between 0.5 to 0.8 μm under the appropriate processing parameters. The electropolishing has the advantages in the flexible employment to versatile metal materials, such as titanium and stainless steel. Nevertheless, the limitations of uniformly emerging of the printed part and controlling of the dissolution rate still challenge the development of this technique [128].

Ultrasonic finishing

Ultrasonic finishing, including ultrasonic cleaning and ultrasonic cavitation, utilizes the ultrasonic vibrations to improve and polish the surface of the AM fabricated three-dimensional designs. The ultrasonic finishing generated the microscopic cavitation bubbles with ultrasound and imploded at the emersed fabricated part to remove the attached contaminations. For instance, Tan et al. [129] introduced the surface modification technique of ultrasonic finishing to improve the surface quality of PBF fabricated Inconel 625 part. The results showed that the surface roughness significantly reduced 45% due to the elimination of the certain amount of the melted powdered materials attached to the as-built surface. This technique has the advantages of cost-efficiency, high dimensional accuracy with less material removal, and compatible with the complex structures. However, the limitations of the difficulty in visualization of the process and highly dependent on the characteristics of the abrasive particles still challenge the current development of the technique [130].

Surface Coating

The surface coating technique served as an important functional-driven post-processing strategy to the AM fabricated components, particularly aiming to the improvement of properties of wear resistance and corrosion resistance and compensation for the inherently printing defects. Taking the advantages of meeting the wear and corrosion resistance and great potential to support high-temperature process, the surface coating technique has been applied in applications [125]. For instance, Rezanejad et al. [131] investigated the effect of FDM-printed PLA coating on the wear behaviour of the AM60 magnesium alloy. The results showed that with the coating of the FDM-printed PLA layer, the coefficient of friction and wear rate was significantly reduced due to the reduction in the delamination and adhesion mechanisms observed in the uncoating sample under microscopic analysis. Nevertheless, the surface coating

technique also faced challenges, including the limited coating conformity with complex structures, insufficient adherence and bonding between coating interfaces, and time-consuming.

Hot isostatic pressing (HIP)

The HIP technique typically applies the AM fabricated metal parts by exposing with high temperature and pressure gas simultaneously to enhance the structural integrity and mechanical properties by addressing the existing voids of the part during the print [132]. For instance, Lopez et al. [133] investigated the effects of HIP post-processing technique on the mechanical performance of the EBM fabricated Ti6242 alloy. The results showed that the tensile strength and fatigue resistance of the sample was improved due to the reduction in the internal porosity and defected during the printing process. Taking the advantages of effectively improving the critical inherently printing void issue and displayed flexibility with abundant metal materials, the HIP technique has been applied to multiple fields, such as aeronautical and medical. Nevertheless, the challenge of high cost, time-consuming and size constraints need to be addressed in the future state [120], [134].

1.4.2 Post-heat treatment

Among the various post-processing techniques discussed, post-heat treatment (or annealing) has emerged as one of the most important methods for improving the mechanical properties of printed parts [34], [135]. The post-heat treatment utilized the temperature changes to expand and activate the movement of the polymer molecular chain, facilitating the recrystallization of crystalline and semi-crystalline polymers [136], [137]. In addition, while relieving the residual stress during the heat treatment process, the interlayer bonding was improved to minimize the internal FDM 3D printed defects [138], [139], [140]. For instance, Yang et al. [136] investigated the effects of different thermal processing conditions during the 3D printing on the degree of crystallinity and mechanical performance of neat PEEK. Their finding revealed that the optimization of the ambient temperature, nozzle temperature and post-heat treatment methods increased the degree of crystallinity, leading to the enhanced material strength and stiffness, as opposed to the reduced mechanical integrity due to the insufficient heat exposure. Kumar et al. [141] studied the overall effect of the infill density and annealing on the mechanical performance of the selected filament. The results demonstrated that the higher infill density particular at 100% with the post heat treatment (annealing) enhanced the tensile strength and stiffness of the material owing to the improved interlayer bonding and interlaying diffusion, and the overall performance can be further improved with the usage of high-

performance polymer and polymer composites. Zhen et al. [142] investigated the augmentation effect of the 3D printing parameters and annealing conditions on the microstructure and mechanical performance of the printed PEEK. Their finding revealed that integrated the experimental pre-treatment printing settings with the annealing or the post-heat treatment improved the tensile strength, ductility and overall structural integrity. The mechanism behind this enhancement is the enhanced crystallinity developed during the heat treatment. which improved the interlayer adhesion, relived the residual stresses, and increased density of the crystal-phase. Dong et al. [143] examined the effect of post processing annealing on the 3D printed nanofiber reinforced PLA. Their findings highlighted the effect of the post-heat treatment on further enhancing the mechanical performance, the flexural strength and stiffness, thanks to the higher degree of crystallinity and reduced internal printing defects building upon the improved mechanical performance achieved through adding the nanofibers to the PLA.

Despite the beneficial effects of post-heat treatment on mechanical performance, its impact on the time-dependent tribological performance of materials, particularly in complex structures, remains limited [35], [36]. While it is often assumed that improvements in mechanical properties lead to enhanced tribological performance, tribological properties are not intrinsic material properties and instead depend strongly on the specific system and operating conditions in which a material or structure functions.

1.5 Additive manufactured re-entrant auxetic for friction-induced vibration control under environmental temperature conditions

Taking advantages of the discussion with additive manufacturing of polymer materials and associated post-processing strategies in previous Chapter 1.1 and Chapter 1.2, the AM fabrication of complex structures enhanced with selection post-processing methods in applications raised significant interests over the past decade [144]. Among these complex structural categories, the re-entrant auxetic structure (lattice structure/metamaterials) had emerged as a promising design due to its unique characteristics of Negative Poisson's ratio (NPR).

1.5.1 Re-entrant auxetic structures

Re-entrant auxetic structures belonging to the metamaterials [145] were first reported in 1987 [146]. However, it has not been widely investigated used for engineering applications back then due to the challenges in manufacturing such complex geometry structures, as seen in Fig 1.1.

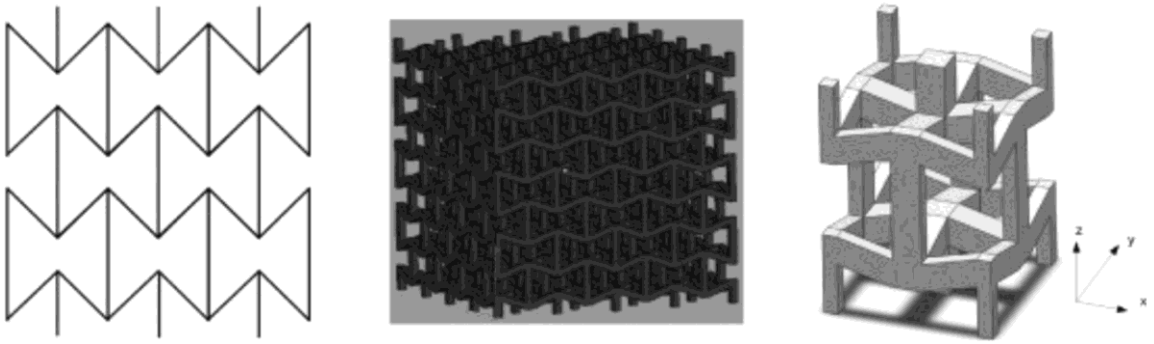

Fig 1.1 Examples of 2D and 3D Re-entrant Structure [146]

Thanks to the development of the additive manufacturing, the research interests of this Negative Poisson's ratio metamaterials have raised significantly in the last decade [43], [44], [147]. For instance, Yan et al. [148] investigated the performance of the stretchable strain sensor with amplified NPR effect employed with continuous fibre reinforced re-entrant auxetic structure in DIW. The results showed that amplified NPR enhanced the flexibility and sensitivity of the senor to a large-deformation response. Their findings demonstrated that the practical approach of utilization re-entrant auxetic structure in the sensor application. Gao et al. [149] investigated the mechanical behaviour of a large deformation auxetic double-V microstructures through the proposed geometrically nonlinear analytical model. The result demonstrated that the characteristics of ligament angle and thickness of the ligament and cell heights contributed to the change in Negative Poisson's ratio of auxetic microstructures. Their findings established a framework that connect geometric design to the auxetic behaviour, expanding the potential of the application. Zhang et al. [150] investigated the implementation of the proposed hydrogel meta structures using Direct Ink Writing (DIW). The result revealed that the printed meta structures had promising mechanical properties printing at the room temperature without sacrificial supports. Their finding highlighted the approach to manufacturing the mechanical resilient and biocompatible meta-structures, expanding the potential in biomedical applications.

In general, the re-entrant auxetic structures with the excellent acoustic properties [151], energy absorption ability [45], [46], [152], and vibration absorption ability [47], [153] are favourable in advanced engineering and industrial applications, such as in the field of aerospace, biomedicine, and sports. For instance, Wang et al. [154] introduced an innovative three-dimensional re-entrant auxetic structure design derived from 2D hexagonal cell validated by both FEA and experiments to improve the aircraft crashworthiness. The results showed that the application of the introduced 3D re-entrant auxetic design significantly improve the energy

efficiency compared to the traditional design of fuselage, thereby enhancing the aircraft crashworthiness. Munyensanga et al. [155] systematically investigated the mechanical response of the AM fabricated novel stent in the concept of the metamaterials tested both numerical simulation and experimental based. The result revealed that the response of the yield strength and maximum energy absorption of the designed stent could be controlled within a range. Their findings highlighted the tailoring of the tessellated unit cells allowed to control the effective elastic modulus and energy absorption ability of the stent, which offering a strategy to the design of the stent structures in general. Krishnan et al. [156] investigated the effect of embedded auxetic structure metamaterial in the sports helmet on the crash safety, specifically the impact energy absorption ability. The results revealed that having the auxetic structure embedded absorbed a high-level of impact energy and thus reduced the transmitted forces compared with the design without the structure. Also, tailored the design in a more negative value of Poisson's ratio, the energy absorption capacity was further enhanced from 50J to 165J.

Further, many researchers have also explored the band gap characteristics of the Negative Poisson's ratio structures focusing on the structural design or the material selection to achieve the vibration and sound isolation by creating the ability of blocking the acoustic wave and shifting the frequency into a lower range [48], [49], [50], [157], [158]. For instance, Pan et al. [159] investigated the design and modelling of re-entrant based structures to achieve the desired Negative Poisson's ratio for the purpose of vibration isolation. The result revealed that the vibration isolation effect was more pronounced when the Negative Poisson's ratio of the design model became more negative. Their findings highlighted the potential of using the re-entrant based design as the adaptable lightweight engineering vibration control foundations. Qin et al. [160] explored the topology optimization design of the Negative Poisson's ratio metamaterials (NPRM) for the vibration reduction performance in terms of proposed the functional element topology optimization (FETO) method. The result demonstrated that the new design on controlling the vibration is promising, showing at least 12% improvement compared to the traditional design. Their findings highlighted the utility of Negative Poisson's ratio metamaterials (NPRM) as the tuneable platform for the design of advanced lightweight structures in the application of vibration control.

Meanwhile, the limitations existed in the re-entrant auxetic structure continues to challenge the development of the applications, including the as-built printing defects as micro-cracking, dimension distortion and rough surface quality specifically in the selective lasering melting

(SLM) process with metal material [51], or the balance between the stiffness and the auxetic behaviour to the applications [52]. Notably, to the best of our knowledge, the auxetic materials/structures have not been directly used in tribological applications. The main challenges not only lied of the friction-based metamaterials potentially suffering from wear [53] but also the larger deformation from auxetic behaviour required for energy absorption [54], [55], [56]. Thus, it is important to ensure the structure will not undergo significant plastic deformation or failure along the sliding and investigate the wear performance of the design structure.

1.5.2 Friction-induced vibrations

Friction-induced vibration is a common issue that occurs when frictional forces cause mechanical oscillation in systems during the sliding wear process, and this oscillation can cause highly undesirable noise and wear to the tribological system [37]. Among the study on the material tribological performance, the friction-induced vibration is particularly important, as it poses a significant challenge in the mechanical system, often resulting in unwanted noises, wear and potential system failures [37]. Reducing such vibrations is vital for improving the reliability and longevity of machinery and thus minimizing downtime and operational costs. To date, extensive analytical and experimental research has been conducted to understand the mechanisms behind FIV, as well as its tribological effects under different contact conditions [8], [161]. For instance, Askari et al. [162] studied the effects of FIV on maximum contact pressure and moment of artificial hip implants. Their findings revealed that FIV induces an oscillating behaviour in the system dynamics, which may greatly affect implants' performance by altering the lubricating regions and elasticity of contact surfaces. Zhou et al. [163] investigated FIV in water-lubricated rubber bearings during shutdown, attributing the instability to stick-slip behaviour at the shaft interface. This effect is further influenced by material properties and dynamic changes in friction, temperature, and load. Lin et al. [164] investigated the effect of surface roughness variations on the friction-induced vibration and associated noises of the marine stern tube bearings using the proposed three-degree-of-freedom model coupling model. The result revealed that the change in surface roughness could trigger the self-excited vibrations and noises even operating under the smooth-stable sliding conditions. Their findings highlighted the crucial need for considering the realistic surface morphology in the bearing design to the strategy of reducing the FIV.

Above studies underscored the complexity and significance of FIV in tribo-systems. In response, both passive and active vibration control strategies have been developed to control

or mitigate FIV [38]. For instance, Chatterjee et al. [39] designed dynamic vibration absorbers to reduce the friction-induced vibration. They provided a framework specifically to the engineering design of dynamic vibration absorbers for the tribological system considering multiple factors, such as the frequency tuning, mass ratio, and damping efficiency. Nath et al. [40] explored the utility of the tangential acceleration feedback controlled to mitigate the vibration, which specially measures and responses to the tangential motion at the contact interface. Their findings demonstrated that the designed approach offers a fast and reliable means to control the friction-induced vibrations compared to the general passive control methods. Das et al. [41] applied a time-delayed feedback method, which involves the delay in the control signal based on the system's past states to suppress the friction-induced vibrations. This work revealed that the proposed method is practically and efficiently as the active control method to be used in the condition of sliding contacts and the belt-driven system. Chomette et al. [42] studied compared the linear and nonlinear control methods to suppress the self-excited vibrations (friction-induced vibrations and noises) in the dry sliding. They found that while the linear control method by adding a control vector had the advantages of easier implementation and effective on the reduction of the mild friction-induced vibration and noises, it falls short in handling the more complex conditions, such as the bifurcations and chaotic responses.

The abovementioned work demonstrated the feasibility and functionally of the active and passive control methods to the condition of controlling the friction-induced vibration and associated noises while simultaneously improves the tribological performance at certain stages. Nevertheless, the proposed control system inevitably introduces the extra complexity and cost of the mechanical system. To address this challenge and limitation, extensive analytic and experimental research were conducted on the optimization of the complex structural design that intrinsically vibration isolation advanced. In particular, the re-entrant auxetic structures, in which owns the unique Negative Poisson's Ratio properties, behaving as the lateral shrinkage upon axial compression [165] offered a potential solution.

1.5.3 Influence of the environmental temperature on the performance of additive manufactured structures

With the discussion of the development of the additive manufacturing techniques and advanced material selections, the inherently AM technique-induced defects were inevitable at the current stage but could be improved depending on the optimization of the printing parameters and selection of post-processing strategies. Nevertheless, the performance of the AM-fabricated parts remains highly sensitive to the external environmental stimuli or the working conditions,

in particular under the influence of temperature, which poeses the significant challenges in the performance outcome of consistency and reliability in the applications across multiple fields [57], [58]. For instance, O'Conner et al. [166] investigated the effect of low-pressure processing conditions on the structural integrity and mechanical properties of ME-fabricated polymers. The results revealed that the polymer samples exhibited increased density but a decrease in porosity and showed the enhanced ultimate tensile strength under low-pressure printing conditions. These behaviours were likely attributed to the reduction in the porosity and heat loss at the polymer surface. Their findings highlighted that the sensitivity of AM-fabricated parts performance to the environmental conditions. Hou at al. [167] investigated the effect of moisture absorption on mechanical performance of the AM-fabricated short carbon reinforced polyamide (SFRP) with varied microstructures. The results revealed that the absorbed moisture by SFRP remarkably impacts the tensile and shear strength and the deterioration of the sample became irreversible due to the permanent damage at the layer interfaces. Kaptan et al. [168] investigated the effect of the chemical resistance of a broad category of FDM-printed material filaments performance immersed in different liquid chemicals. The result revealed that the FDM-printed PP maintained most of the mechanical properties after exposure to the chemicals, whereas the filament such as PLA experienced a severe mechanical degradation in the solvents like acetone. Their finding highlights the sensitivity of AM-fabricated parts to the exposure of chemical.

Among these influential factors, the temperature or environmental temperature exerts a critical influence, as reported by literature. For instance, Chen et al. [59] investigated the dynamic compressive performance and failure mechanisms of the temperature-dependent AM-fabricated CoCrFeMnNi high-entropy alloy (HEA) parts. The results showed that the elevated temperature leads to the remarkably reductions in the flow stress and dynamic strength with the corresponding transition of the failure modes from localized sheer-dominated fracture to the more uniformly ductile deformation. Their findings demonstrated the critical role of environmental temperature on the performance of mechanical properties of AM-fabricated parts in engineering applications. Wen et al. [60] investigated the time-dependent thermal and mechanical properties of AM-fabricated (SLM) Ti600 alloy. The results revealed that the thermal conductivity and thermal expansion improved with elevated temperatures, whereas the mechanical properties of elastic modulus and tensile strength significantly decreased above the temperature at 550°C due to phase coarsening and decomposition. Das et al. [169] critically assessed the current development and remaining challenges of in high temperature AM-

fabricated engineering thermoplastic polymers. Their findings highlighted the temperature effects leads to the inconsistent structure processing properties and emphasized the needs the improvement with different methodologies to achieve the reliable mechanical performance of AM fabricated parts in high temperature conditions.

Above studies underscored the significance of the effect of environmental temperatures in the thermal properties and mechanical performance of the AM-fabricated components. Further, the environmental temperature also significantly influences the wear behaviour. For instance, Joshy et al. [61] systematically investigated the wear behaviour of AM-fabricated (PBF) Ti6Al4V under the elevated environmental conditions from 28°C to 600°C and variable sliding speeds. The result revealed that the wear loss significantly increased with altered friction behaviour above 400°C, whereas the dominant wear mechanism at the lower temperature was abrasive and delamination wear modes. Their findings highlighted the sensitivity of tribological performance of AM-fabricated parts under the environmental temperature conditions. Tripathy et al. [62] comprehensively investigated the fretting wear behaviour of AM-fabricated (PBF) Inconel 625 superalloy compared with wrought counterpart under the elevated temperature conditions, i.e., at room temperature, 350°C, and 700°C. The result revealed that all samples friction coefficient decreases but the wear volume increases with the increased temperature. Also, the AM fabricated sample exhibited a higher wear at room temperature and a reduction in wear with the elevated temperature due to oxidation. Their findings demonstrated that the environmental temperature had a remarkable influence on the wear behaviour of AM-fabricated alloy. Kurdi et al. [63] investigated the sliding wear and friction behaviour of high-performance polymer and polymer composites across wide range elevated temperature conditions. The results revealed that friction coefficient and wear resistance was significantly affected due to the changes in the material deformation mode and interfacial contact conditions with elevated temperature. Also, the development of the transfer films and the transition from brittle to ductile deformation shown on the polymer matrix is primarily temperature dependent. Their findings highlighted the critical influence of environmental temperature to the tribological performance of AM-fabricated high-performance materials.

Overall, the environmental temperature significantly affects the performance of AM parts, including the material stiffness, thermal expansion, and interfacial frictional wear behaviour. Nevertheless, its effect on the tribological performance of high-performance polymers

embedded with complex structures remains unexplored [63], [64], [65]. In the engineering applications, the long-term tribological properties are the key indicators to largely determine the service life of the components. Hence, the thermal exposure facilitated the degradation of the surface and structural integrity of the AM-fabricated functional-design complex structures, thereby compromising the effectiveness in FIV controls. Therefore, systematically investigation on the tribological performance under thermal conditions of AM-fabricated complex structures in high performance polymers is vital to enable and further optimize the AM-fabricated components for thermally demanding environments.

1.6 Thesis outline

Following this chapter, Chapter 2 introduces the material and methods to achieve the proposed objectives of this research thesis, including the sample preparation and design of the re-entrant auxetic structures, post-heat treatment settings, characterization of the mechanical behaviour, friction and wear test setups, and the related microscopy analysis.

Chapter 3 investigates the effect of proposed post-heat treatment on the dimensional accuracy and mechanical properties of 3D-printed neat PLA and PEEK. The dimensional accuracy of the sample before and after the heat-treatment was measured and compared with introduced mean absolute deviation (MAD). Also, the influence of the post-heat treatment on the yield strength and compressive strength of the FDM-printed specimens were measured and compared.

Chapter 4 investigates the effect of proposed post-heat treatments on the tribological performance of the 3D printed neat PLA and PEEK structures. For the first time, the effect of the re-entrant auxetic structure on the tribological performance of polymer-metal sliding system were systematically studied in order to develop a new self-tunning absorber for FIV control. Then, the subsequential effect of post-heat treatment on the tribological behaviour of the printed samples in PLA and PEEK with and without structures were comprehensively investigated.

Chapter 5 investigates the effects of reducing the FIV and wear with FDM-fabricated CFPRs embedded in the re-entrant auxetic structures. The role of CFRPs with complex structure design on the tribological performance under applied loading conditions were studied.

Chapter 6 investigates the effect of environmental temperature on the tribological performance of 3D-printed neat PLA and PEEK structures. The coefficient of friction and wear resistance of selected material filaments incorporating complex structure designs under elevated temperature conditions approaching to their respective own glass transition temperature (T_g) were systemically investigated.

Chapter 7 summarizes the overall research findings from the present work, following with the suggestions to the future research work.

And the cited references are listed in the Reference sections.

Chapter 2 Material and Methods

2.1 Sample Preparation & Design of Re-entrant Auxetic Sample

All samples were fabricated by FDM method. Three different filament materials were selected in this research thesis: neat polylactic acid (PLA) manufactured by eSUN, Shenzhen Esun Industrial Co., Ltd., Shenzhen, China, carbon fibre reinforced polylactic acid (CF-PLA) with milled carbon fibre in a weight fraction of 10% manufactured by Proto-Pasta, Vancouver, WA, USA, and KetaSpire neat polyether ether ketone (PEEK) MS NT1 made by Solvay, Brussels, Belgium. The printer used for printing the neat PLA and CF-PLA are UPBox, manufactured by Tiertime, Beijing, China and Prusa CORE ONE, manufactured by Prusa Research, a.s., Prague, Czech Republic (EU). The neat PEEK was printed with FUNMAT HT made by INTAMSYS, Technology Co., Ltd., Shanghai, China. The diameter of all filaments is 1.75 mm. The printing parameters of three filaments are listed in Table 2.1 below, which are based on our previous study, the recommendation guidelines from manufacturer [109], [170], and the preliminary test to optimize the interlayer bonding and mechanical properties of the printed materials [171], [172].

Table 2.1 Printing parameters of filaments

Filament	**Nozzle Temperature (°C)**	**Bed Temperature (°C)**	**Chamber Temperature (°C)**
Neat PLA	210	60	Room
CF-PLA	220		
Neat PEEK	400	145	90

All wear models were printed in a solid infill with the selection of printing parameters with different orientations. The printing direction of wear model was controlled along the structure direction to maximize the loading bearing capacity of the auxetic structure [173]. Fill angle of 90 degrees was settled for the tensile and compression test specimen.

In this research thesis, the typical complex structure, re-entrant auxetic structure (lattice structure/metamaterials) was selected due to its unique characteristics of Negative Poisson's ratio (NPR), leading to great potentials in applications. In particular, the energy absorption ability and vibration isolation capacity was targeted properties to address the critical challenge of the friction-induced vibration (FIV) under environmental temperature conditions in the tribological applications.

Fig 2.1 demonstrated the design of a single re-entrant unit cell and the associated wear models. As shown in Fig 2.1(a), four parameters are contained in the design of one unit cell: length of re-entrant vertical strut (h), length of re-entrant inclined strut (l), thickness of the strut cross-section (t), and re-entrant angle between the vertical and inclined struts (θ) [174], [175]. In this study, to avoid the influence of other parameters on the negative Poisson's ratios, only the re-entrant angle θ has been changed in this design while others are fixed, as listed in Table 2.2. Here, β is defined as the length ratio of *h/l*.

Table 2.2 Geometry dimension of re-entrant unit design in different angles.

θ (°)	β (mm/mm)	t (mm)
20	2.5	1.5
30		
45		
60		

The choice of the auxetic design was decided based on the considerations of the work of literature and findings in our previous studies [176], [177], [178], [179], [180]. Such a truss based complex structure is well-aligned for the fabrication using FDM with the selection of filaments. Fig 2.1(b) illustrates the design of re-entrant auxetic wear model constructed from the assembly of single re-entrant unit cell shown in Fig 2.1(a). Two main components are composed in the model: the design of upper re-entrant auxetic section for the purpose of vibration reduction, and the lower round plate section for the wear against the steel counterparts. For comparison, a solid benchmark wear model was created by replacing the re-entrant structure with a solid rectangular block of identical external dimensions as depicted in Fig 2.1(c).

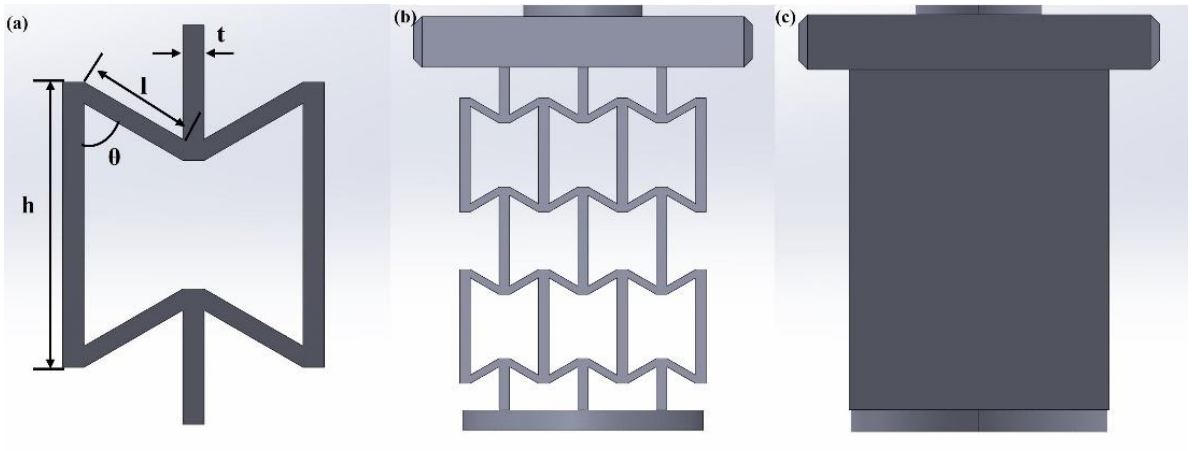

Fig 2.1 Schematics: (a) re-entrant auxetic unit, (b) wear test re-entrant auxetic model, (c) wear test solid benchmark.

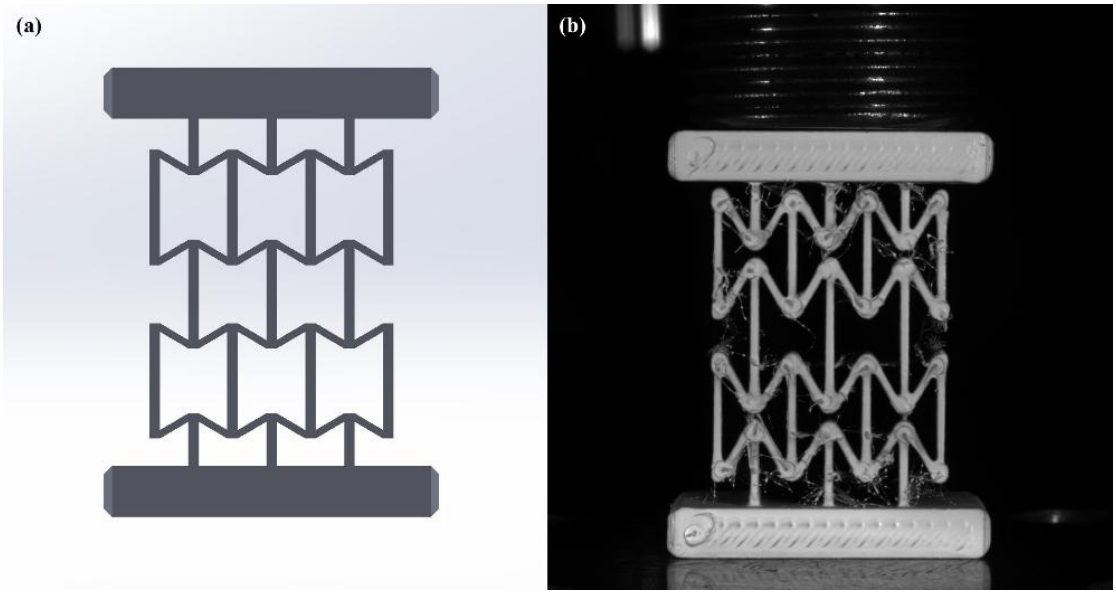

Fig 2.2 The compression test's re-entrant auxetic structure: (a) schematic, and (b) the actual specimen for experimental setup

The Poisson's ratio of each sample was obtained using the ε_{axial} and ε_{trans} as follows:

$$\nu = -\frac{\varepsilon_{trans}}{\varepsilon_{axial}} \quad (1)$$

As the increment of re-entrant auxetic angel θ, the ν_{xy} and ν_{yx} show different trends that when along the x-direction, ν_{xy} becomes more negative, on the contrary; ν_{yx} is closer to 0 [174], [175]. To test and validate the trend of the design in this study, compression tests and FEA simulations were carried out. The compression tests were conducted using Instron 5567 Universal Testing Machines. Fig 2.2(a) and Fig 2.2(b) show the geometry design of specimens and test setup, respectively. During tests, the compression displacement was set to 0.1 mm/sec, and the total testing time of each sample was set to 60 sec. The test was conducted under room temperature. The vertical displacement of the sample was recorded directly from the machine. There was also a camera placed in front of the testing sample to capture the in-situ deformation behaviour of the specimen throughout the compression test every 200ms. Fig 2.3 shows the setup of the FEA model under compressing loadings. Fig 2.3(a) shows the simulation of having a compression load from the lower cylinder along the y-axis, and Fig 2.3(b) shows the simulation of having a compression force on the re-entrant vertical struts along the x-axis. The upper rod in both FEA analysis was fixed.

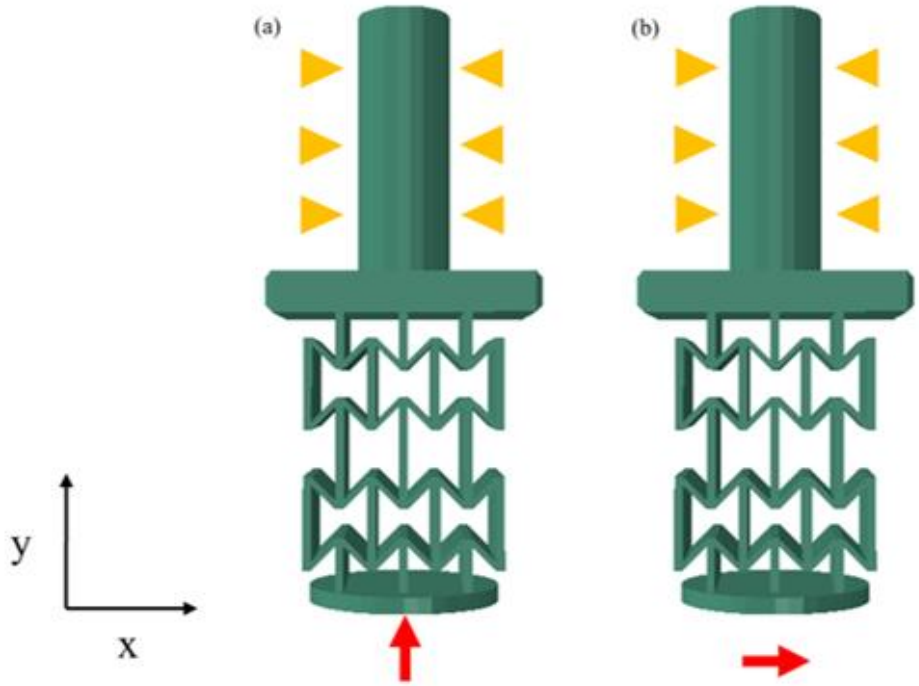

Fig 2.3 FEA test setup: (a) along y-direction, (b) along x-direction

The CAD model was imported into the commercial Finite Element (FE) software Abaqus/Standard for analysis. The model was meshed using linear tetrahedral elements (C3D4 type). A convergence test determined an optimal element size of 0.2 mm. In total, the mesh comprised 320,202 elements and approximately 1,561,422 degrees of freedom. The top cylinder was kinematically constrained, while a displacement-controlled load was applied to the bottom surface. A mesh convergence study was performed using four progressively refined meshes. The results (peak stress) showed minimal variation (<3%) between the intermediate and finest mesh (0.2 mm element size), indicating that further refinement had negligible impact on the outcomes. This confirms that the simulation results are not mesh-dependent and serves as a form of model verification. The material properties of PLA, obtained from existing literature [181] and consideration of the material datasheet provided by the manufacturing, were defined as follows: Young's modulus of 1.973 GPa and Poisson's ratio of 0.35. Fig 2.4 shows the stress/strain distribution within the re-entrant structure under compression and shear loads, respectively. With the strain of information, Poisson's ratios of the structures can be determined. The results were summarized in Table 2.3.

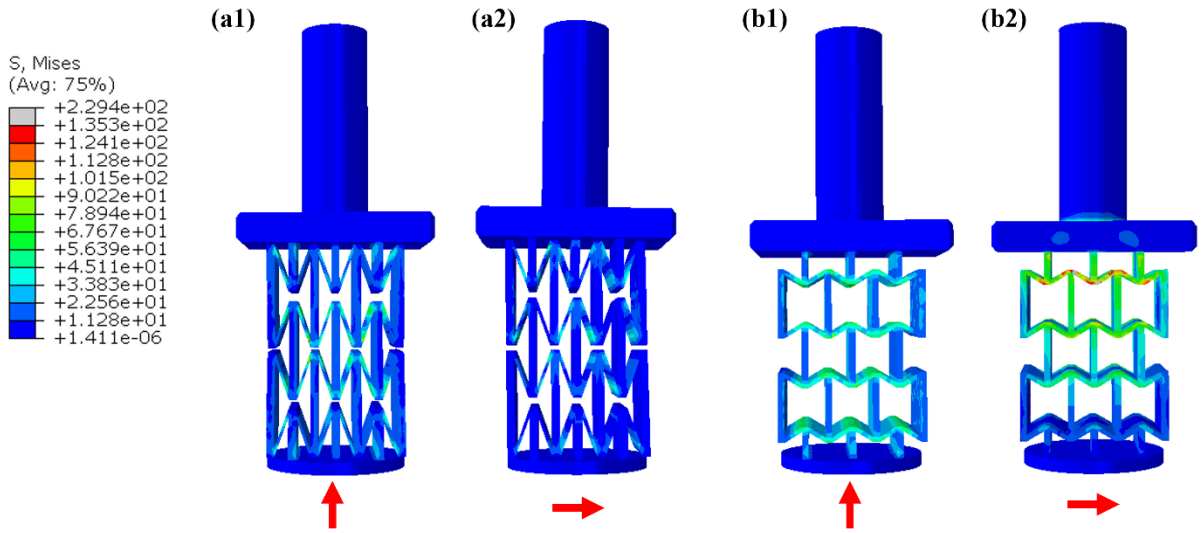

Fig 2.4 The stress distribution of re-entrant auxetic structure: (a1) Re-20 with compressive load, (a2) Re-20 with shear load, (b1) Re-60 with compressive load, (b2) Re-60 with shear load.

Table 2.3 Re-entrant auxetic structure's Poisson's ratio in angles along y- and x- directions

Re-entrant Auxetic Angles	ν_{yx}	ν_{xy}
20°	-0.621	-0.324
30°	-0.459	-0.544
45°	-0.397	-0.808
60°	-0.331	-1.341

2.2 Post-heat Treatment Settings

In this research thesis, annealing or post-heat treatment was selected as a cost-efficient post-treatment method that does not require the high capital investment or expensive consumables associated with other techniques. More importantly, compared with post-processing methods such as chemical smoothing, annealing was shown to improve the overall material properties of the entire volume of the printed part rather than being limited to surface refinement.

The post-heat treatment was conducted in a furnace, named Nabertherm TR60 oven manufactured by Nabertherm GmbH, Lilienthal, Germany. The specific treatment temperature and duration of neat PLA and PEEK was summarized in Table 2.4. The duration and temperature of the specific post-heat for PLA and PEEK was decided in accordance with the thermal properties. For PLA, a single step heat treatment above the glass transition temperature (T_g) was utilized to relieve the residual stress and enhance the crystallinity following established approaches in the literature [182], while considering a relatively low melting temperature typically around 170–180 °C. For PEEK, which has a significantly higher T_g at

143°C and melting temperature at 343°C, a multi-stage heat treatment was applied based on prior studies and manufacturing guidelines [136], [142], [182], [183], [184]. This approach was intended to optimize crystallization and mechanical properties by gradually relieving residual stresses and enhancing material crystallinity. In addition, the incremental temperature increases from 200°C to 220°C helped to control stress relaxation and avoid potential thermal shock associated with rapid temperature elevation.

Table 2.4 Post-heat treatment settings of PLA and PEEK

Sample	Temperature and Duration
Neat PLA	1. Increase from room temperature to 95°C at a rate of 65°C/h 2. Holding 95°C for 1 h 3. Cool down to room temperature
Neat PEEK	1. Increase from room temperature to 120°C at a rate of 60°C/h 2. Holding 120°C for 2 h 3. Increase from 120°C to 200°C at a rate of 80°C/h 4. Holding 200°C for 30 min 5. Increase from 200°C to 220°C at a rate of 60°C/h 6. Holding 220°C for 3 h 7. Cool down to room temperature

2.3 Characterisation of Mechanical Behaviour

2.3.1 Tensile and Compression Test

The mechanical properties of tensile strength were examined using the Instron 3366 Universal Testing machine following the ISO 527-1 standard [185] at the test speed of 50 mm/min. The compressive strength of samples was evaluated by the Instron 5567 Universal Testing machine, following the standard of ASTM D695 [186] at a rate of 1.3 mm/min. Fig 2.5(a) and 2.5(b) shows the design and printed specimens for tensile and compression tests, respectively. For the tensile and compression test, two sets of specimens with and without post-heat treatment were tested and the associated error bars were shown in the corresponding figures. The material specifications of the selected neat PLA and neat PEEK based on the manufacturer's guidelines and datasheets were shown in Table 2.5.

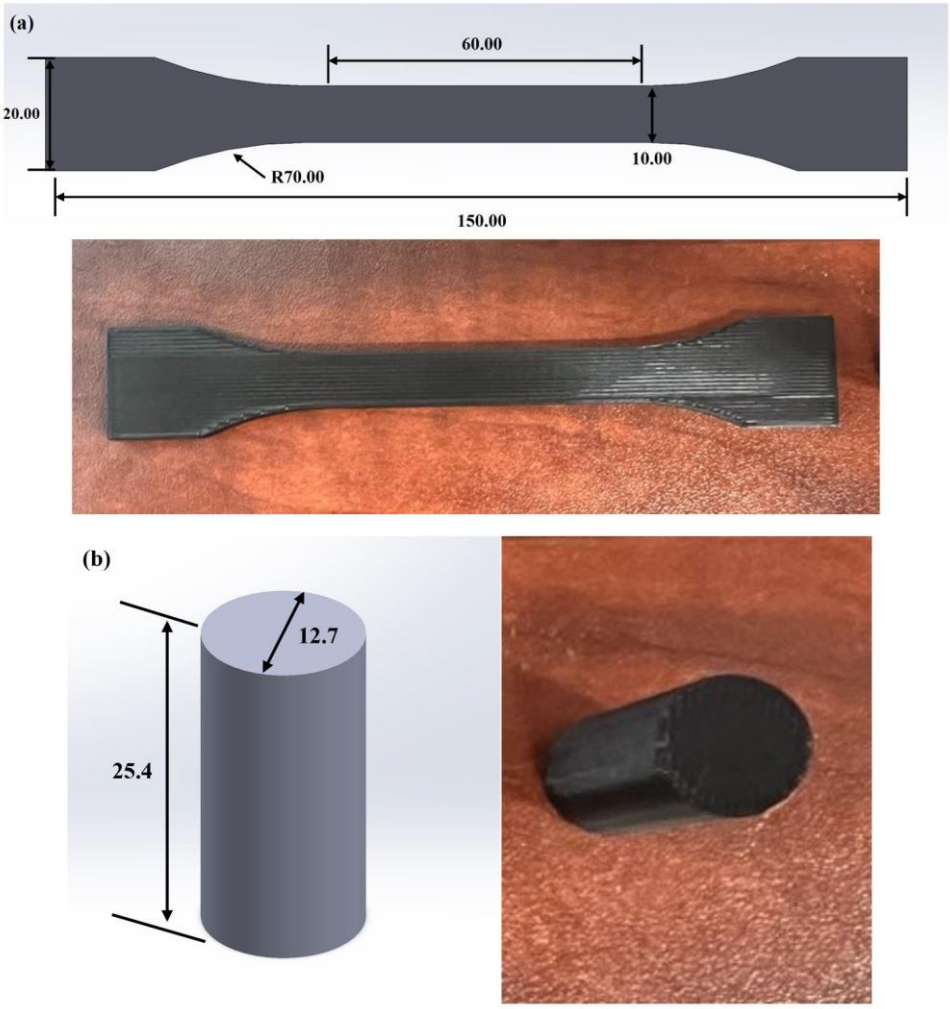

Fig 2.5 Schematic: (a) tensile test specimen and (b) compression test specimen. Dimensions are indicated on the figure in millimeters (mm)

Table 2.5 Material Specifications

	PLA	PEEK
Tensile strength (MPa)	53.34	95
Compressive strength (MPa)	—	118
Flexural strength (MPa)	74	150
Glass transition temperature (°C)	—	150
Melting temperature (°C)	—	340
Melt flow index	5（190°C/2.16kg）	3 (400 °C, 2 16 kg g/10 min)
Density (g/cm³)	1.23	1.30
Poisson's ratio	0.35	0.37

2.3.2 Dynamic Mechanical Analysis

Dynamic mechanical analysis (DMA) was performed on Discovery DMA 850, manufactured by TA Instruments, New Castle, DE, USA, to determine the glass transition temperature (T_g) of neat PLA and neat PEEK. The sample was one-side clamped and tested under the amplitude of 20 μm with the 1.0 Hz of frequency. The sample was in a rectangular shape with the dimensions of 32 mm in length, 6 mm in width, and 2 mm in thickness. The test was performed in a temperature sweep mode. The temperature was ramped from 35°C to 80°C for neat PLA and 35°C to 250°C for neat PEEK. The same ramp rate at 3.0°C/min applied to both filaments. The T_g was determined in accordance with tan δ peak. Two sets of tested samples were fabricated in the materials of neat PLA and neat PEEK.

2.3.3 Differential Scanning Calorimetry

Differential Scanning Calorimetry (DSC) was conducted on DSC 2500, manufactured by TA Instruments, New Castle, DE, USA, to measure the degree of crystallinity of the untreated and heat-treated PEEK based on the equation:

$$X_c = \frac{\Delta H_m}{\Delta H_m^0} \times 100\% \tag{2}$$

Whereas ΔH_m is the enthalpy of melting obtained by the heat flow curve after the baseline correction, and ΔH_m^0 is the enthalpy of fully crystalline PEEK, which is 130 J/g [187].

The sample mass was controlled within the range of 5 mg to 10 mg to ensure the sufficient signal-to-noise ratio while minimizing the thermal lagging. Two sets of the tested PEEK samples before and after the heat treatment were prepared for DSC analysis. The temperature setting and duration of the standard PEEK and the heat-treated PEEK (PEEK-HT) are identical as shown in Table 2.6 below.

Table 2.6 DSC setting for PEEK and PEEK-HT

Sample	Temperature and Duration
PEEK & PEEK-HT	1. Holding room temperature at 20°C for 1 min 2. Increase from 20°C to 380°C in ramp 10°C/min 3. Holding 380°C for 1 min 4. Decrease from 380°C to 20°C in ramp 5°C/min 5, Holding room temperature at 20°C for 1 min

2.4 Friction and Wear Tests

As shown in Fig 2.6, the friction and wear tests were conducted at room temperature using a pin-on-disk configuration with a commercial tribometer NANOVEA-MT/60/NI (Nanovea, Irvine, CA, USA). The steel counterpart was a stainless-steel disk (SKF Gothenburg, Sweden; model LS2542) with an internal diameter of 25 mm and an external diameter of 42 mm. The steel counterpart had a hardness of approximately 910 HV and a surface roughness of about 220 nm. The risk rotation speed was constant at 120 rpm. The sampling rate was 0.2 Hz, indicating one friction and LVDT data point was captured every five seconds. The testing time of wear models in different filament materials was 600/900 minutes. The applied normal load for PLA was 5N, CF-PLA ranging from 5N to 25N, and PEEK at 25N.

The surface area of the wear model was 158.37 mm^2. The specific wear rate (SWR) of the specimen was calculated based on the mass loss during the test in the equation of [188]:

$$SWR = \frac{\Delta m}{\rho \cdot F_N \cdot L} \tag{3}$$

Where Δm denotes the mass loss, ρ is the material density, F_N is the normal force, and L is the sliding distance.

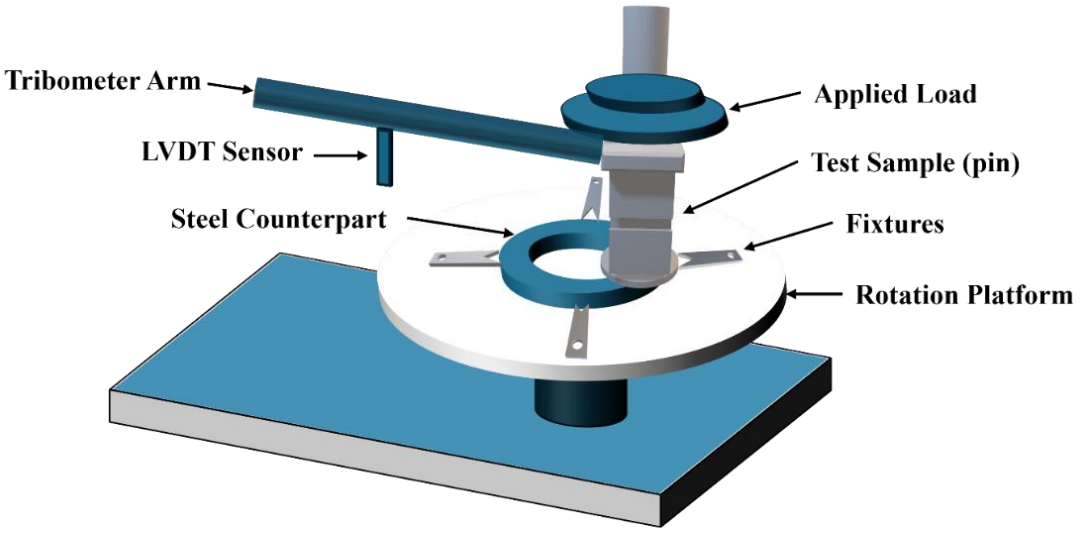

Fig 2.6 Schematic of pin-on-disk wear test machine and setup

To measure friction-induced vibration in the vertical direction, a linear variable differential transformer (LVDT) sensor was mounted on the wear testing machine to track vertical displacement of the sample during the test, as also shown in Fig 2.6. Fig 2.7(a) presents a

representative curve showing height variation as a function of sliding time. The curve represents the wear re-entrant auxetic model at a 60-degree angle, printed with PLA. Since material wear leads to a decrease in sample height, the displacement data generally increases over time. The slope of this curve indicates the time-dependent wear rate, $w_t = \Delta h/t$ where as Δh refers to height loss and t denote time. To analyse vibrations separately from wear, the absolute value of the immediate displacement change, $|\Delta y_i|$ (see Figure 2.7a), was used to determine the vibration amplitude. It is assumed that, over very short time intervals, wear is negligible; therefore, fluctuations in displacement during these intervals primarily reflect the system's vibration behaviour.

The average vibration amplitude is calculated using the following expression:

$$AV = \frac{\sum_{i=1}^{n} |\Delta y_i|}{n-1} = \frac{\sum_{i=1}^{n} |(y_{i+1} - y_i)|}{n-1} \quad (4)$$

where y represents the displacement measured between the LVDT sensor and the sample.

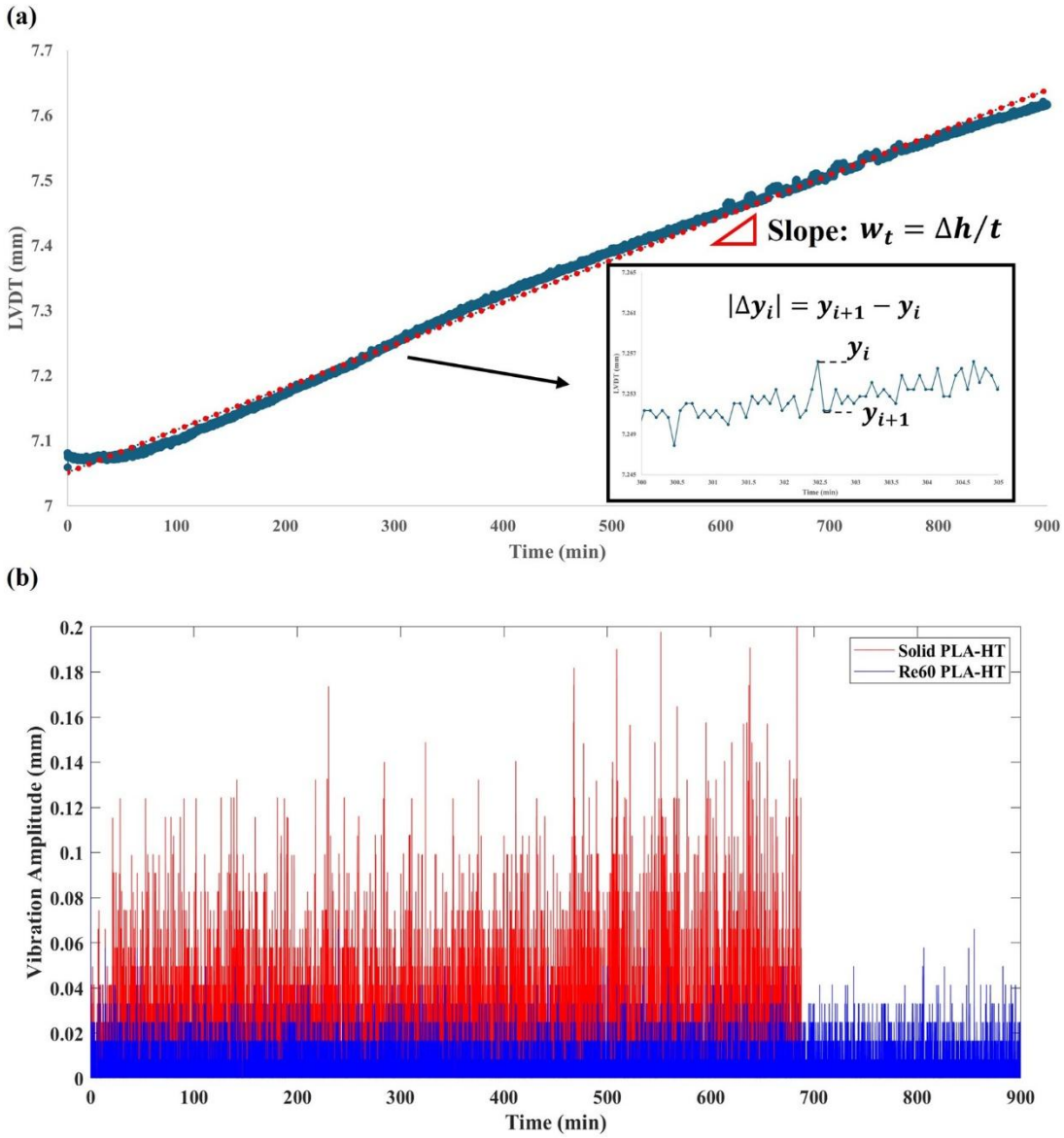

Fig 2.7 Vibration amplitude (a) LVDT results; a linear trend line (the "dotted line linear fitting") has been applied to data points and the slope of this fitted line then quantifies the rate of wear height loss per unit of time; (b) derived vibration amplitude curve for PLA-HT (heat treated) solid bench-mark (Solid PLA-HT) and PLA with the embedded re-entrant auxetic structure (Re60 PLA-HT) at the load of 5 N.

Based on this approach, the corresponding vibration amplitude curve derived from Fig 2.7(a) is shown in Fig 2.7(b), which indicates an average vibration amplitude of 0.00111 mm. For comparison, the average vibration amplitude of the solid benchmark is also given in Fig 2.7(b), with a value of vibration amplitude equal to 0.00279 mm. To further evaluate the vibration absorption performance of the re-entrant auxetic structures, the relative Absorbed Vibration

Percentage (AVP) with respect to the solid benchmark was introduced and calculated as Equation (5):

$$AVP = \frac{Solid_{vibration\ amplitude} - Re_{vibration\ ampltiude}}{Solid_{vibration\ amplitude}} \times 100\% \quad (5)$$

Thus, for the results shown in Figure 2.7, the AVP is determined to be 60.2% for the PLA specimen with the embedded re-entrant auxetic structure. This approach allows for the quantitative analysis of FIV in the presence of the re-entrant structures under the specified sliding conditions.

2.5 Microscopy Analysis

After the wear tests, the surface morphology of the worn samples was examined using a Phenom XL Desktop SEM (Thermo Scientific, Waltham, MA, USA). The scanned image provided detailed characteristics of the carbon fibre condition, fibre-matrix interface, wear tracks and the wear debris morphology on the worn surfaces of the sample corresponding to the changes of applied loads. The SEM equipment also enables to conduct Energy-dispersive X-ray spectroscopy (EDS) analysis to examine the elemental composition of the selected regions. The surface roughness analysis of the worn specimens and metal disk rings was examined with Olympus LEXT 5000 – 3D laser confocal (Olympus Corporation, Hachioji, Tokyo, Japan). An Asylum Jupiter XR Material atomic force microscopy (AFM; Asylum Research, Santa Barbara, CA, USA) was used to investigate the detailed surface morphology of the steel counterpart at a nanoscale. The surface profile combining the confocal and AFM measurements demonstrated the surface with minor but distributed asperities in order to acquire the fine scale (microscale and nanoscale) roughness corresponding to the sample's surface morphology.

Chapter 3 Effects of post-heat treatment on the dimensional accuracy and mechanical properties of 3D printed PLA & PEEK

In this Chapter, post-heat treatment was applied to investigate the effects on the dimensional accuracy and mechanical properties of 3D-printed polymer components. As discussed above, the post-heat treatment employed the controlled thermal exposures to activate and enhance the movement of the polymer chain, thus facilitating the recrystallization of crystalline and semi-crystalline polymers [136], [137]. In parallel, the residual stress was relieved during this post processing, leading to improvement of interlayer boding and mitigate the internal FDM-printed defects [138], [139], [140]. In accordance with the distinct thermal dynamic properties of different polymers, such as glass transition temperatures and kinetics of crystallization, specific material-depended post-heat treatment strategies are necessary to the FDM fabrications. Therefore, two polymers, i.e., polylactic acid (PLA) and polyether ether ketone (PEEK), were used as base materials. The selection of PLA and PEEK represented the typically thermoplastic thermal and mechanical features, which enabled the comparative assessment of the effect of post-heat treatment across the range from commonly-used to high performance polymers. The investigations on the dimensional accuracy and mechanical properties after the heat treatment were to ensure the targeted material strength achieved while controlling the dimensions within the tolerances.

The result revealed that the post-heat treatment induced systematic shrinkage of the printed specimen, while simultaneously effectively enhanced the mechanical properties of both materials by increasing their elastic modulus and yield strength. Specifically, the heat-treated sample had an increased mean absolute deviation (MAD) from 0.141 mm to 0.263 mm, indicating the increased dimensional deviations and highlighting the necessity for controlling the warpage induced by thermal shrinkage, particularly in the long-thin specimen. Further, the tensile and compressive strengths of heat-treated PLA increased from 44.14 MPa to 47.66 MPa and from 68 MPa to 82 MPa, respectively. A similar trend was observed for heat-treated PEEK, with tensile strength increasing from 75.53 MPa to 84.91 MPa and compressive strength from 106 MPa to 123 MPa. However, the post-heat treatment also reduced the ductility of PLA while enhancing the ductility of PEEK.

3.1 Heat-treatment effects on the dimensional accuracy of printed polymers

The dimensional accuracy of the tensile PEEK specimen was measured as shown in Fig 2.5 before and after the proposed heat treatment demonstrated in Table 2.4. In particular, the overall length, width, and the thickness of each printed specimen was measured with vernier calliper. Further, multiple locations were selected on each specimen, and the dimension deviation (Dev.) in millimetres from the CAD design was quantified through 3D scanning. The minus sign "–" indicates the printed specimen is smaller than the design value. The results were summarized in Table 3.1 and Fig 3.1 below.

Table 3.1 Measured printed dimensions of specimen before and after heat treatment

Sample	Length (mm)	Width (mm)	Thickness (mm)
Sample before heat treatment	149.35	4.11	20.30
Sample after heat treatment	148.82	4.09	19.47

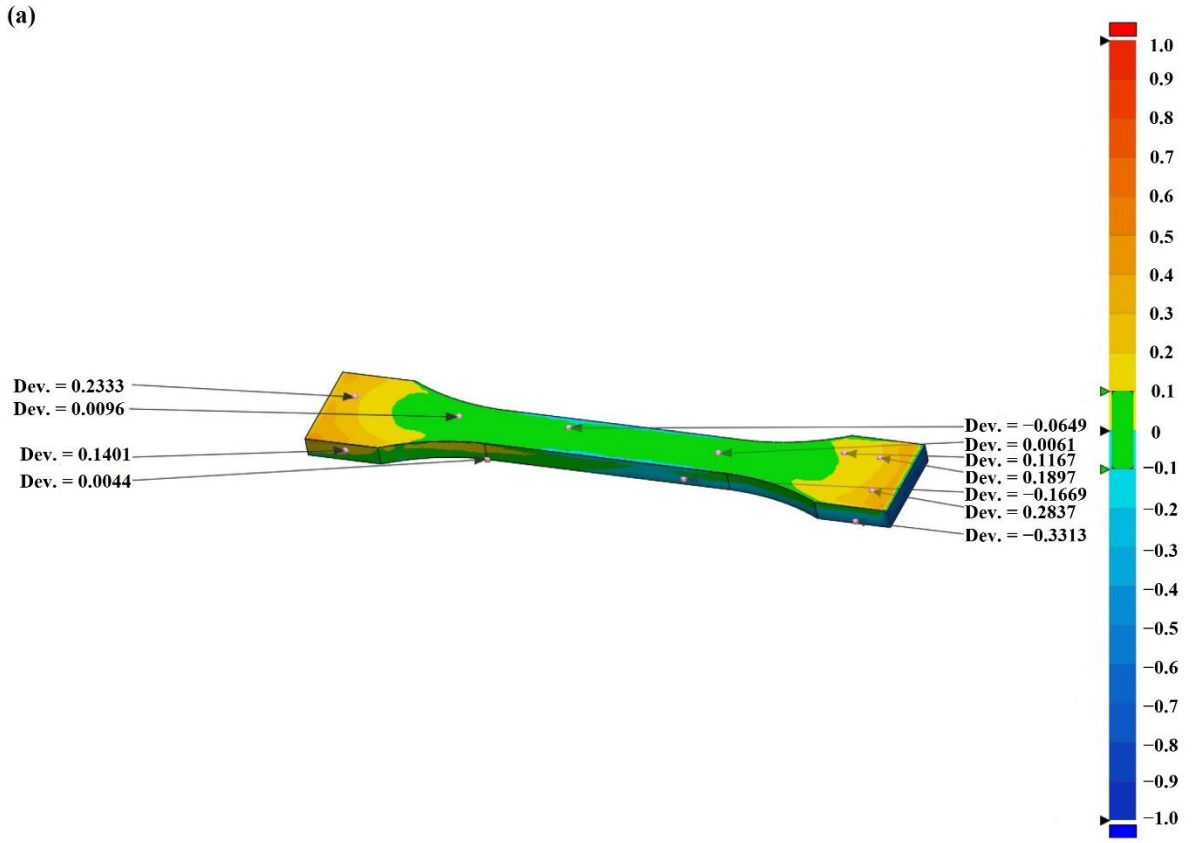

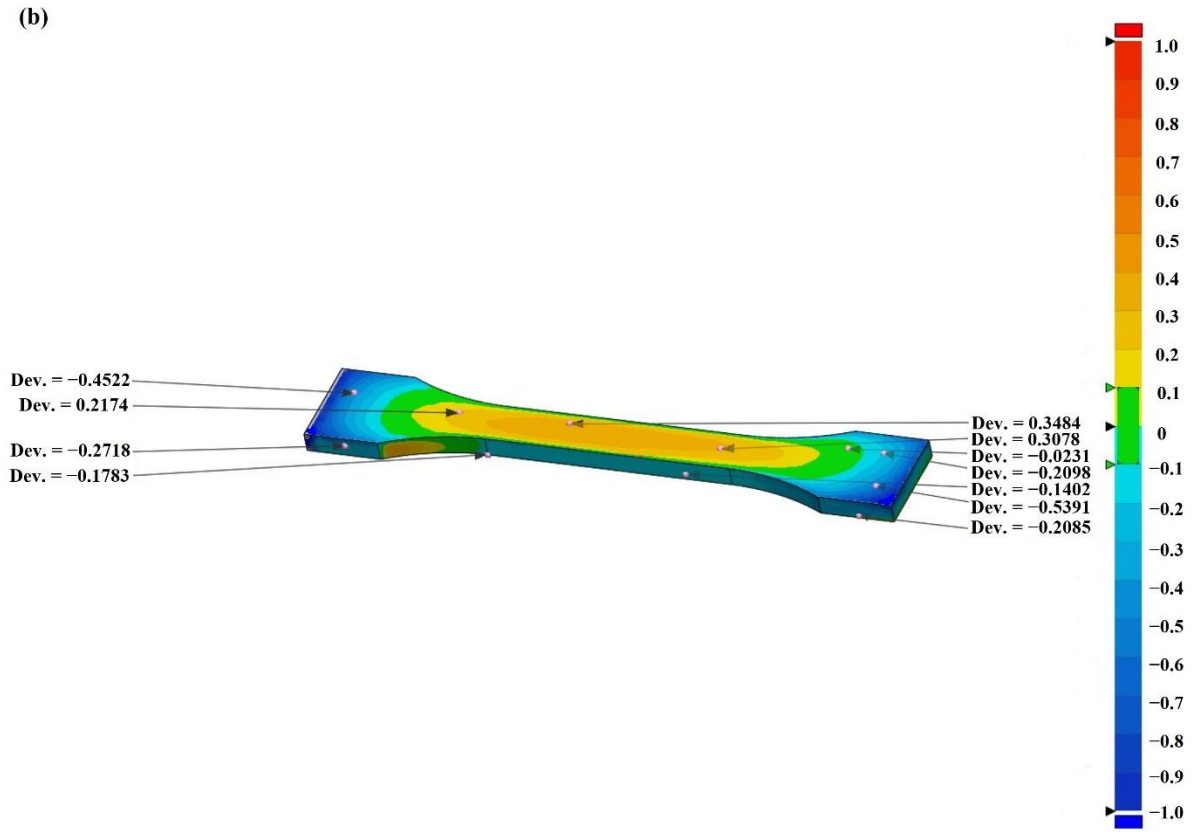

Fig 3.1 Dimension deviation (Dev.): (a) sample before heat treatment, (b) sample after heat treatment

As shown in Fig 3.1(b), the specimen after heat-treatment had more distributions of the negative Dev. (dimension deviation) compared with the standard specimen. To remove the sign bias and directly quantify the dimensional accuracy of the printed specimens, the MAD (mean absolute deviation) was introduced and calculated as follows,

$$MAD = \frac{1}{n}\sum_{i=1}^{n}|\Delta D_i| \tag{6}$$

Where $\Delta D_i = D_i - \Delta D_{CAD}$ is the dimensional deviation at location i. In this case, the ΔD_i is the numbers shown Dev. Value in Fig 3.1. n is the number of measurement points.

The statistical evaluation of the dimensional accuracy revealed that the heat-treated PEEK specimen had an increased mean absolute deviation at 0.263 mm compared to the standard PEEK specimen with 0.141 mm, indicating a systematically shrinking of the sample due to the post-heat treatment [189]. Although the post-heat treatment resulted in a higher dimensional deviation, the observed Dev. shown in Fig 3.1(b) were uniformly directional, i.e. a

predominantly distribution of negative signs. This observation was consistent with the negative strain dimensional changes with the thermally treated printed polymers, which was associated with the crystallization-induced volumetric shrinkage and relieve of the residual stress [189], [190], [191]. This highlighted the necessity of implementing the control methods to control the negative strain dimensional changes, particularly in the long-thin designs to avoid the adverse impact on the subsequent mechanical properties, for instance by placing a lid above the sample during the post-heat treatment. The finding demonstrated that the post-heat treatment or annealing induced a systematic shrinkage due to the increased degree of crystallinity and thermal stress relaxation, which should be accounted and controlled during the post-processing the FDM-printed parts, particularly in the elongated-thin design.

3.2 Heat-treatment effects on mechanical properties of printed polymers

3.2.1 Thermal-mechanical properties of printed polymers

DMA tests were conducted twice for both PLA and PEEK, with the dimensions in millimeters of each test specimen indicated in the upper right corner shown in Fig 3.2. Fig 3.2(a) presents the DMA results, illustrating the viscoelastic transition behaviour of PLA filaments as the temperature increases. The loss modulus exhibits a distinct peak, indicating maximum energy dissipation at the glass transition temperature (T_g), which corresponds to the tan δ peak at approximately 61.91°C. Concurrently, the storage modulus shows a pronounced decline near T_g due to the onset of large-scale molecular chain mobility.

In contrast, PEEK illustrated a different viscoelastic behaviour shown in Fig 3.2(b). The storage modulus decreased more gradually with the increased of temperature, indicating excellent thermal stability. The loss modulus of PEEK occurred at a significantly higher temperature T_g of 151.16°C with a broader and less pronounced transition as PLA presented in Fig 3.2(a), indicating a more restricted molecular chain mobility.

Overall, these differences in viscoelastic behaviour and results are consistent with values reported in the literature [192], [193] and provide guidance for selecting the post-heat-treatment temperatures provided in Table 2.4.

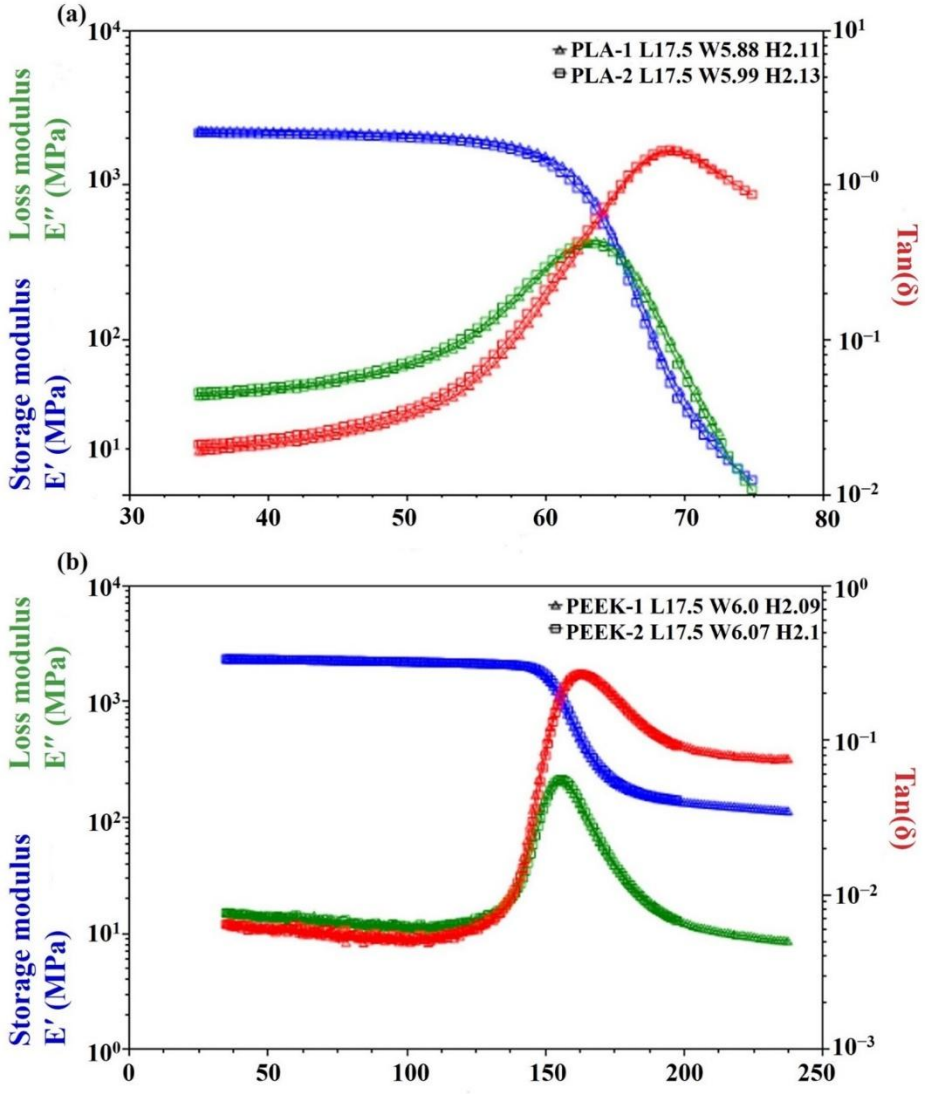

Fig 3.2 DMA Result: (a) PLA, (b) PEEK

3.2.2 Effects of Post-Heat treatment

Fig 3.3 compares the mechanical properties of the printed PLA samples before and after post-heat treatment. After baking at 95°C for 1 h, the strength increased by approximately 10%. For both treated and untreated samples, the printed specimens exhibited higher compressive strength than tensile strength, which can be attributed to void defects introduced during the printing process. Accordingly, the representative tensile stress–strain curves of PLA are shown in Fig 3.4. It is observed that the elongation at break decreased after heat treatment, indicating reduced ductility, as demonstrated in Fig 3.4. This observation is consistent with previous studies, which indicated the heat-treatment of FDM-printed PLA influences the degree of crystallinity and layer bonding situation [194]. The process enhances the chain mobility of the amorphous regions, facilitating the crystallization process, lamellar thickening and promoting

the interlayer diffusion. As a result, the collectively effects contribute to the enhancement in the tensile strength and material stiffness [182]. However, these studies also highlighted the trade-off between the balance. The excessive crystallization can disrupt the uniformity of the amorphous phase and introduced the microstructural heterogeneities, which resulted in the stress concentration sites and decreased ductility [194]. This explains the results observed in Fig 3.4.

For PEEK, the mechanical strength was also enhanced after post-heat treatment, as shown in Fig 3.5. The characteristic tensile stress–strain curves of the untreated and heat-treated PEEK materials are presented in Fig 3.6. It was observed that ductility increased following heat treatment. In general, improvements in mechanical properties such as strength and modulus can be attributed to an increased degree of crystallinity and enhanced interlayer bonding [136], [195], [196]. However, the effect of heat treatment on the ductility of PEEK is more complex. As reported by Yang et al. [136], the ductility of printed PEEK initially decreased as crystallinity increased from 16% to 18%, but subsequently increased with further increases in crystallinity from 19% to 21%.

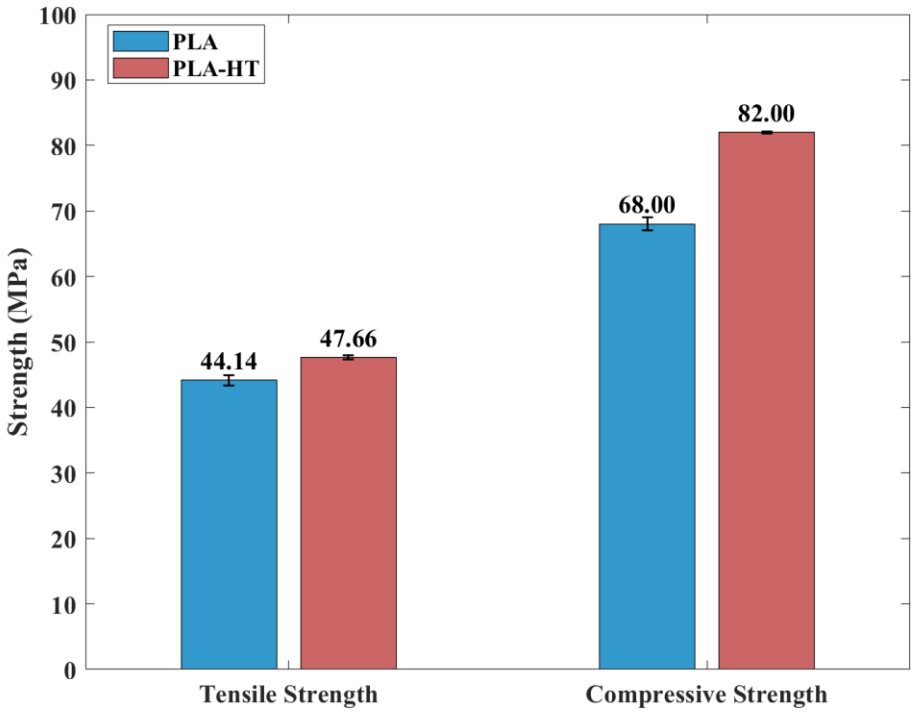

Fig 3.3 Yield strength and compressive strength of PLA with and without post-heat treatment

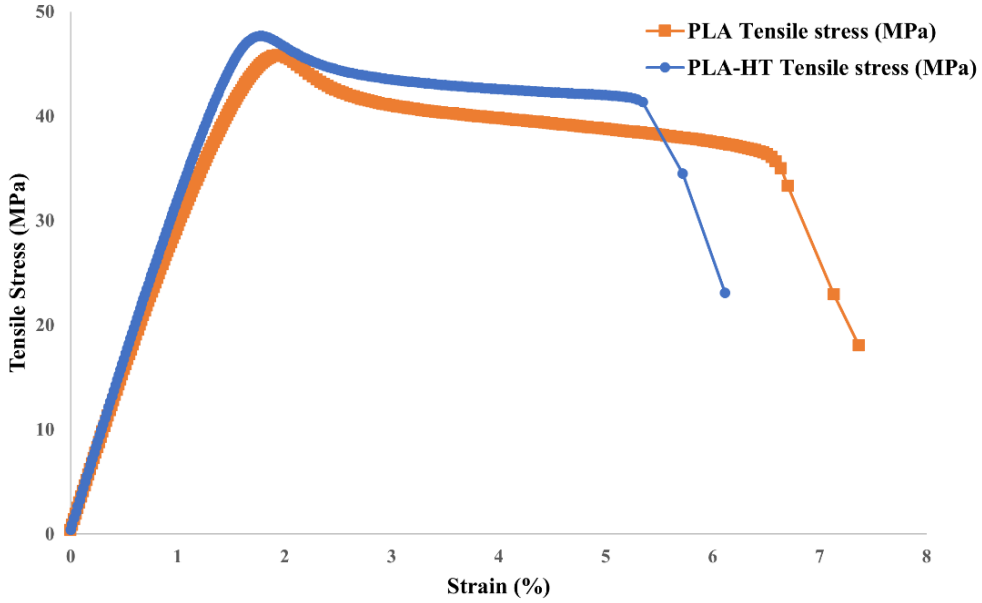

Fig 3.4 Stress-strain curve of neat PLA with and without post heat treatment

To quantify the crystallinity of the printed PEEK materials, DSC tests were conducted, and the results are summarized in Fig 3.7. Using Eq. (2), the degree of crystallinity of standard PEEK was calculated to be 21.8%, which increased to 24.0% after post-heat treatment, as listed in Table 2.4. These results are consistent with the findings reported by Yang et al. [136], i.e. ductility increases with crystallinity when crystallinity is higher than 19%. Nevertheless, it should be noted that, in addition to crystallinity, other factors such as residual stress, internal defects, and structural distortion induced by heat treatment may also influence the elongation at break of printed PEEK. In particular, high residual stresses can be introduced during the printing process due to the relatively high processing temperature. Annealing can effectively relieve these residual stresses, which, together with increased crystallinity and improved interlayer bonding, may account for the observed enhancement in ductility of the printed PEEK materials.

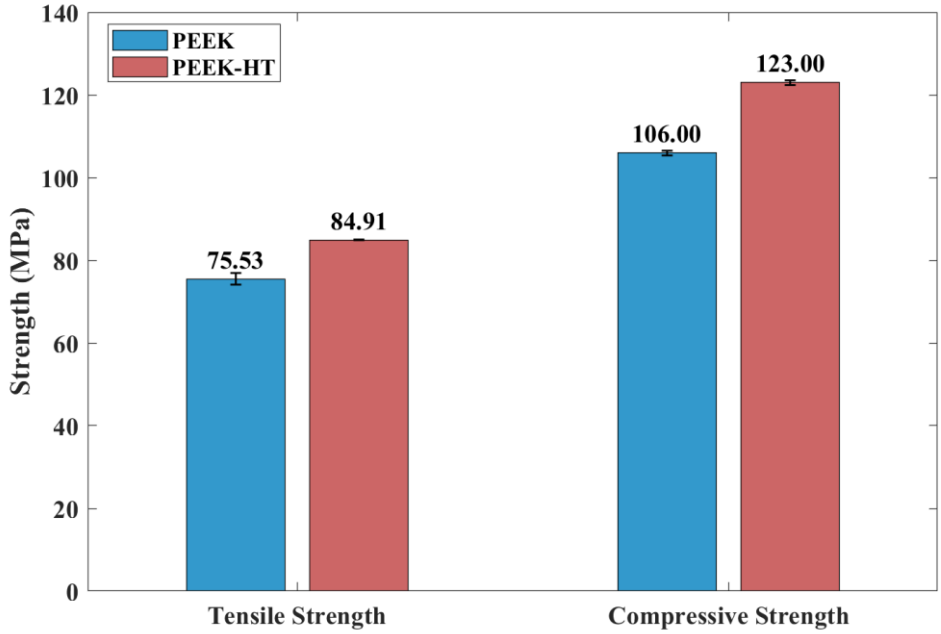

Fig 3.5 Yield strength and compressive strength of PEEK with and without post-heat treatment

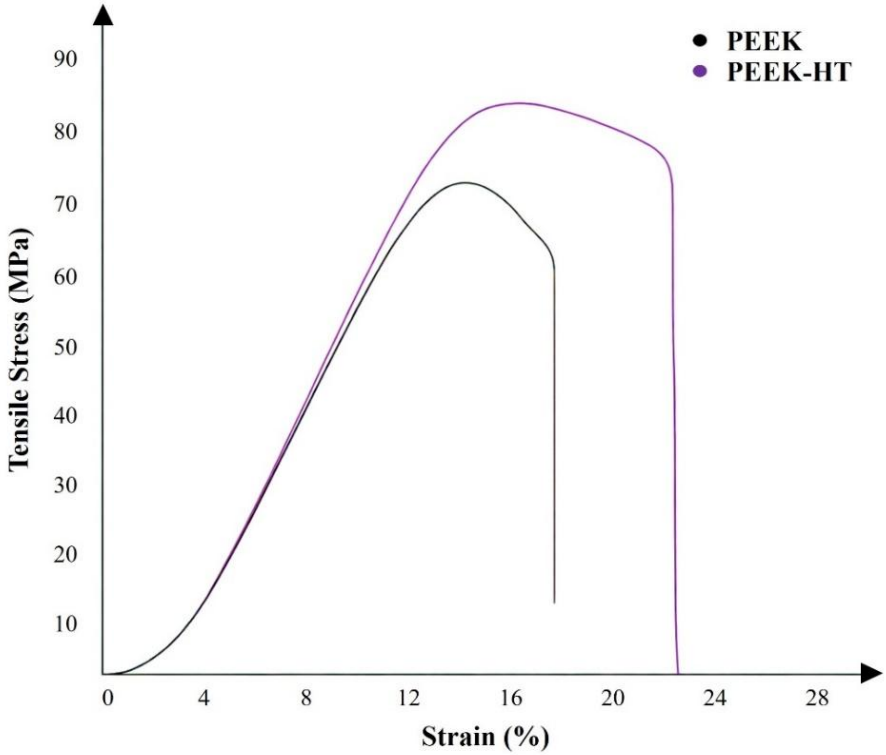

Fig 3.6 Stress-strain curve of neat PEEK with and without post heat treatment

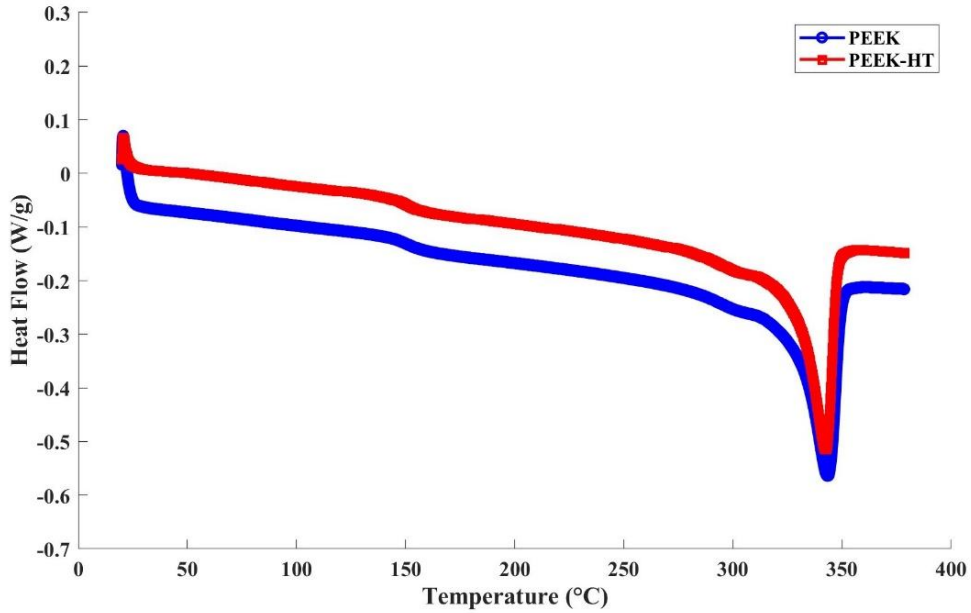

Fig 3.7 The DSC result of PEEK with and without post-heat treatment.

3.3 Conclusions

This chapter investigated the effects of the post-heat treatment on the dimensional accuracy and mechanical properties of FDM-printed PLA and PEEK materials. In particular, the dimensional deviation and mechanical performance of printed specimens were comparatively evaluated. The following conclusions can be drawn:

1. The proposed heat treatment resulted in an increased MAD from 0.141 mm to 0.263 mm, leading to the systematic shrinkage of the printed specimen due to the increased degree of crystallinity and relieve of internal stress. It is necessary to account for this change and implement the control methods particularly for the elongated-thin design.
2. The proposed heat treatment resulted in higher degrees of crystallinity and, consequently, improved strength for both printed materials. For PLA, heat treatment increased the tensile strength from 44.14 MPa to 47.66 MPa, while the compressive strength improved from 68 MPa to 82 MPa. A similar trend was observed for heat-treated PEEK, with tensile strength increasing from 75.53 MPa to 84.91 MPa and compressive strength improving from 106 MPa to 123 MPa. Nevertheless, post-heat treatment reduced the ductility of PLA while enhancing the ductility of PEEK.

Chapter 4 Effects of post-heat treatment on tribological properties of 3D printed PLA & PEEK structures

In previous chapter, experimental studies have been systematically conducted on the investigation of the effects of post-heat treatment on the dimensional accuracy and mechanical properties of the FDM-printed neat PLA and neat PEEK. It can be seen that post-heat treatment induced the systematically shrinkage of the printed samples, while simultaneously effectively enhanced the mechanical performance of the printed polymers by increasing their elastic modulus and yield strength. Nevertheless, the impact of post-heat treatment on the time-dependent tribological performance of materials, particularly in complex structures remain limited [35], [36]. While it is often assumed that improvements in mechanical properties lead to enhanced tribological performance, tribological properties are not intrinsic material properties and instead depend strongly on the specific system and operating conditions in which a material or structure functions.

Therefore, in this Chapter, the effects of re-entrant auxetic structure's on friction-induced vibrational behaviour of 3D-printed PLA samples was systematically investigated at first. We explored the use of re-entrant auxetic structures via 3D printing as novel self-tuning absorbers for mitigating friction-induced vibrations (FIV) [109]. The study demonstrated the potential of the re-entrant structure in suppressing FIV of neat PLA sliding against steel counterparts. However, stress concentrations and printing defects in the printed structures can compromise energy absorption efficiency and load-bearing capacity. Building upon this and aforementioned research limits, for the first time, post-heat treatment is applied to complex tribological components incorporating embedded re-entrant auxetic structures fabricated with FDM. Annealing was selected as a cost-efficient post-treatment method that does not require the high capital investment or expensive consumables associated with other techniques. More importantly, compared with post-processing methods such as chemical smoothing, annealing was shown to improve the overall material properties of the entire volume of the printed part rather than being limited to surface refinement. The influence of the proposed heat treatment on the tribological properties of the printed base materials and structures was systematically investigated. This work contributes to the advancement of heat treatment processes for thermoplastics, offering guidance for their application in a wide range of tribological applications and leveraging the capabilities of modern additive manufacturing techniques [197].

4.1 Determine the Poisson's Ratios of Printed Re-entrant Structures

To validate the simulation results shown in Table 2.3, Poisson's ratio of the printed re-entrant structures was also measured under compression tests. Fig 4.1 shows the deformation response of one re-entrant structure under the compression test. The analysis of Digital Image Correlation (DIC) and Tracking system was used to trace the deformation changes in the horizontal (x) direction of the structure by measuring the displacement of a pair of points e.g., points 3 and 4 [198]. The overall deformation in structure is determined by the average values extracted from multiple pairs of points. The selection of points at different locations was decided by considering the effects of material variability and model complexity of the re-entrant structure [199]. Thus, the strains of the tested structure in axial and transverse directions, i.e. on ε_{axial} and ε_{trans} can be determined. Accordingly, Poisson's ratio can be calculated according to Eq. (1). Fig 4.2 summarizes Poisson's Ratios of the printed re-entrant structures as a function of the auxetic angle θ. The simulation results were also given in the figure for the comparison. A good agreement between the simulation and experimental was observed, which as the increment of angle θ, the value of ν_{yx} becomes less negative. While the simulation values exhibit slightly higher estimations, this can be explained by imperfections in the printed specimen. More deformation occurs in the horizontal direction due to the buckling deflection in the vertical struts, whereas such deflection was neglected in the simulation model with the ideal geometric structures used.

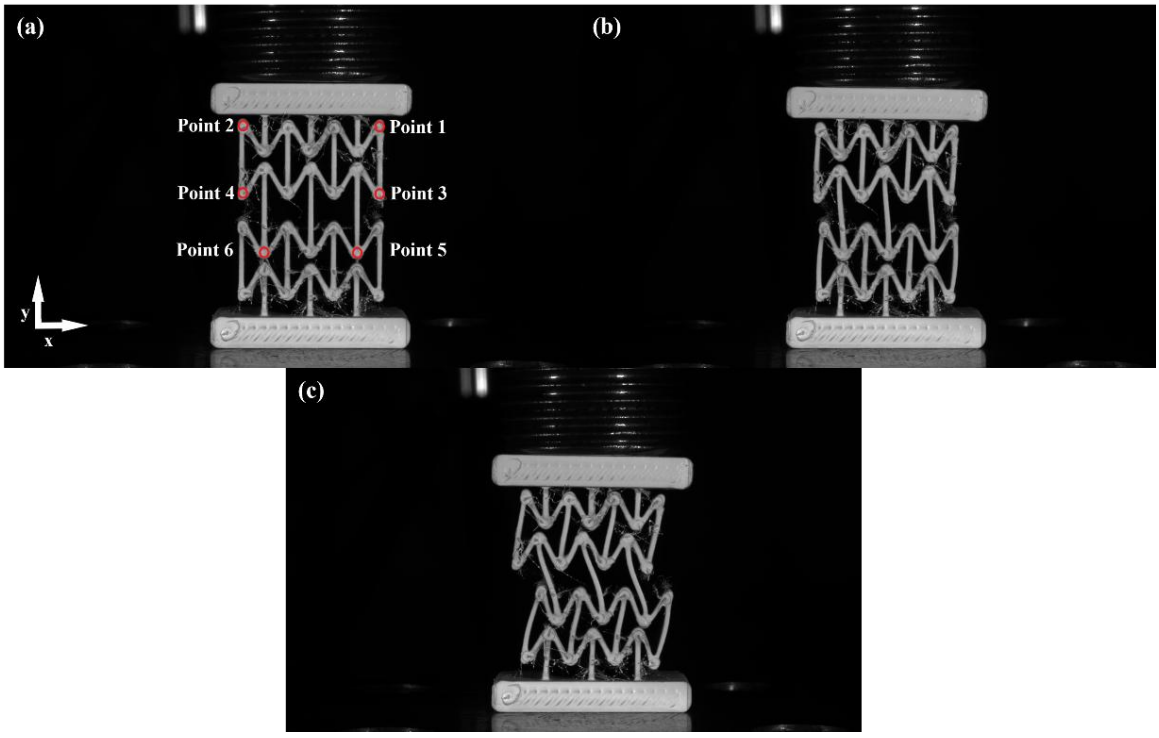

Fig 4.1 Deformation responses of the compression test of re-entrant auxetic structure in 30-degrees along y-direction: (a) under relaxing condition; (b) with deformation strain reaching ~ 80% maximum elastic strain and (c) fully yielding

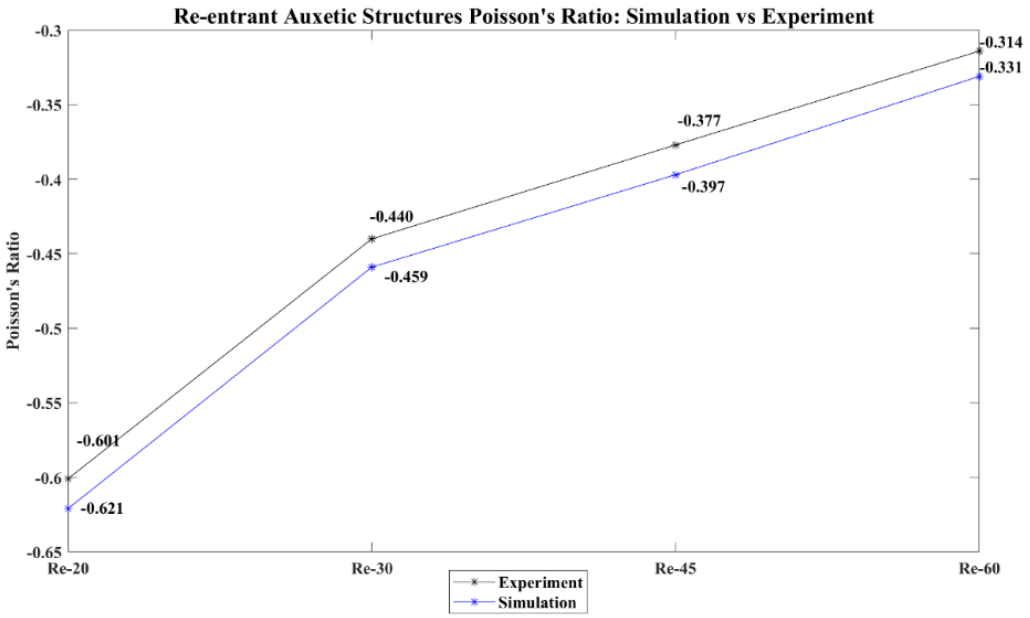

Fig 4.2 The experimental and simulation results of re-entrant auxetic Poisson's ratio along y-direction

4.2 Coefficient of Friction Results and Friction-induced Vibration Analysis

4.2.1 Coefficient of Friction Results

Fig 4.3 compares the typical friction processes of printed specimens with and without the induced re-entrant structures shown. It can be seen that CoF slightly increased at the initial sliding process within ~ 300 minutes, which can be explained by the increased real contact area due to the wear loss at roughness asperities. After that, the friction process for the sample without re-entrant structure showed large fluctuations, whereas a rather stable CoF pattern was achieved by the specimen with the re-entrant structure having an auxetic angle of 60°. Further, the average CoF at the steady stage was also reduced with the presence of re-entrant structures. Fig 4.4 summarizes the average CoF of all the printed specimens. Here, the average CoF was calculated after running for 300 minutes when each sample reaches its steady state. It can be seen that the lower friction was achieved by the re-entrant structure with larger auxetic angles, i.e. more negative Poisson's ratios in the sliding direction (cf. Table 2.3).

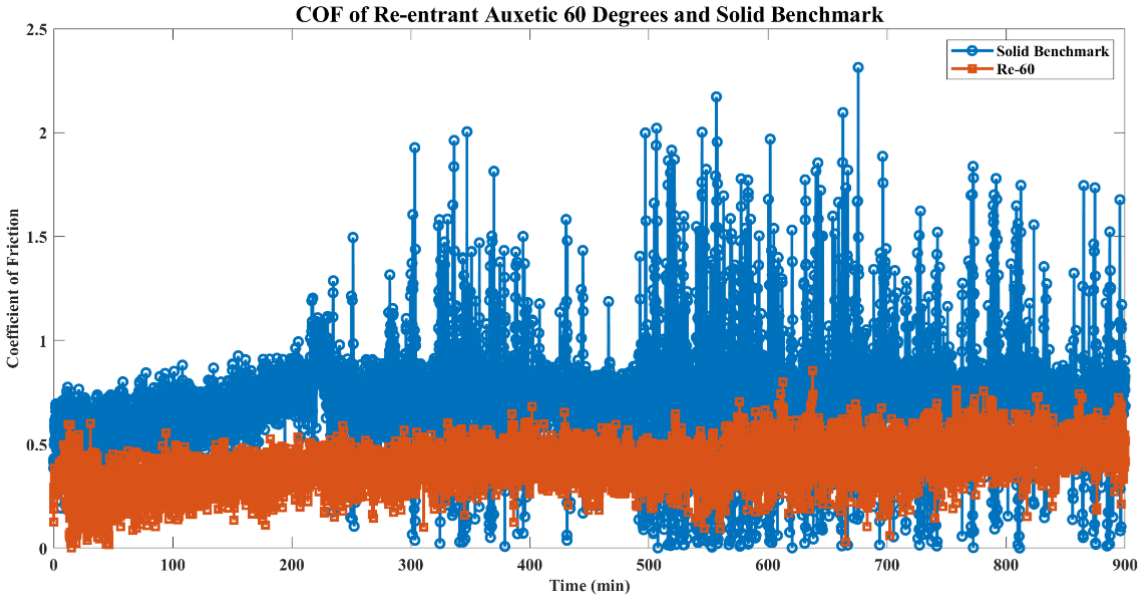

Fig 4.3 CoF of re-entrant auxetic 60 degrees and the solid benchmark

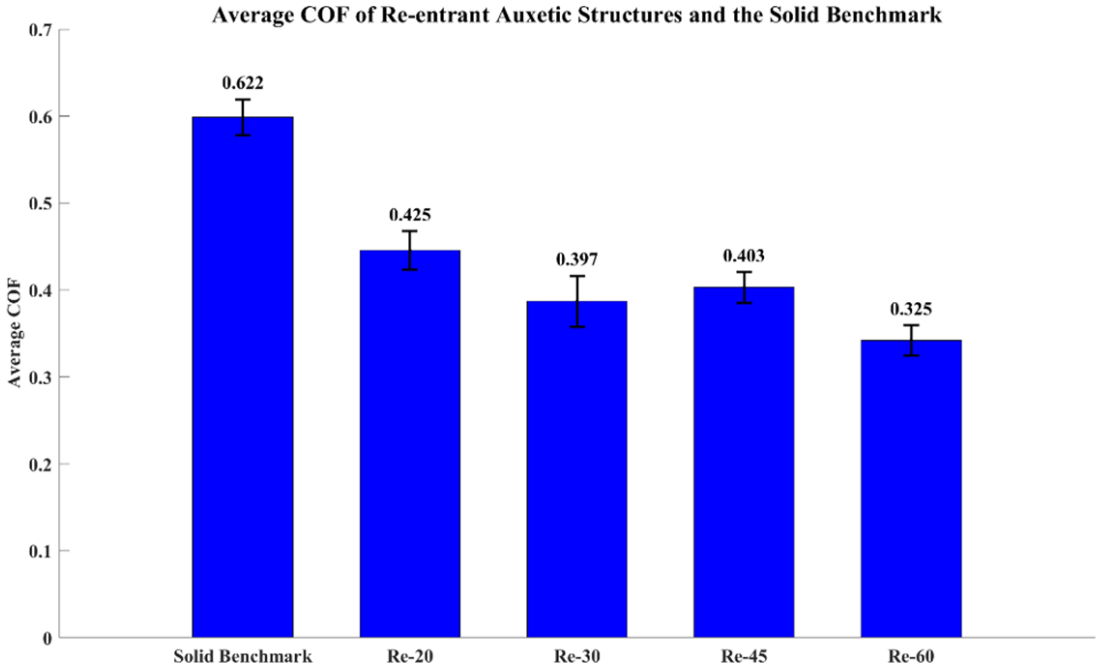

Fig 4.4 Average CoF of re-entrant auxetic structures and the solid benchmark

4.2.2 The effects of Re-entrant structures on the friction-induced Vibration

As can be seen in Fig 4.3, significant fluctuations in CoF were observed, which are often associated with vibrations in the sliding system [200], [201]. In this paper, the vibration amplitude is calculated using the displacement of sliding samples in the vertical direction, according to Eq. (4). Fig 4.5 compares the vibration behaviour of the sliding samples with and

without re-entrant structures. It was noticed that with the re-entrant structure, the friction-induced vibration is significantly suppressed. Auxetic 60 degrees exhibits the highest AVP of absorbing friction-induced vibration at 57.73% compared to other samples according to Eq. (5), thanks to the vibration absorption capability of the re-entrant structures [159], [160]. Table 4.1 compares the friction-induced vibration behaviour of all the samples. It is interesting to note that the friction-induced vibration is more effectively reduced by the re-entrant structures having higher auxetic angles i.e. a more negative value of NPR in the horizontal direction (cf. Table 2.3). This agrees with the conclusion drawn by Pan et al. [159] that more negative Poisson's ratio provides better vibration isolation ability.

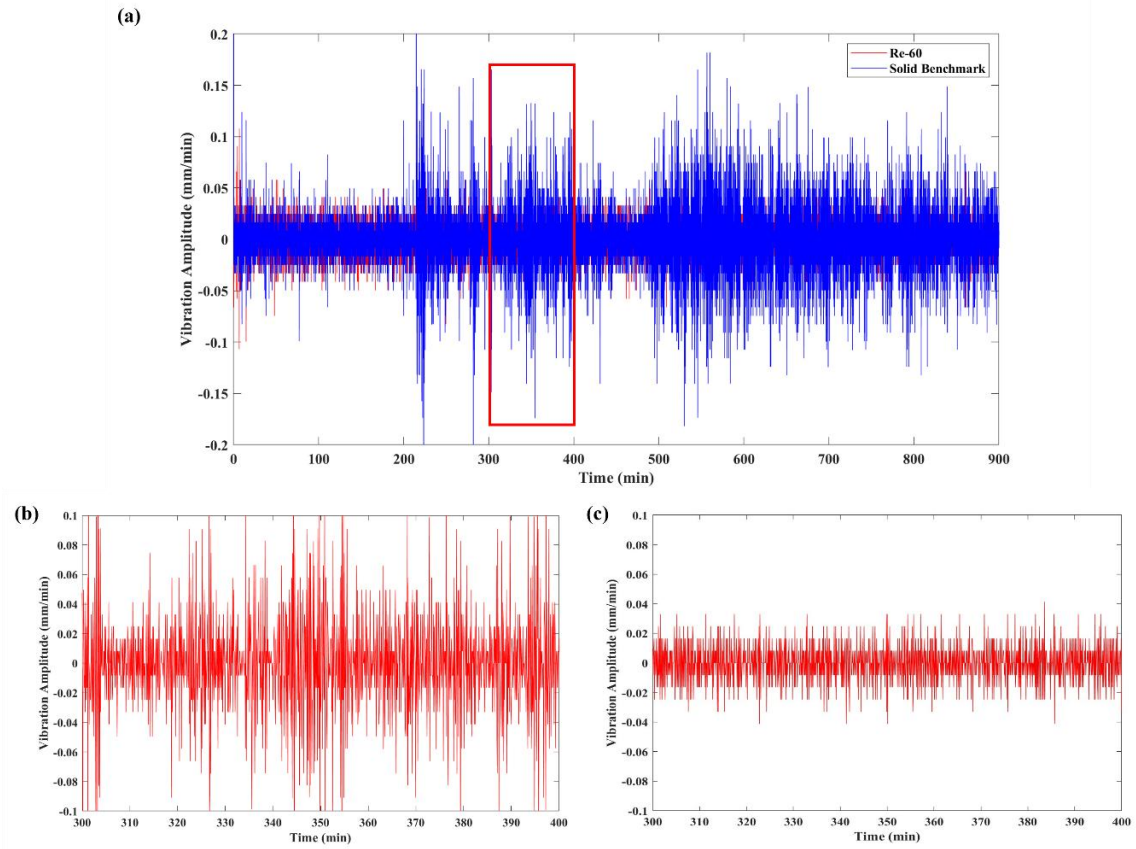

Fig 4.5 Vibration amplitude: (a) solid benchmark and re-entrant auxetic 60 degrees, (b) detailed solid benchmark, (c) detailed re-entrant auxetic 60 degrees

Table 4.1 Vibration amplitude values of re-entrant auxetic structures and the solid benchmark

Sample	Vibration Amplitude (mm/min)
Solid Benchmark	0.0291
Re-20	0.0160
Re-30	0.0149
Re-45	0.0142
Re-60	0.0123

4.3 Wear Properties - Specific Wear Rate (SWR) and Scanning Electron Microscopy (SEM) Results

4.3.1 Wear Results

Fig 4.6 compares the wear results of the specimens with and without the re-entrant structures. It is interesting to note that the wear resistance of the specimens was effectively improved with the embedded re-entrant structures. The lowest wear rate was achieved by the specimen with the most negative Poisson's Ratio in sliding direction, i.e. the re-entrant auxetic angles of 60 degrees. To further understand the underlying wear mechanisms induced by re-entrant structures, the worn surfaces are examined by using both optical and electronic microscopies which will be discussed in the following section.

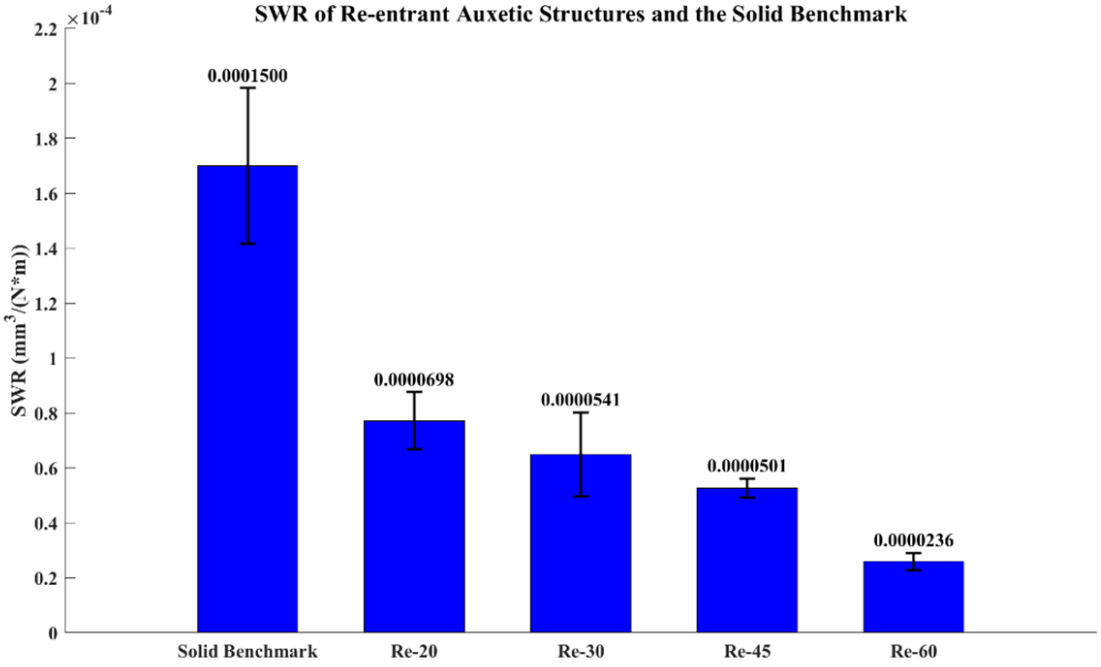

Fig 4.6 Specific wear rate of re-entrant auxetic structures and the solid benchmark

4.3.2 SEM - Wear Features and Surface Roughness

Fig 4.7 compares the SEM images of the worn surfaces of specimens with and without the embedded re-entrant structures. As shown in Fig 4.7(a) and (b), for the worn surfaces of the specimen without re-entrant structures, there are continuous grooves along the sliding direction, indicating the severe abrasive wear caused by the surface asperities on the hard steel. Also, there are numerous micro-cracks against the friction direction. As shown in Figs 4.3 and 4.5, there were severe friction oscillations and vibrations during the sliding process. In this case,

surface fatigue takes place as the production of force alternating compression-tension stresses, associated with the formation of micro-cracks on worn surfaces [202], [203], as shown in Fig 4.7(a). This may also explain the relative high wear loss of the specimens without re-entrant structures.

With the presence of re-entrant structure, the friction oscillations and induced vibration have been effectively reduced (cf. Fig 4.5). Accordingly, no observable cracks were noticed on worn surfaces (Fig 4.7 c and d), resulting in the reduction in wear rate for the specimens. Material transfer was also noticed on the worn surface (see Fig 4.7c) for the re-entrant structure, which has an angle of 20^{o}, indicating the adhesive wear process. This can be explained by the relatively higher contact temperature due to continuous contact with less vibrations in the vertical direction compared to the specimen without re-entrant structures. Thus, the polymeric wear debris can easily deform due to thermal softening effects. As a result, the polymeric wear debris is likely to form the transfer films on the metal counterpart and sometimes back-transfer to the worn surface polymer specimen, as shown in Fig 4.7(c) [204], [205].

With a further increase in the re-entrant angles (e.g. 60^{o}), the CoF decreases (Fig 4.4), leading to less frictional heating and lower contact temperature. Consequently, the governing wear mechanisms changed from adhesion to mild abrasion. As shown in Fig 4.7(d), uniform, light grooves were observed on the worn surface with much less attached back-transferred debris. Thanks to the vibration absorption with re-entrant structure, there are no noticeable surface cracks.

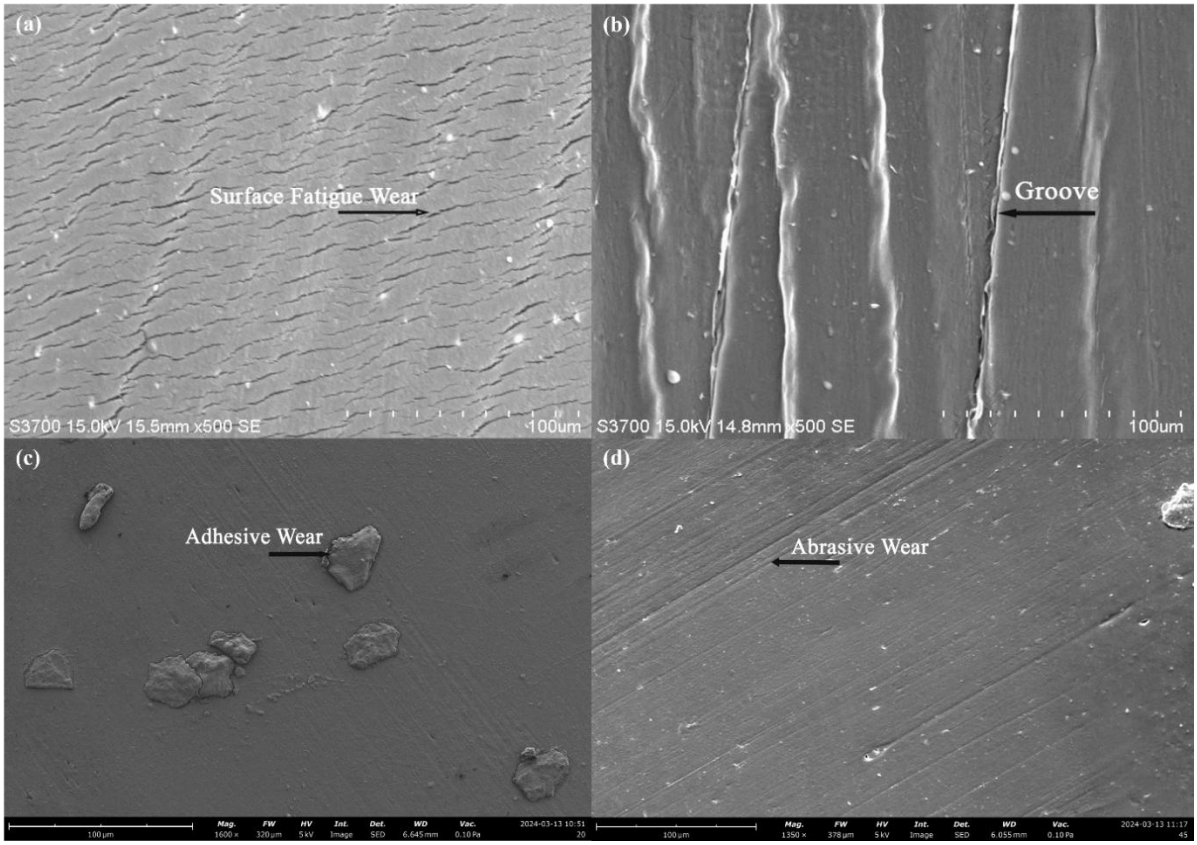

Fig 4.7 SEM of sample's contact surface: (a) (b) solid benchmark, (c) Re-20, (d) Re-60

Meanwhile, the EDS measurement was carried out as shown in Fig 4.8. The unmarked peak shown in each sample's spectrum is the element of Au which is used for the coating of SEM specimens. In general, owing to much higher surface energy of steel materials than that of polymers, the material transfer will take place dominantly from polymer to steel. Only a very small amount of steel elements can be seen on the worn surfaces polymeric specimens. In particular, the attached debris shows much higher Fe elements, suggesting it was transferred back from counterpart surface as shown in Fig 4.9. Normally, high friction force and more intensive friction-induced vibration would favor wear debris to be back transferred on polymer samples. As a result, the solid benchmark also has the higher weight concentration of transferred Fe at 2.1%. Meanwhile, the re-entrant auxetic 20 degrees and 60 degrees have the much lower weight concentration of the transferred Fe at 0.4% and 0.5%, as seen in Fig 4.8(b) and (c) respectively.

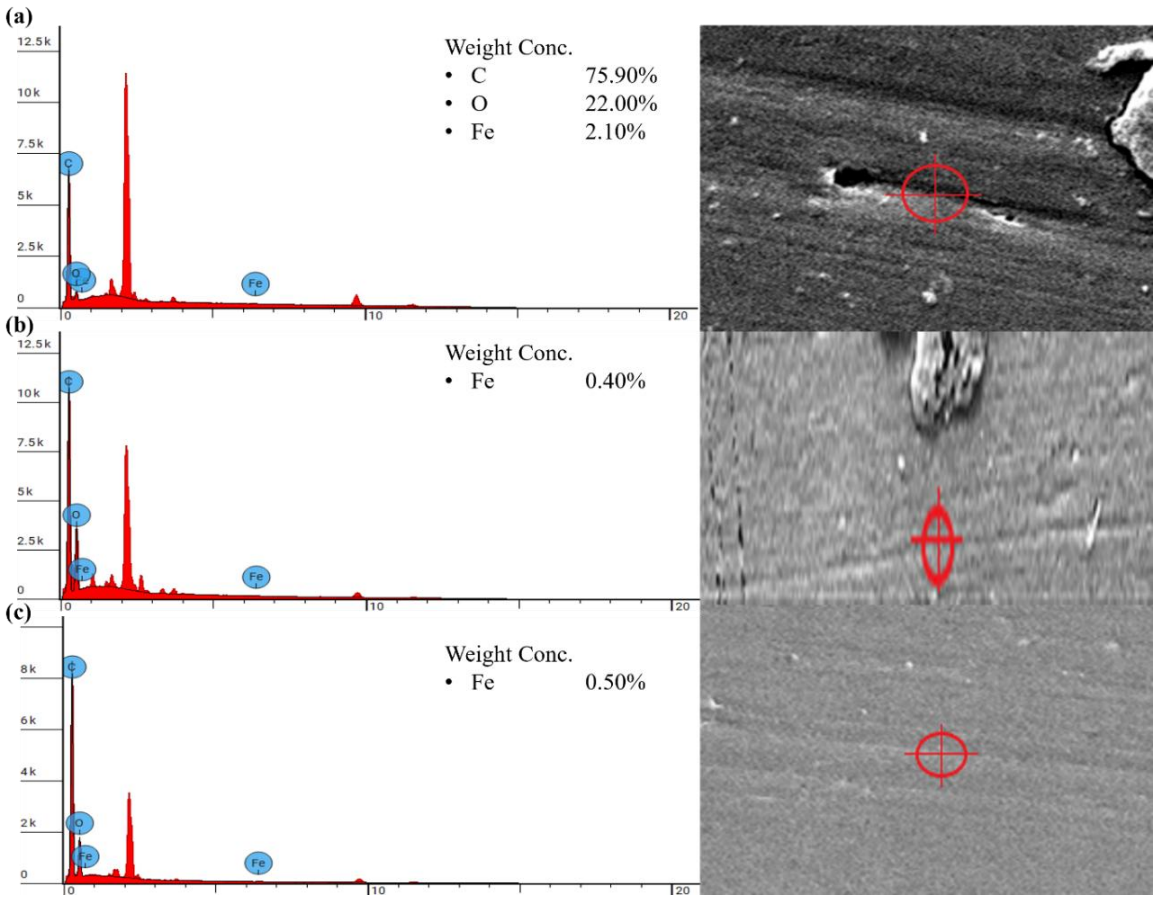

Fig 4.8 EDS result of worn surface: (a) solid benchmark, (b) re-entrant auxetic 20 degrees, (c) re-entrant auxetic 60 degrees

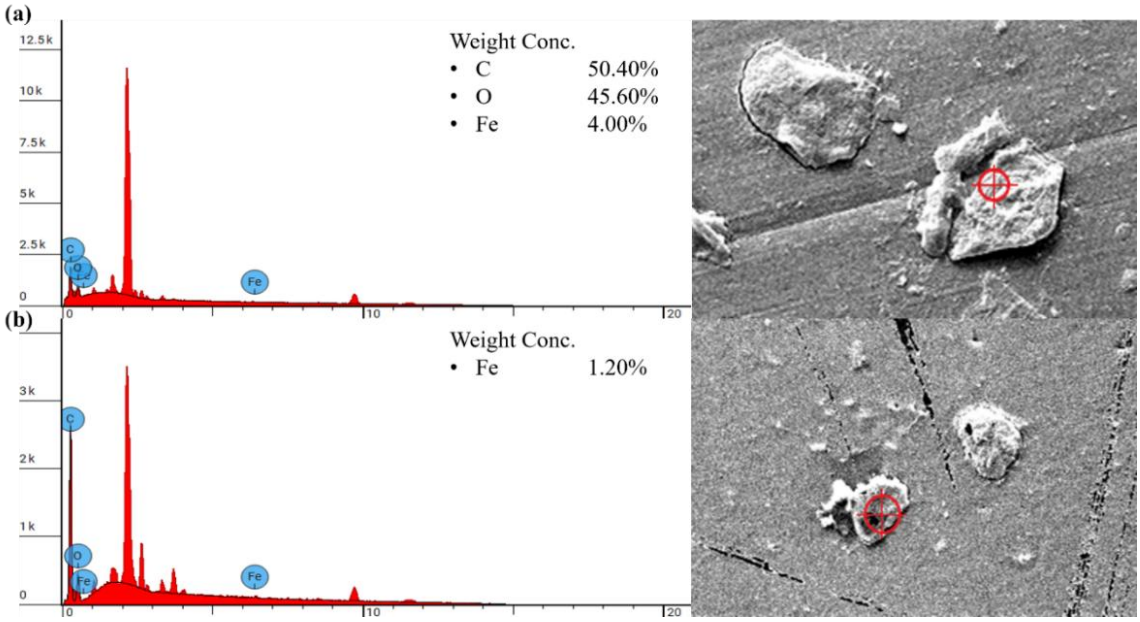

Fig 4.9 EDS result of wear debris on worn surface: (a) solid benchmark, (b) re-entrant auxetic 20 degrees

It is well known that contact temperature between sliding pairs can increase due to frictional heating which can significantly affect the wear mechanisms involved in the contact region. In general, the temperature is proportional to the frictional heating power intensity, q_f, which is defined as $q_f = \mu pv$ [W/m^{2}s]. Here, μ is friction coefficient, p is normal pressure and v is sliding velocity [206], [207]. However, it is practically difficult to measure the transient contact temperature at the contact spots. Hence, the bulk temperature of counterparts is often measured, though it would be significantly lower than the contact temperature at contact spots, namely flash temperature [208], [209], [210]. To confirm the relation between the contact temperature and friction, Fig 4.10 shows the elevated temperature of specimen, ΔT as function of frictional heating power intensity, q_f. It can be seen that the temperature of all re-entrant auxetic samples increases linearly corresponds to the increase frictional heating power intensity. It was also noticed that for the solid benchmark, the temperature increase was less severe compared with that predicted by the trendline generated from the data for re-entrant structures (cf. Fig 4.10). This can be explained by the more intense friction-induced vibrations for solid benchmark specimens which lead to less increased temperature due to the less contact time between contact spots in the real contact region during friction process.

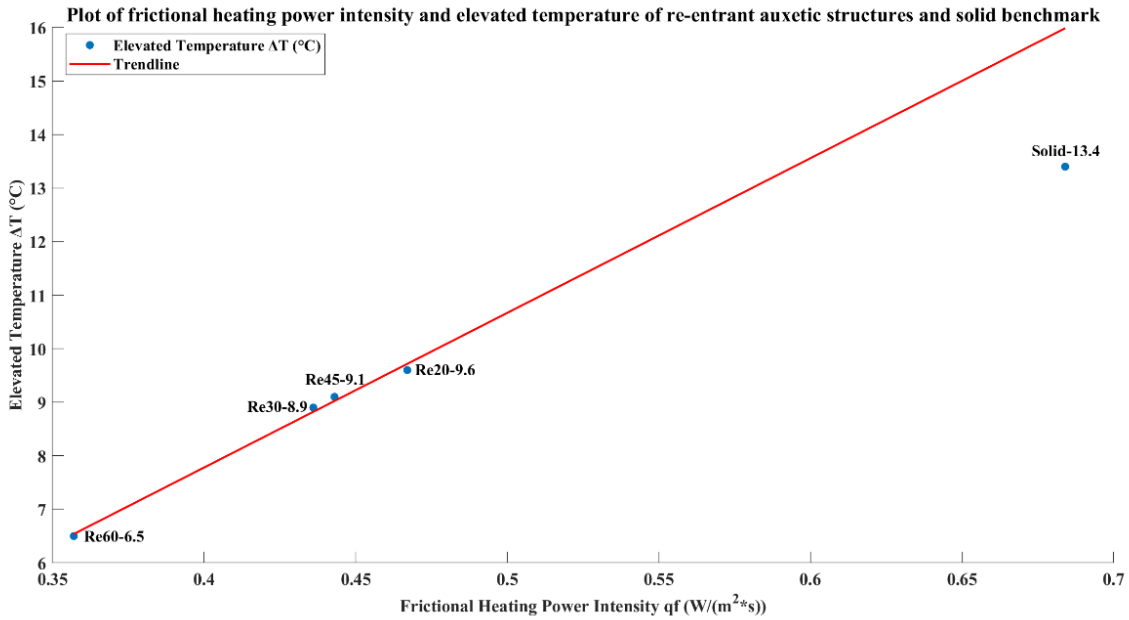

Fig 4.10 Plot of frictional heating power intensity and elevated temperature ΔT of re-entrant auxetic structures, compared with the solid benchmark specimen

As mentioned before, the real contact temperature at contact spot can be much higher than the bulk temperature of the counterparts. In general, there is a proportional relationship between

two temperatures, i.e. higher bulk temperature indicates higher contact temperatures. Further, higher frictional heating is also supported by SEM observations. As seen in Fig 4.11(a), a clear thermal softening wear feature shown in the worn surface of re-entrant auxetic 20 degrees, corresponding to the higher bulk temperature shown in Fig 4.10 above. This thermal feature disappeared in the later re-entrant degrees as seen through Fig 4.11(b) to (d). As aforementioned, with an increase in the re-entrant angles (e.g. 60°), the CoF gradually decreases, leading to less frictional heating and lower contact temperature. Consequently, the governing wear mechanisms changed from adhesion to mild abrasion which is correspondingly shown in Fig 4.11 that no clear groove observed in re-entrant auxetic 30 degrees, and the formation of groove becomes deeper and more distributed as the angle increases from 45 degrees to 60 degrees.

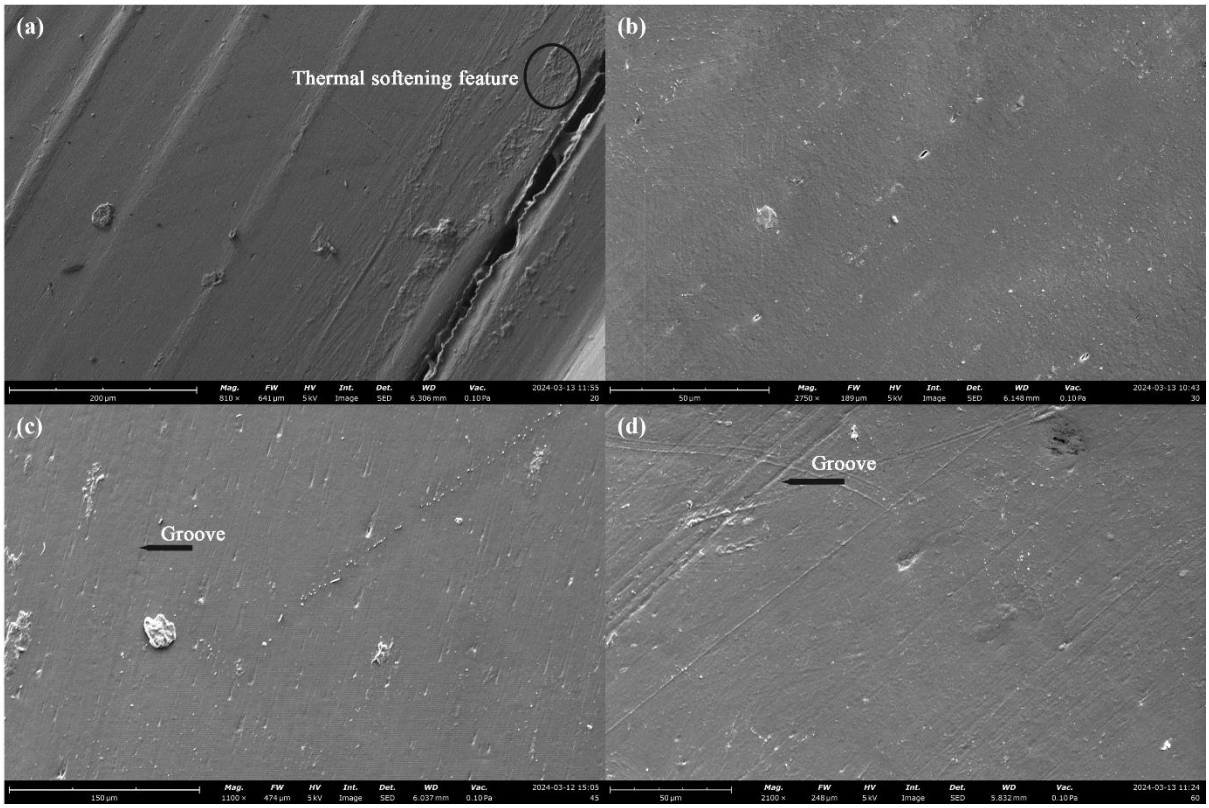

Fig 4.11 SEM of sample's contact surface: (a) Re-20, (b) Re-30, (c) Re-45, (d) Re-60

Fig 4.12 compares the surface profile images of the worn surface of different specimens. The values of the measured surface roughness, R_a were summarized in Table 4.2. As shown in the figures, the solid specimens show the more severe surface damage/deformation with the highest surface roughness. With the re-entrant auxetic structures, the surface roughness was greatly decreased without severe surface damage. With the increase re-entrant angles, the surface roughness gradually increased due to the transition from adhesion to mild abrasion wear.

However, with 20 degrees, the highest surface roughness was observed because of the large back-transferred wear debris attached to worn surfaces.

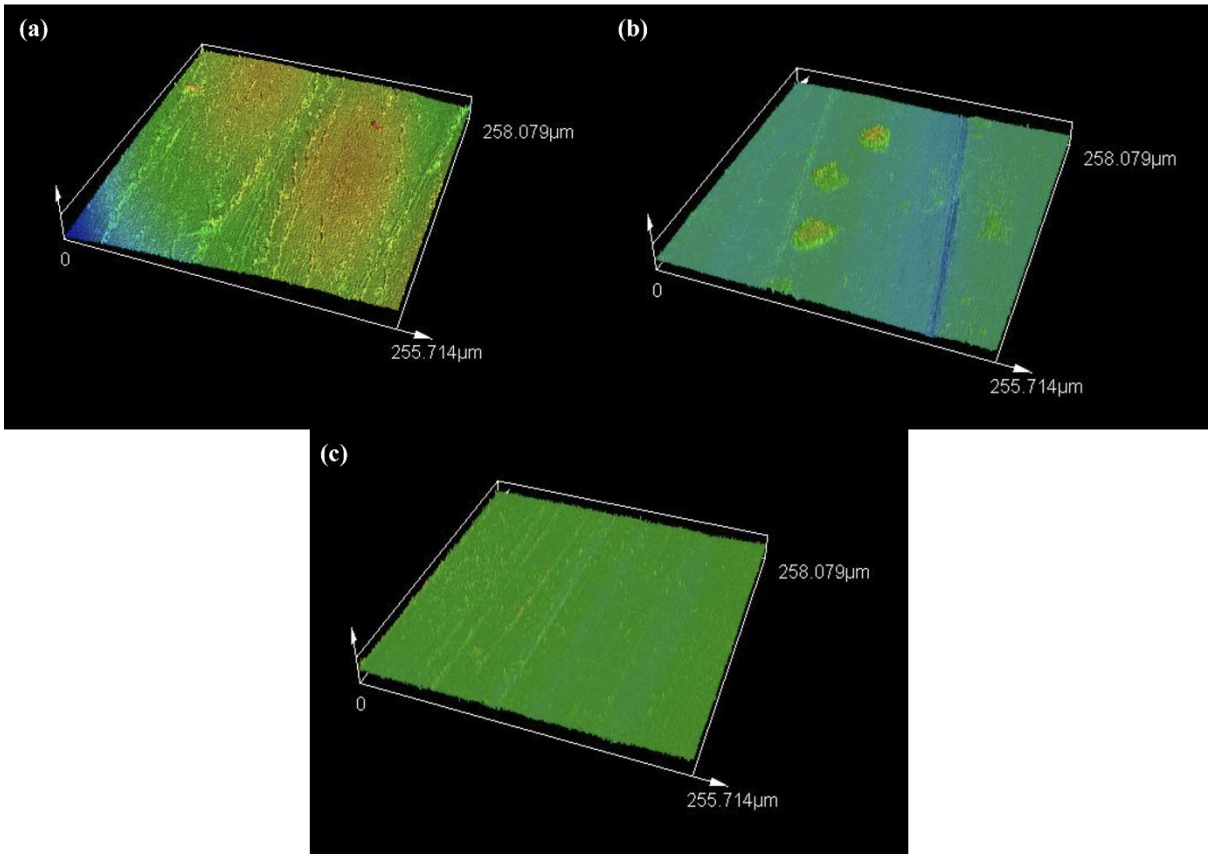

Fig 4.12 Worn surface of re-entrant auxetic structure: (a) solid benchmark, (b) Re-20, (c) Re-60

Table 4.2 Surface roughness of re-entrant auxetic structures and the solid benchmark

Samples	R_a (µm)
Solid Benchmark	0.722 ± 0.073
Re-20	0.191 ± 0.013
Re-30	0.095 ± 0.008
Re-45	0.109 ± 0.014
Re-60	0.139 ± 0.019

4.4. Heat treatment effects on friction and wear behaviour

4.4.1 Friction and wear behaviour of printed PLA

Fig 4.13 compares the typical friction responses of the printed PLA samples before and after heat treatment. All tests were conducted under an applied normal load of 5 N and a constant disk rotation speed of 120 rpm. For the untreated sample shown in Fig 4.13(a), the coefficient of friction (CoF) exhibited a slight increase during the initial stage, up to approximately 200 min. This behaviour is likely associated with an increase in the real contact area and contact

temperature resulting from frictional heating. Beyond this stage, significant fluctuations in the CoF were observed. After post-heat treatment, the solid benchmark sample showed an early and abrupt increase in CoF, with pronounced fluctuations initiating at approximately 48 min, as seen Fig 4.13(b). As sliding continued, these oscillations became dominant, and the test was terminated at 687 min when the CoF exceeded the upper threshold limit. The severe CoF fluctuations can be attributed to the increased stiffness and brittleness of PLA after post-heat treatment. This behaviour hinders the formation of a stable and uniform transfer film on the steel counterpart, thereby leading to increase CoF fluctuations during sliding [211].

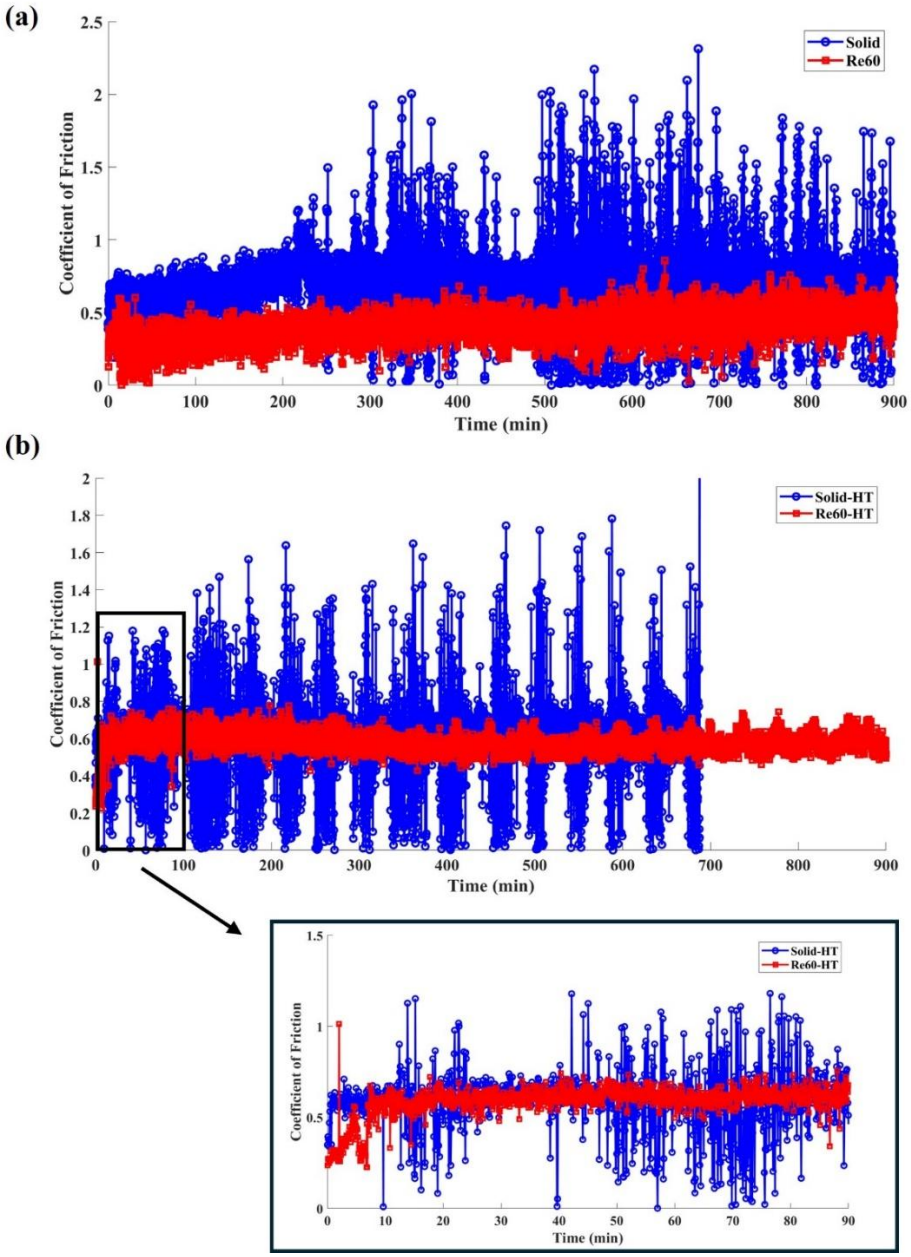

Fig 4.13 Coefficient of friction of PLA samples with (Re60) and without re-entrant (solid) structure tested under 5N: (a) before and (b) after heat treatment

The pronounced fluctuations in friction shown above are generally associated with vibrations, the FIV (friction-induced vibrations) in the sliding system [200], [201]. In this paper, the vibration amplitude was calculated in Eq.4 and Fig 2.7 using the captured the vertical displacement of sliding samples with LVDT sensor. Fig 4.14 illustrates the effects of post-heat treatment on the FIV behaviour of the printed materials. It is evident that samples with embedded re-entrant structures, both heat-treated and untreated, exhibited significantly reduced FIV compared with the solid benchmark sample. To quantitatively evaluate the vibration absorption performance and assess the effect of post-heat treatment on FIV, the relative absorbed vibration percentage (AVP) with respect to the solid benchmark sample was calculated based on Equation (5) above.

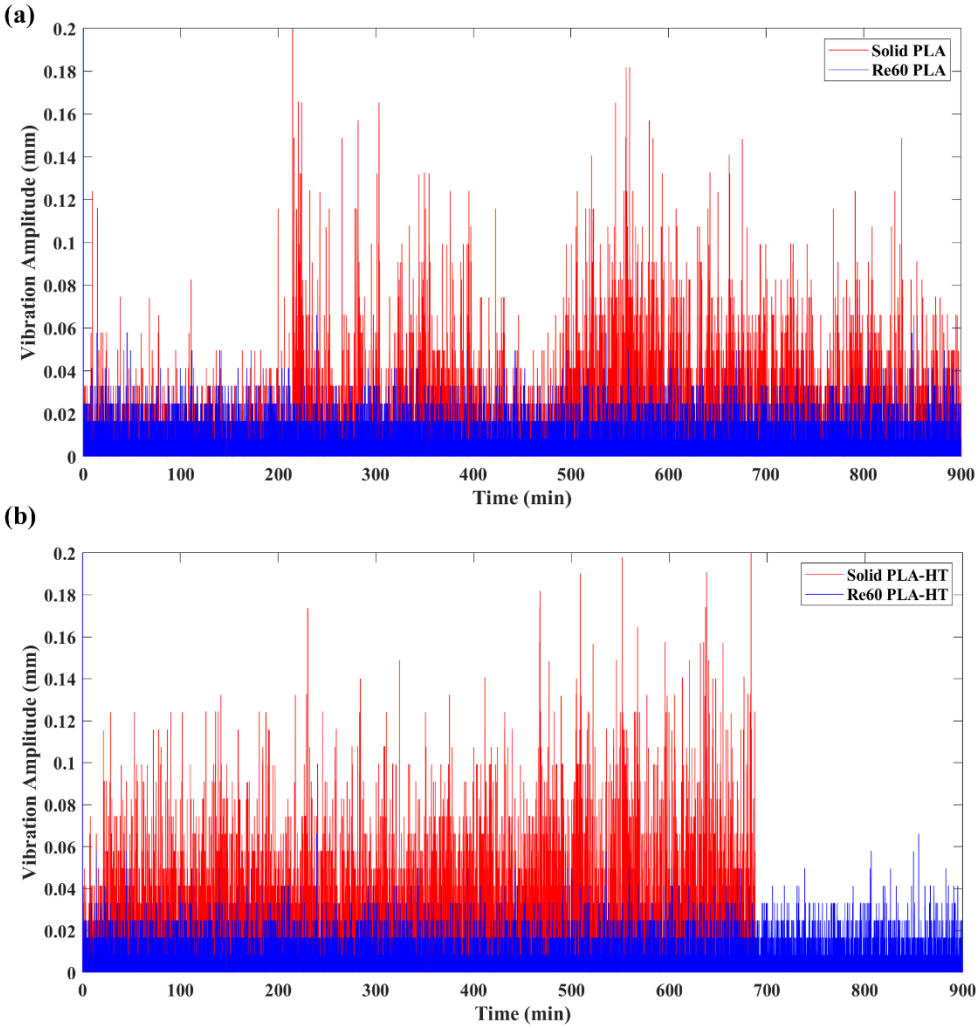

Fig 4.14 Vibration amplitude of PLA samples with (Re60) and without re-entrant (solid) structure tested under 5N: (a) before and (b) after heat treatment.

Fig 4.15 presents the AVP results for both PLA and heat-treated PLA (PLA-HT). It can be seen that FIV was effectively mitigated by the embedded re-entrant auxetic structures due to their inherent vibration absorption capabilities [159], [160]. Furthermore, the heat-treated re-entrant wear model exhibited a more pronounced vibration absorption capacity, reaching 65.30%. While post-heat treatment enhances the mechanical performance of PLA, the associated increase in the degree of crystallinity partially transforms the amorphous regions into crystalline lamellae, leading to higher stiffness and increased structural rigidity [212]. This improvement in stiffness enhances the energy absorption capability of the re-entrant structures [179], [213], thereby contributing to the observed reduction in FIV [109].

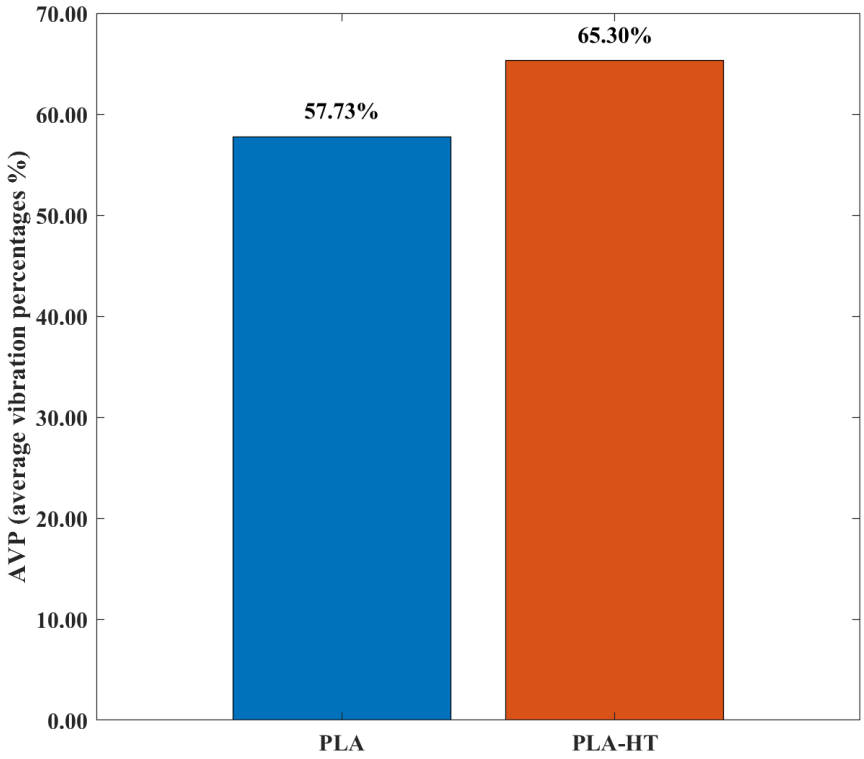

Fig 4.15 AVP of PLA samples with the re-entrant structures before (PLA) and after heat-treated PLA (PLA-HT).

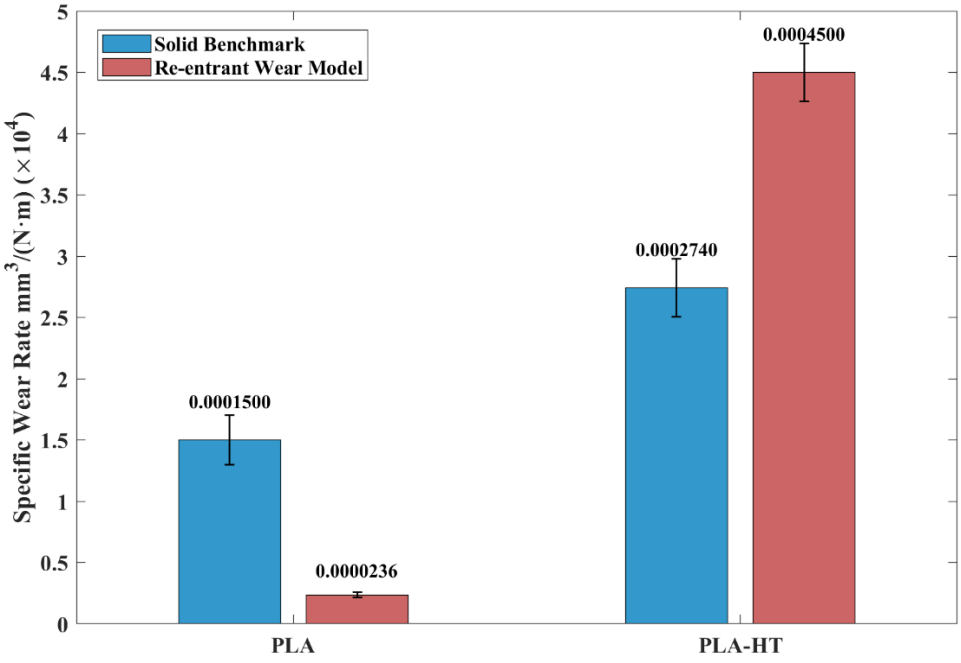

Fig 4.16 The effects of post-heat treatment on printed PLA samples before and after heat-treatment tested under 5N

Fig 4.16 summarizes the specific wear rate (SWR) of the printed PLA samples. For all heat-treated wear specimens, the SWR generally increased. Notably, for samples with embedded re-entrant structures, the SWR increased significantly after the heat treatment, from 0.0000236 $mm^3/(N \cdot m)$ to 0.0004500 $mm^3/(N \cdot m)$. This substantial increase in wear is also evidenced by the markedly greater amount of wear debris distributed around the steel counterpart after testing, as shown in Fig 4.17.

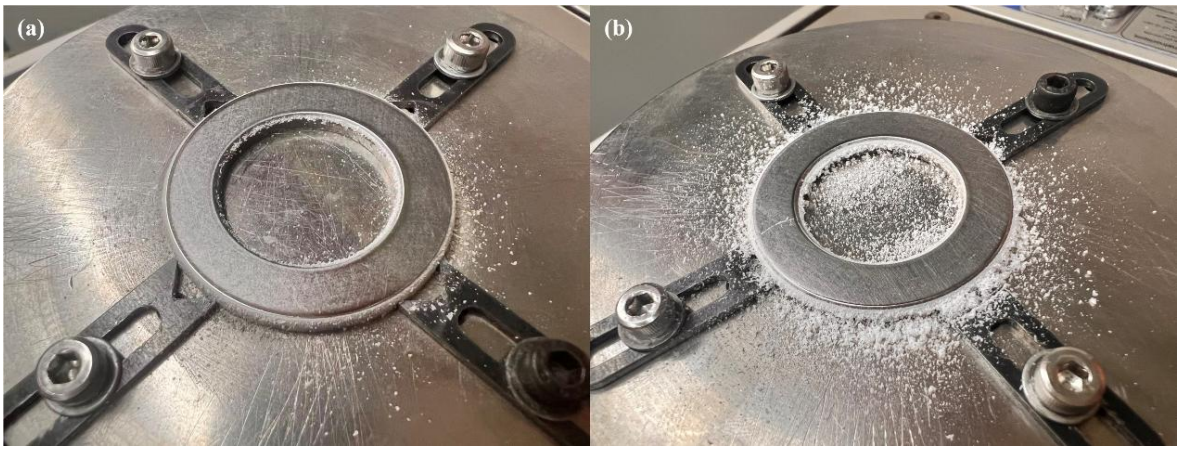

Fig 4.17 Smearing wear debris on the disk after the test of the heat-treated sample printed in PLA: (a) solid-benchmark, (b) re-entrant wear model

4.4.2 Friction and wear behaviour of printed PEEK

Fig 4.18 compares the typical friction responses of the printed PEEK wear model with and without post-heat treatment. All tests were carried out under the applied load of 25N in a total testing time of 600 min. As seen in Fig 4.18(a), the CoF slightly increased during the running-in stage, which lasted approximately 200 min. This behaviour is similar to that observed for PLA. Owing to the excellent mechanical properties and high wear resistance of PEEK, the untreated solid benchmark sample did not exhibit significant oscillations as those observed for PLA during the later stages of sliding. After post-heat treatment, the running-in stage was shortened to approximately 50 min, as shown in Fig 4.18(b). This behaviour is likely due to the increased degree of crystallinity [214] and ductility of the material, which promotes faster formation of a stable transfer film [215]. Improved surface integrity and reduced interfacial shear consequently enhance the stability of the CoF. Moreover, samples with embedded re-entrant structures exhibited reduced CoF under both heat-treated and untreated conditions.

Fig 4.19 presents the vibration amplitude of the PEEK wear models before and after heat treatment. Owing to the superior mechanical properties of PEEK, the solid benchmark sample exhibited relatively low FIV, with a vibration amplitude of 0.00136 mm. In contrast, the sample with embedded re-entrant auxetic structures further suppressed FIV, reducing the amplitude to 0.00109 mm. This behaviour is consistent with the results observed for heat-treated PLA, as discussed above, and aligns with the conclusions reported in our previous study [109].

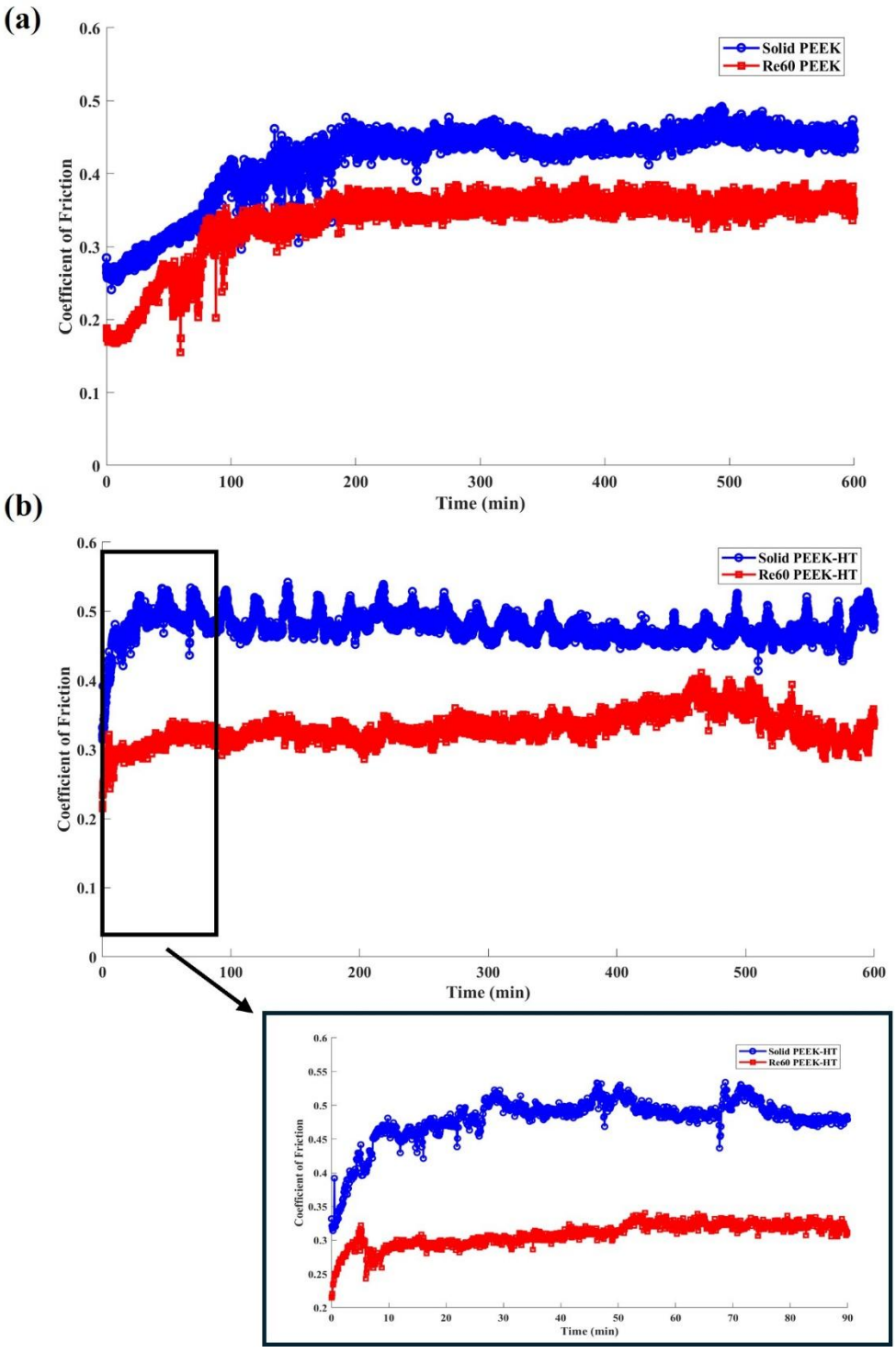

Fig 4.18 Coefficient of friction of PEEK samples with (Re60) and without re-entrant (solid) structure tested under 25N: (a) before and (b) after heat treatment

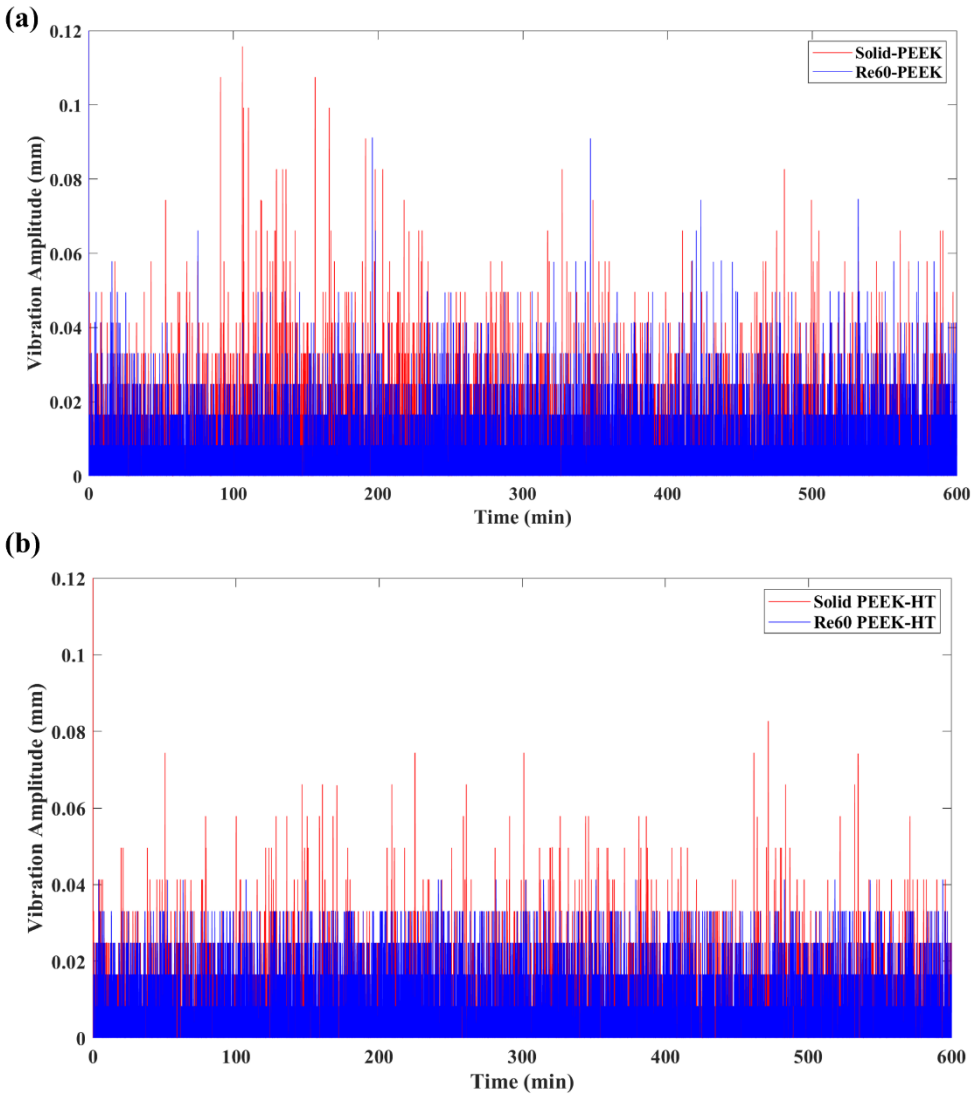

Fig 4.19 Vibration amplitude of PEEK samples with (Re60) and without re-entrant (solid) structure tested under 25N: (a) before and (b) after heat treatment

The post-heat treatment had the detrimental effect on the PLA wear sample shown in Fig 4.16, but the PEEK sample exhibited the opposite trend. As seen in Fig 4.20, the SWR of heat-treated wear models generally decreases. Notably, the re-entrant wear model exhibited a greater reduction from 0.00000318 $mm^3/(N \cdot m)$ to 0.00000062 $mm^3/(N \cdot m)$. To further understand the underlying wear mechanism of this opposite SWR result in PLA and PEEK induced by the post-heat treatment, the worn surfaces were further examined by SEM and EDS and discussed in the following section.

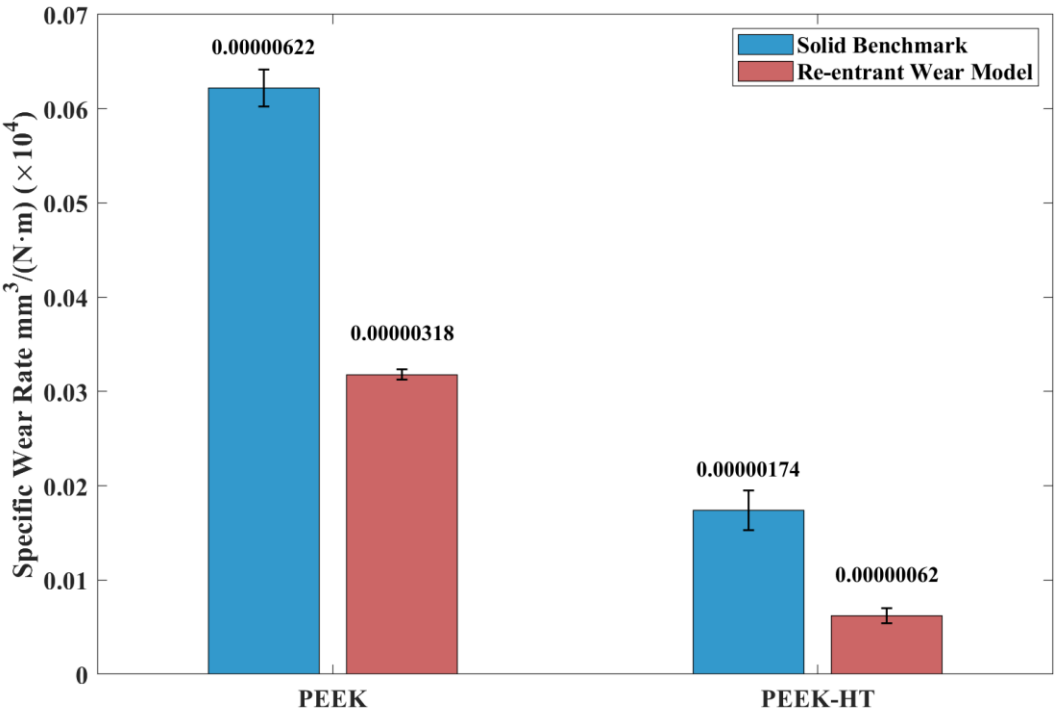

Fig 4.20 The effects of post-heat treatment on printed PEEK samples before and after heat-treatment tested under 25N

4.5 Discussions

Fig 4.21 presents the SEM images of the worn surfaces of printed PLA before and after post-heat treatment. As seen in Fig 4.21(a), numerous micro-cracks are observed on the worn surface of PLA sample without re-entrant structures. As indicated in Fig 4.13(a) and 4.14(a), severe friction oscillations and vibrations occurred during the sliding process of the sample. The conditions likely resulted in surface fatigue due to alternating compressive and tensile stresses, which consequently promoted the formation of micro-cracks on the worn surface [202], [203]. With the embedded re-entrant structure, however, both friction oscillations and FIV were effectively mitigated (cf. Fig 4.13(a)). As a result, no observable cracks were detected on the worn surface, as shown in Fig 4.21(c). Instead, grooves aligned along the sliding direction were visible, indicating a mild abrasive wear process. Consequently, the wear rate was significantly reduced, as demonstrated in Fig 4.16.

After the post-heat treatment, the increased brittleness of the material promoted the formation of powder-shaped debris during the wear process, as shown in Fig 4.17. For the solid specimen, severe FIV occurred, as illustrated in Fig 4.13(b). In this case, the intensive FIV in the vertical

direction repeatedly impacted the loosened wear debris, resulting in compacted debris on the worn surface, as shown in Fig 4.21(b). The compacted debris may have acted as a cushion, reducing surface cracks on the worn surface. With the embedded re-entrant structures, FIV was effectively reduced. Consequently, larger-sized particulate wear debris were observed on the worn surface, as shown in Fig 4.21(d). These larger debris particles likely acted as a three-body abrasion medium, contributing to increased wear loss of the sample. As a result, the highest wear loss was observed for the sample with the embedded re-entrant structures.

The SEM and EDS analyses were performed on the steel counterpart sliding against the heat-treated PLA samples. The results indicate that no effective transfer film was formed on the steel counterpart, which explains the high wear loss observed in the heat-treated samples. The elemental composition of the small, isolated dark regions on the steel counterpart showed an increase in carbon content, confirming the presence of polymeric debris. The carbon content in these regions increased to 19.40 wt.% compared to the mostly bare steel, which had a carbon content of 1.90 wt.%, as shown in Fig 4.22. For the heat-treated PLA sample with the re-entrant structure, the EDS results revealed a similar trend in carbon content on the steel counterpart. The darker regions containing polymer debris exhibited an increase in carbon content to 16.70 wt.% compared to the bare steel-dominated regions, which had a carbon content of 1.80 wt.%, as shown in Fig 4.23.

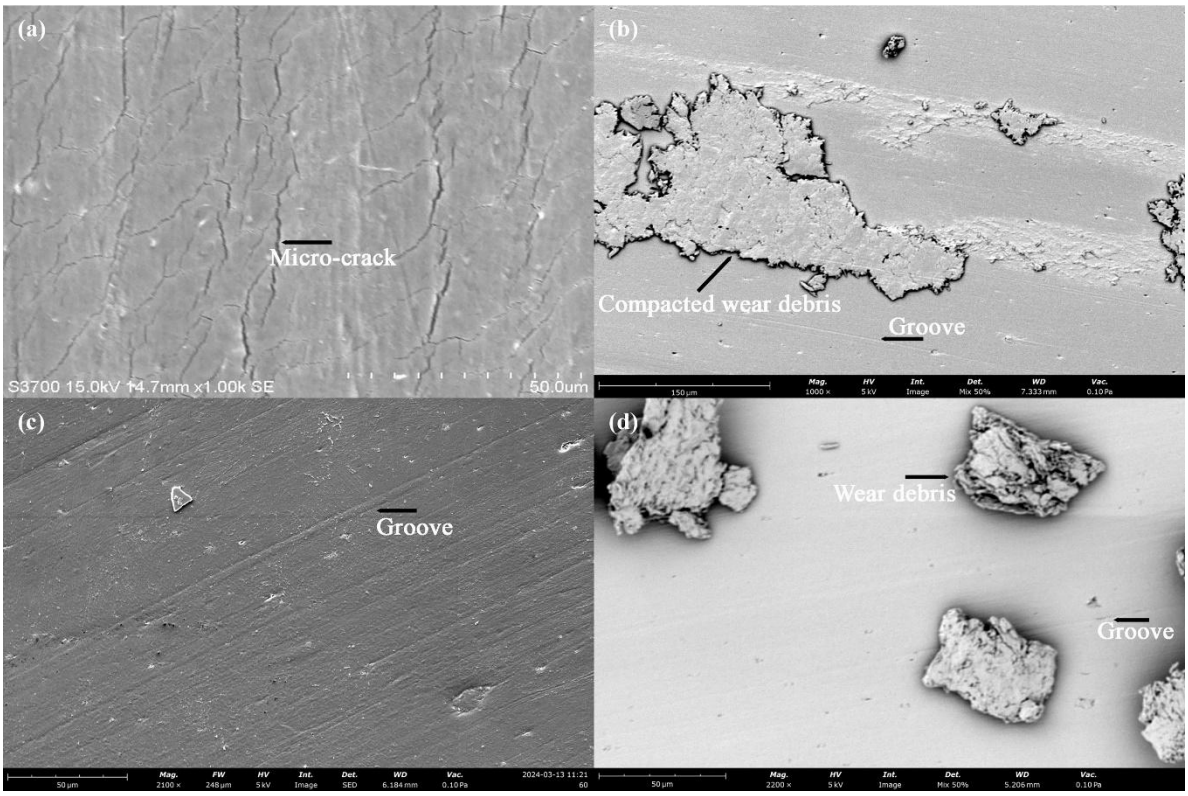

Fig 4.21 SEM images of the worn surfaces of the PLA sample tested at 5 N: (a) solid benchmark sample before heat treatment, (b) solid benchmark sample after heat treatment, (c) with a re-entrant structure before heat treatment, and (d) with a re-entrant structure after heat treatment.

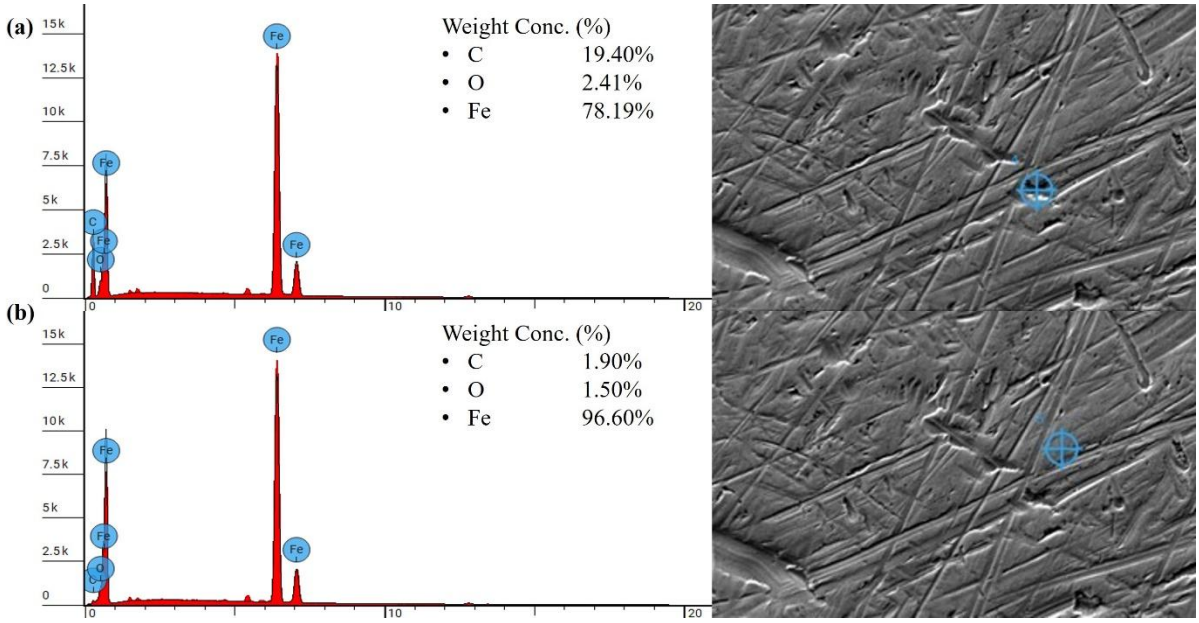

Fig 4.22 EDS result of the steel counterpart tested against the heat-treated PLA solid benchmark sample tested under 5 N: (a) isolated dark regions, (b) mostly bare steel regions

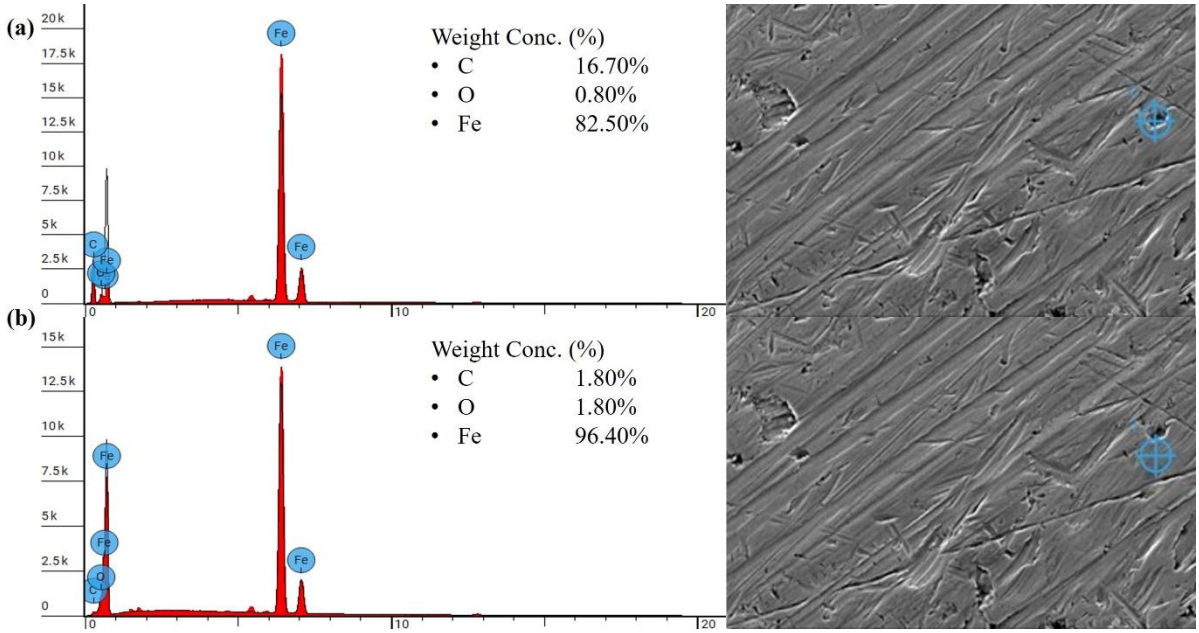

Fig 4.23 EDS result of the steel counterpart tested against the heat-treated PLA sample with a re-entrant structure under 5 N: (a) isolated dark regions, (b) mostly bare steel regions

For PEEK material, owing to its favourable mechanical property profile, all PEEK samples exhibited reduced CoF fluctuations and FIV. The worn surface condition of the solid benchmark was smoother, displaying uniform grooves along the sliding direction, as shown in Fig 4.24(a). This indicates a mild abrasion wear mechanism. With the incorporation of the embedded re-entrant structure, the CoF further decreased with even lower FIV, and the worn surface became smoother as seen in Fig 4.24(b). This improvement was accompanied by a reduction in SWR shown in Fig 4.20 above.

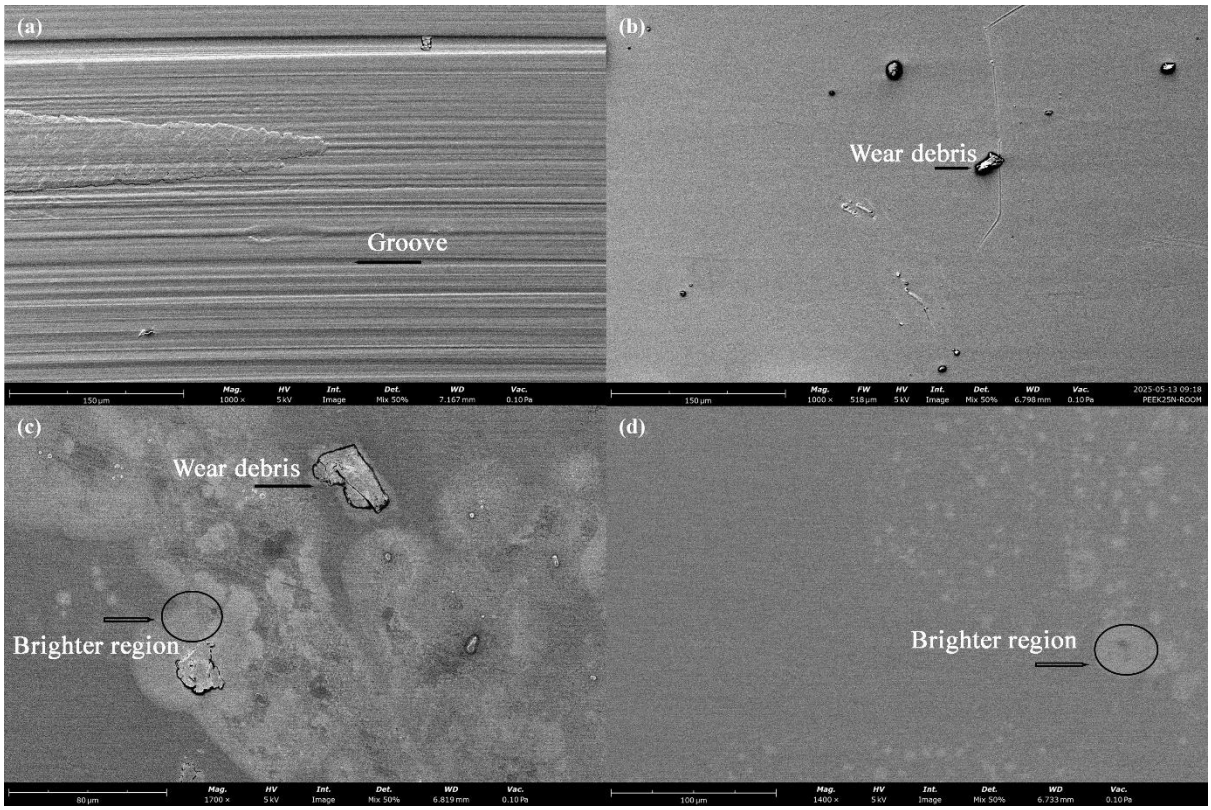

Fig 4.24 SEM images of the worn surfaces of the PEEK sample tested at 25 N: (a) solid benchmark sample before heat treatment, (b) with a re-entrant structure before heat treatment, (c) solid benchmark sample after heat treatment, and (d) with a re-entrant structure after heat treatment.

After heat treatment, the strength and ductility of the material further improved, resulting in a smoother worn surface, as shown in Fig 4.24(c) and Fig 4.24(d). In general, with increased ductility, the polymer tends to undergo plastic deformation rather than brittle fracture, which typically facilitates the formation of a stable protective transfer film [216]. SEM and EDS analyses confirmed that a greater number of patched transfer film layers were observed on the steel counterpart. As shown in Fig 4.25, the dark regions exhibited significantly higher carbon

content, reaching up to 38.65 wt.%, along with a notable reduction in Fe content to 54.72%, compared to the steel-dominated regions with the Fe content of 96.40 wt.%. The higher carbon content of the polymer patches on the steel, nearly twice that of PLA, indicates the formation of a comparatively thicker and more effective transfer film. Notably, unlike the extensive distribution of wear debris observed on the heat-treated re-entrant wear model printed in PLA (Fig 4.21(d)), no grooves or wear debris were detected on the worn surface of the re-entrant wear model made of PEEK after heat treatment, as shown in Fig 4.24(d). This is likely due to the increased both strength and ductility. The higher carbon content of up to 40.16 wt.% observed in the darker regions from the EDS analysis demonstrated in Fig 4.26 suggests the formation of an effective transfer film compared to the heat-treated solid benchmark. Furthermore, both heat-treated wear samples displayed slightly brighter regions occupying a notable portion of the scanned area, as seen in Fig 4.24(c) and Fig 4.24(d). These regions correspond to dense lamellar structures with a high load-bearing capacity [217]. As a result, the heat-treated sample with embedded re-entrant structures exhibited the highest wear resistance.

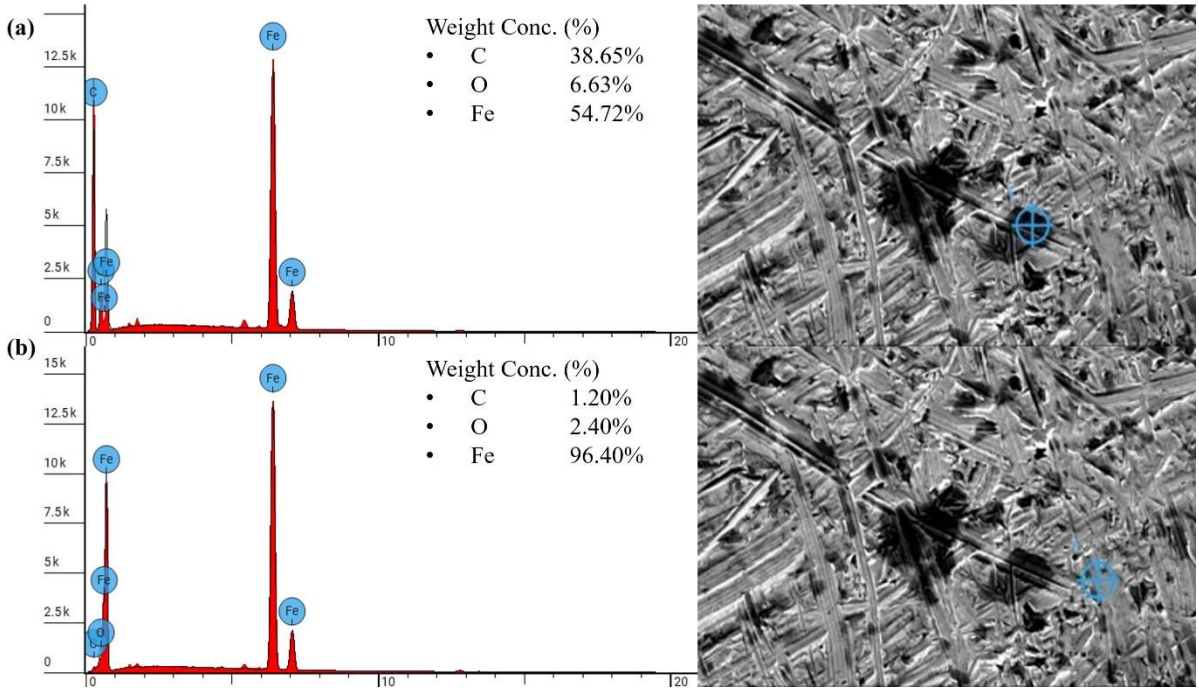

Fig 4.25 EDS result of the steel counterpart against the heat-treated PEEK solid benchmark sample tested under 25 N: (a) dark regions, (b) steel-dominated regions

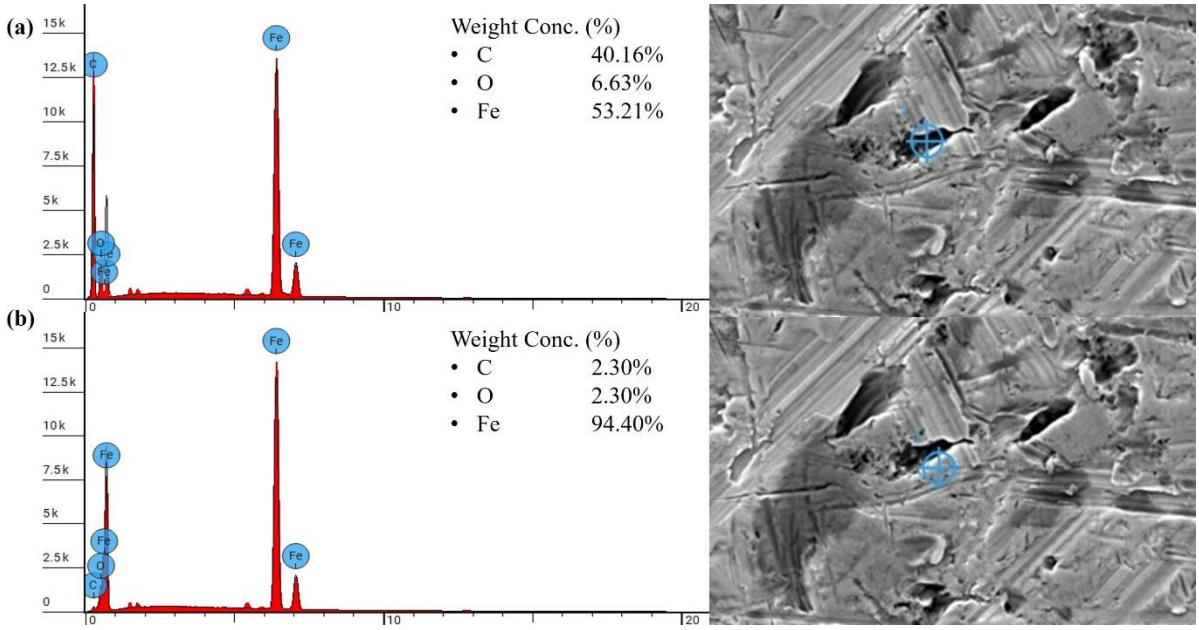

Fig 4.26 EDS result of the steel counterpart tested against the heat-treated PEEK sample with a re-entrant structure tested under 25 N: (a) dark regions, (b) steel-dominated regions

4.6 Conclusions

In this Chapter, a series of specimens with the embedded re-entrant auxetic structures were prepared by using 3D printing technology. The effects of post-heat treatment on the tribological properties of PLA and PEEK materials and structures fabricated using FDM technology. In particular, the tribological performance of printed specimens with and without embedded re-entrant auxetic structures was comparatively evaluated. The following conclusions can be drawn:

(1) During the sliding process, the friction-induced vibration can be effectively suppressed with the embedded re-entrant structure thanks to its exceptional energy absorption behaviour. Further, the effect is more noticeable with the re-entrant structures having higher auxetic angles i.e. a more negative value of NPR in the horizontal direction.

(2) Having the re-entrant structure leads to a more stable CoF pattern with a lower average CoF value. Further, the wear loss of the specimen reduced by avoiding severe fatigue wear. It is also noted that changing the re-entrant auxetic structure angles from 20 degrees to 60 degrees, the dominance wear mechanism shows the transition from adhesive wear to mild abrasion due to the reduction in frictional heating.

(3) Under all testing conditions, the embedded re-entrant auxetic structures contributed to a lower coefficient of friction (CoF) and reduced friction-induced vibration (FIV) owing to their high energy absorption capacity. The results indicate that post-heat treatment can deteriorate the CoF behavior of solid benchmark PLA specimens, as evidenced by the earlier onset and increased intensity of CoF fluctuations. In contrast, specimens incorporating re-entrant auxetic structures exhibited a comparatively more stable CoF after heat treatment. Furthermore, the enhanced stiffness of the embedded re-entrant structures resulting from post-heat treatment led to a more pronounced mitigation of FIV in the printed specimens.

(4) Post-heat treatment exhibited contrasting effects on the specific wear rate (SWR) of the two printed materials. For PLA, the treatment increased material brittleness, leading to a higher SWR. Specifically, after post-heat treatment, the SWR of the solid benchmark PLA increased from 1.5×10^{-4} $mm^3/(N\cdot m)$ to 2.74×10^{-4} $mm^3/(N\cdot m)$. For specimens incorporating re-entrant structures, the wear rate was generally reduced compared with solid ones, due to the mitigation of friction-induced vibrations (FIV). Nevertheless, post-heat treatment also resulted in an increase in SWR of PLA samples with the re-entrant structure from 2.36×10^{-5} $mm^3/(N\cdot m)$ to 4.5×10^{-4} $mm^3/(N\cdot m)$. This behavior is attributed to the increased brittleness of heat-treated PLA, which promoted the formation of powder-like wear debris and, consequently, higher wear loss despite the improved strength. In contrast, for PEEK, post-heat treatment enhanced both strength and ductility, leading to a significant improvement in wear resistance. Specifically, the SWR of the solid benchmark PEEK decreased from 6.2×10^{-6} $mm^3/(N\cdot m)$ to 1.74×10^{-6} $mm^3/(N\cdot m)$ after heat treatment. Similarly, the re-entrant structured specimens exhibited a reduction in SWR from 3.18×10^{-6} $mm^3/(N\cdot m)$ to 6.2×10^{-7} $mm^3/(N\cdot m)$.

Finally, it is worth noting that this chapter focuses on the distinctive effects of post-heat treatment on the tribological properties of different polymers, namely PLA and PEEK. The annealing process was selected as a commonly used and cost-efficient post-processing technique for 3D-printed parts. Nevertheless, as summarized in the literature review, other post-treatment methods, such as chemical smoothing [122] and the ironing process [123], are also available. Future work will be carried out to further explore additional effective treatment methods to achieve improved tribological properties under different sliding conditions. In particular, the combination of multiple treatment methods may allow further

tailoring and optimization of the property profiles of 3D-printed polymer components for different engineering applications.

Chapter 5 Reducing Friction-induced Vibration and Wear of Carbon Fiber Reinforced PLA Composites with the Re-entrant Auxetic Structure using 3D Printing Technology

Q1 Journal Tribology International. Current Status: Submission

In the previous chapters, the effect of post-heat treatment on the tribological performance of the FDM-printed PLA and PEEK structures has been systematically investigated. It can be seen that the heat-treatment influenced the wear behaviour of the printed structure in a much more complex way, displaying a contrasting effect of the specific wear rate of PLA and PEEK.

Meanwhile, as discussed in Chapter 1 Introduction, despite the rapid development of the additive manufacturing and the corresponding demonstrated application of CFRPs, the research on the design of additive manufactured CFRPs, especially with respect to the structural design for enhancing wear resistance in tribological applications remains limited [12], [13]. Therefore, further studies need to be conducted to systematically investigate the wear behaviour of the AM-fabricated CFRPs involved with the complex structural design.

In this Chapter, re-entrant auxetic structures were employed to reduce friction-induced vibration (FIV) and thus the wear loss of carbon fiber reinforced PLA (CF-PLA) composites against metal counterparts. Both numerical and experimental studies showed that with the increase in re-entrant angles, the negative Poisson ratio of the re-entrant structures becomes greater, leading to more pronounced effects on vibration insulation. As a result, with the embedded entrant structures, the friction-induced vibration and noise of polymer-metal sliding pairs could be effectively migrated, associated with the reduction in wear loss of polymeric specimen. For instance, the specific wear rate of CF-PLA having the auxetic structure with the re-entrant angle of 60^{o} was 1.75×10^{-5} $mm^3/N*m$, which almost an order magnitude lower than that of the specimen without the re-entrant structure. Microscopy analysis revealed that severe damage of fibres was greatly prevented with the re-entrant structures, thanks to their energy absorption and vibration insulation capacities. This led to the gradual removal process of fibres even under high loading conditions, contributing to the enhanced loading-carry capacity of the composite.

5.1 Finite Element Analysis of Re-entrant Structures

5.1.1 Design of Re-entrant Structures

Re-entrant structures were first designed in SolidWorks (SolidWorks Corp., USA). The structures with different negative Poisson's ratio was achieved by varying re-entrant angles without changing other key geometry parameters. In particular, as shown in Fig 5.1, each lattice structure consisted of a 2 × 3 array of unit cells with varying re-entrant angles of 20°, 30°, 45°, and 60°. The CAD models were subsequently imported into Abaqus/Standard (ABAQUS Inc., Providence, RI, USA) for finite element analysis (FEA). Within Abaqus, the models were discretised using a structured meshing strategy to ensure adequate resolution of the re-entrant features while maintaining computational efficiency. A mesh convergence study was performed, resulting in an average of 320,202 elements and approximately 1,561,422 degrees of freedom per model. The top cylindrical surface was kinematically constrained, and a displacement-controlled load of 1 mm (upward) was applied to the bottom surface. Fig 5.1(b) shows the stress/strain distribution within the re-entrant structure under compression loads. With the strain of information, Poisson's ratios of the structures along x- direction can be determined as -0.324, -0.544, -0.808 and -1.341, for the re-entrant angles of 20°, 30°, 45° and 60° respectively.

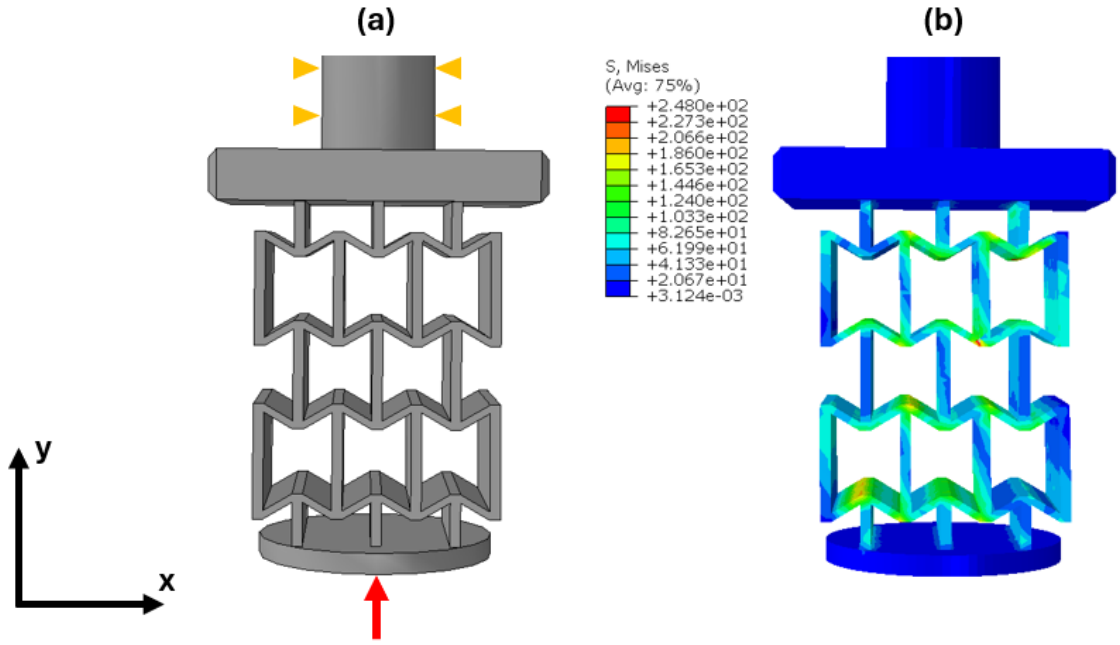

Fig 5.1 FEA test setup: (a) compressive load along y-direction, (b) the resultant stress/strain distribution of re-entrant auxetic structure.

5.1.2 Energy Absorption of Re-entrant Structures

To evaluate the structure's energy absorption capacity, energy absorption (EA) is defined as the integral of force with respect to displacement in equation below:

$$EA = \int_0^{\delta_{max}} Fd(\delta) \tag{7}$$

where F is the reaction force of the structure, δ is the applied vertical displacement, δ_{max} is the peak displacement.

Two materials considered and simulated in later discussion of peak stress and energy absorption was: polylactic acid (PLA) and carbon fiber (CF)-reinforced PLA. The material properties, obtained from our previous studies and works of literature shown in Chapter 2.1 [109], [181], were defined by Young's modulus (E, GPa) and Poisson's ratio (v) as follows: for PLA, 1.973 and 0.35; for CF-reinforced PLA, 3.946 and 0.35. As shown in Fig 5.2, PLA exhibited a moderate increase from 20° to 30°, after which the values remained relatively stable between 30° and 60°. By contrast, CF-PLA structures consistently absorbed more energy, increasing from roughly 13 mJ at 20° to about 23 mJ at 60°. Notably, with the improved mechanical properties, CF-PLA showed much higher energy absorption capacity than that of neat PLA. Further, energy absorption in CF-PLA increased more linearly with re-entrant angle compared to PLA. The results also agree with the conclusion drawn by Pan et al. [159] i.e. more negative Poisson's ratio provides better vibration isolation ability.

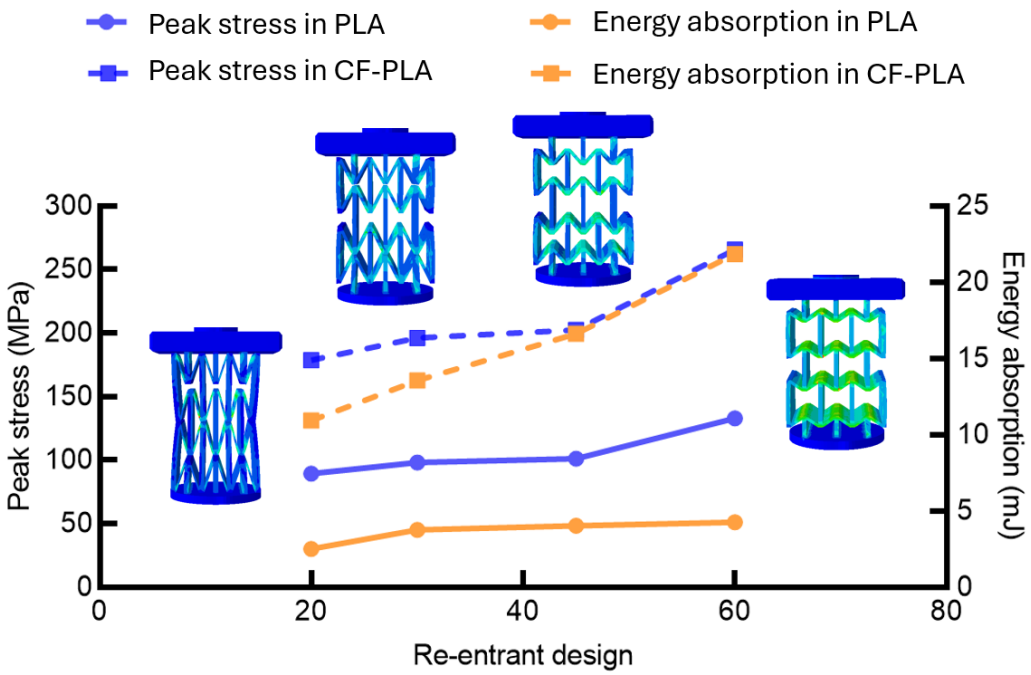

Fig 5.2 Peak von Mises (VM) stress (left Y axis) and Energy absorption (right Y axis) for re-entrant structures with various re-entrant angles, including 20°, 30°, 45°, and 60°

Under the same applied compression displacement (1mm), the peak stresses re-entrant lattice structures with different re-entrant angles (20°, 30°, 45°, and 60°) for both PLA and CF-reinforced PLA materials were also compared in the figure. Representative von Mises stress distributions for each design are also presented. While the stress pattens varied with changes in geometry due to different re-entrant angles, no significant differences were observed under the effect the carbon fibre composites compared to neat polymers. As shown in Fig 5.2, the peak stresses in both PLA and CF-PLA increased from 20° to 60°. Therefore, although a larger re-entrant angle enhances energy absorption, it also subjects the auxetic structure to higher stress concentrations particularly at nodes or joints, increasing the likelihood of premature failure.

5.2 Friction and Wear Results

5.2.1 Reducing FIV with the Re-entrant Structures

Fig 5.3 compares the typical friction responses of printed polymeric specimens with (cf. Figure 2.1b) and without (cf. Figure 2.1c) induced re-entrant structures. All tests were carried out under a normal load of 5 N for neat PLA and CF-PLA. The coefficient of friction (CoF) was observed to increase slightly during the initial sliding stage (up to ~200 minutes), likely due to the enlargement of the real contact area caused by wear of surface asperities. Beyond this stage, the specimen without a re-entrant structure exhibited significant fluctuations in CoF. Notably, the CF-PLA solid benchmark showed a sudden increase in CoF at approximately 34 minutes, accompanied by continuous, intense FIV and severe noise, as illustrated in the inset of Fig 5.3(b). As sliding progressed, these oscillations became dominant and ultimately exceeded the stabilized CoF threshold, resulting in premature test termination after only 37 minutes. This phenomenon is likely attributable to the increased structural stiffness introduced by carbon fiber reinforcement, which elevates the natural frequency of the transfer path and, in turn, amplifies vibration and noise [218]. In contrast, the specimen with a 60° auxetic angle maintained a relatively stable friction profile. Most importantly, the severe friction-induced vibrations and associated unbearable noise observed in the solid benchmark were completely eliminated.

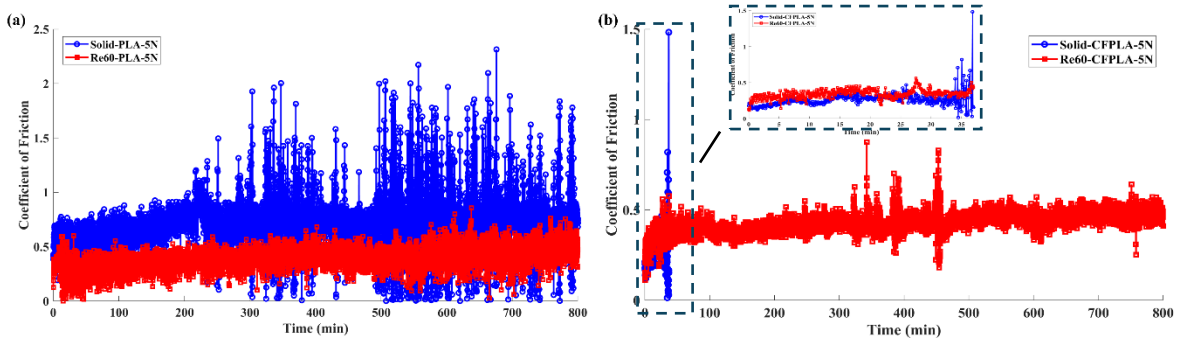

Fig 5.3 Coefficient of friction of solid benchmark and re-entrant auxetic 60 degrees: (a) in neat PLA at 5N, (b) in CF-PLA at 5N

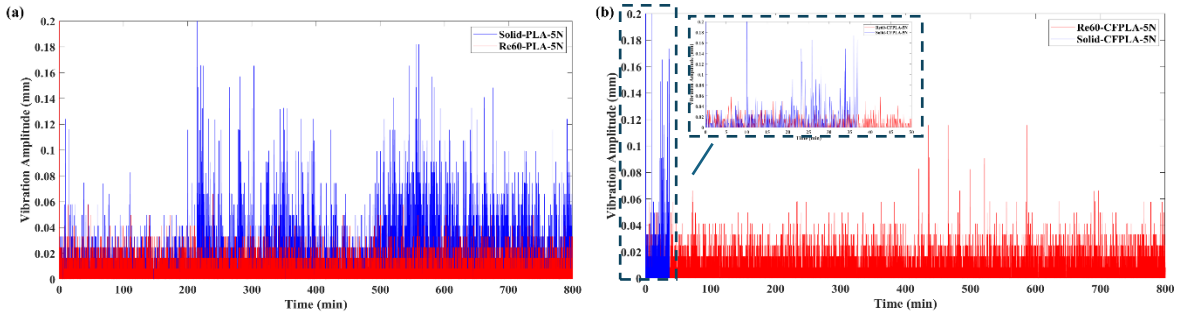

Fig 5.4 Vibration amplitude of solid benchmark and re-entrant auxetic 60 degrees: (a) in neat PLA-5N, (b) in CF-PLA at 5N

The pronounced fluctuations in friction, evident in Fig 5.3, are commonly associated with vibrations, i.e., FIV in the sliding system [200], [201]. In this study, vibration amplitude was quantified by measuring the vertical displacement of sliding samples, as described in Eq. (4) and Fig 2.7. Accordingly, Fig 5.4 compares the vibration behaviour of specimens with and without re-entrant structures. It is clear that the incorporation of re-entrant geometry could significantly suppress FIV.

Fig 5.5 presents the AVP values for both neat PLA and CF-PLA as a function of re-entrant angle. It can be seen that the incorporation of re-entrant auxetic structures reduced FIV by approximately 45 – 62%, confirming that about half of the vibration was effectively mitigated due to the vibration absorption capability of these structures [159], [160]. Moreover, AVP increased with the larger re-entrant angle of 60°, and CF-PLA exhibited a more pronounced absorption capacity compared with neat PLA. These findings are consistent with the simulation results (see Fig 5.2), which indicate that FIV is more effectively suppressed using re-entrant structures with higher auxetic angles—corresponding to more negative Poisson's ratios in stiffer materials such as CF-PLA.

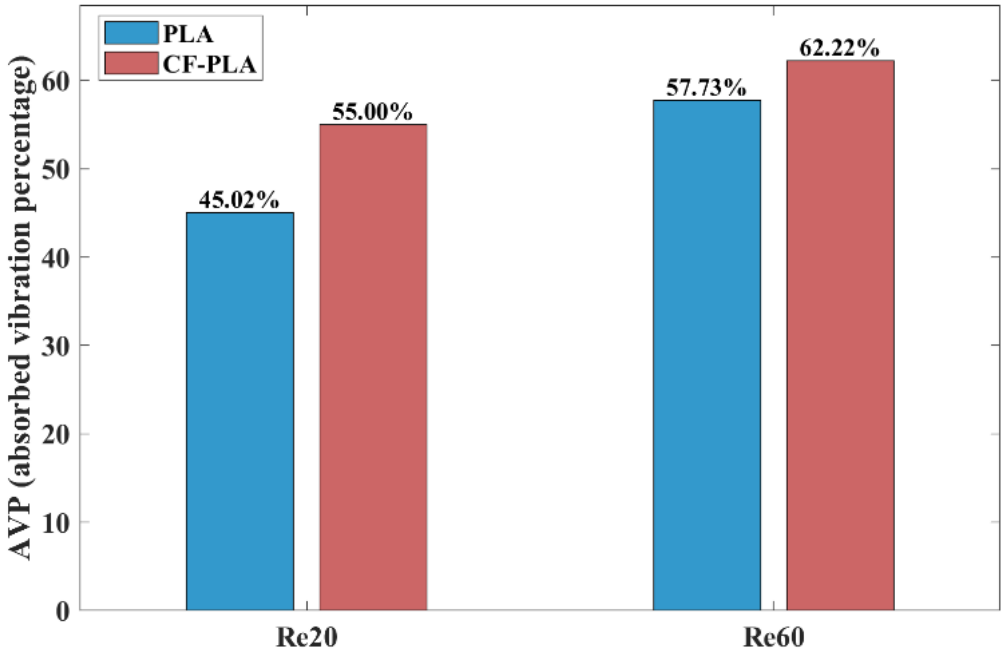

Fig 5.5 AVP of re-entrant auxetic structures in PLA and CF-PLA at 5 N

5.2.2 Enhancement Effects of Re-entrant Structures on the Wear Behaviour of CF-PLA

Fig 5.6 illustrates the effects of re-entrant structures on friction and wear performance of polymeric specimens tested under 5 N. The CoF was determined by the average value during the steady stage. It is evident that the lower friction was achieved with the re-entrant structure, compared that obtained with solid one. Further, the CoF tends to decrease with the auxetic angles. Correspondingly, the wear resistance of the specimens was also effectively improved with the embedded re-entrant structures. The lowest wear rate was achieved by the CF-PLA with the large auxetic angles of 60^{o}. However, it is important to note that the large deformation required for energy absorption through auxeticity also subjects the structure to higher stress concentrations, particularly at nodes or joints, thereby increasing the risk of premature failure. In fact, with the further increase of load up to 10 N, premature failure in a re-entrant structure made of neat PLA took place, as shown in Fig 5.7(a).

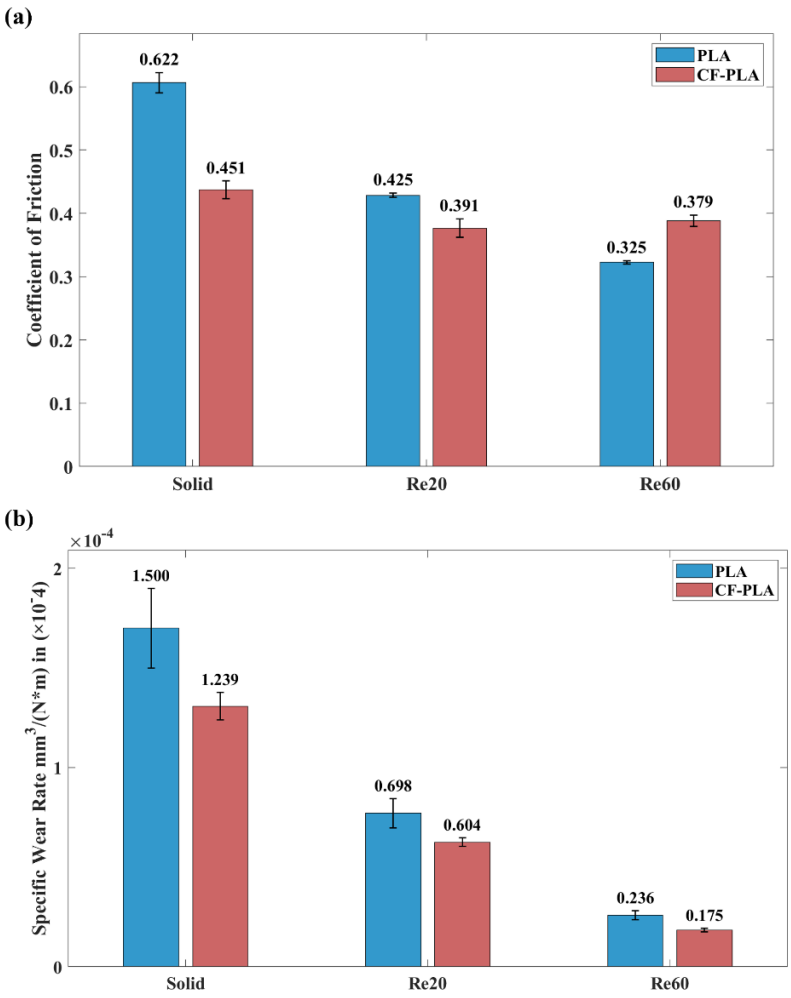

Fig 5.6 The effects of re-entrant structures on (a) CoF and (b) SWR of neat PLA and CF-PLA at 5N

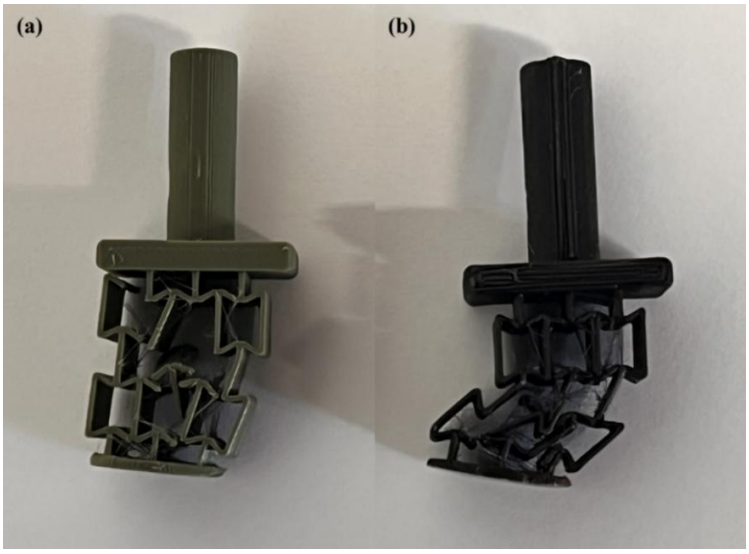

Fig 5.7 Premature failure in re-entrant structure for neat (a) PLA under 10 N and (b) CF-PLA under 25 N

With the incorporation of CF fillers, the load-bearing capacity of CF-PLA was greatly enhanced, allowing the structure to perform under significantly higher loading conditions. Fig 5.8 summarizes the friction and wear behaviour across loads ranging from 10 to 20 N. It is clear that VA is generally decreased with the increase re-entrant angles. Correspondingly, the friction coefficient and wear rate decrease within each own applied normal loads. Nevertheless, with further increases in load to 25N, the re-entrant structure with a 60° angle failed first (cf. Figure 5.7b), owing to the higher stress concentration effects shown in Fig 5.2. Therefore, although larger re-entrant angles improve energy absorption capacity, they compromise load-bearing capacity. Hence, selecting an appropriate re-entrant angle is critical and should be guided by the specific design requirements of different tribological applications.

To further understand the underlying wear mechanisms induced by re-entrant structures, the worn surfaces are examined by using both optical and electronic microscopies which will be discussed in the following section.

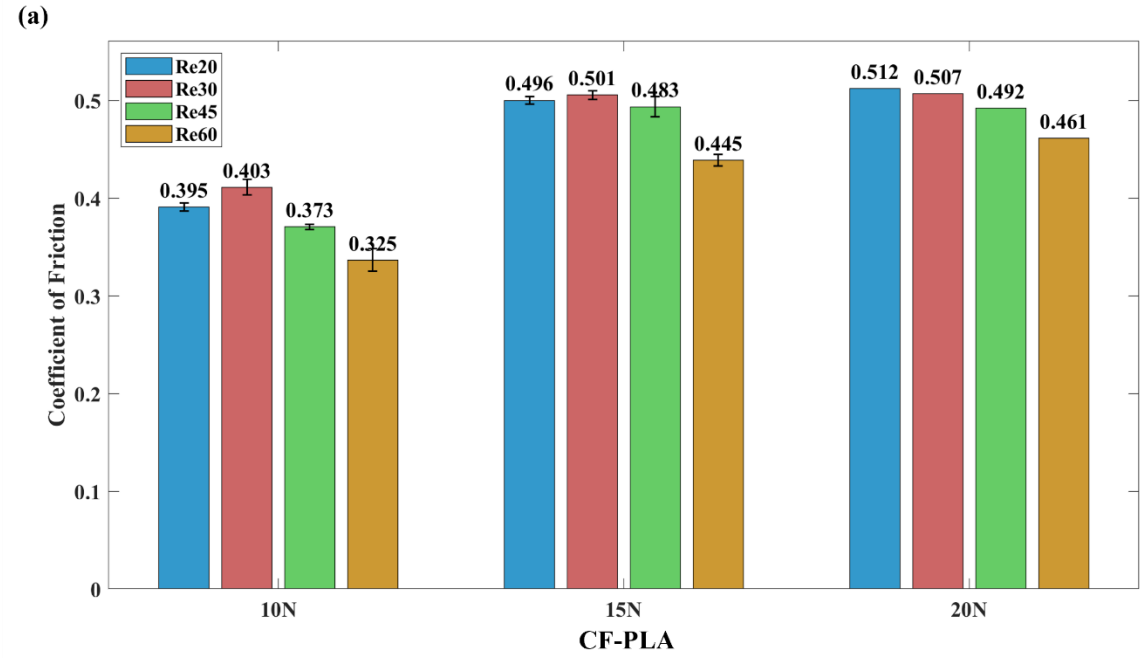

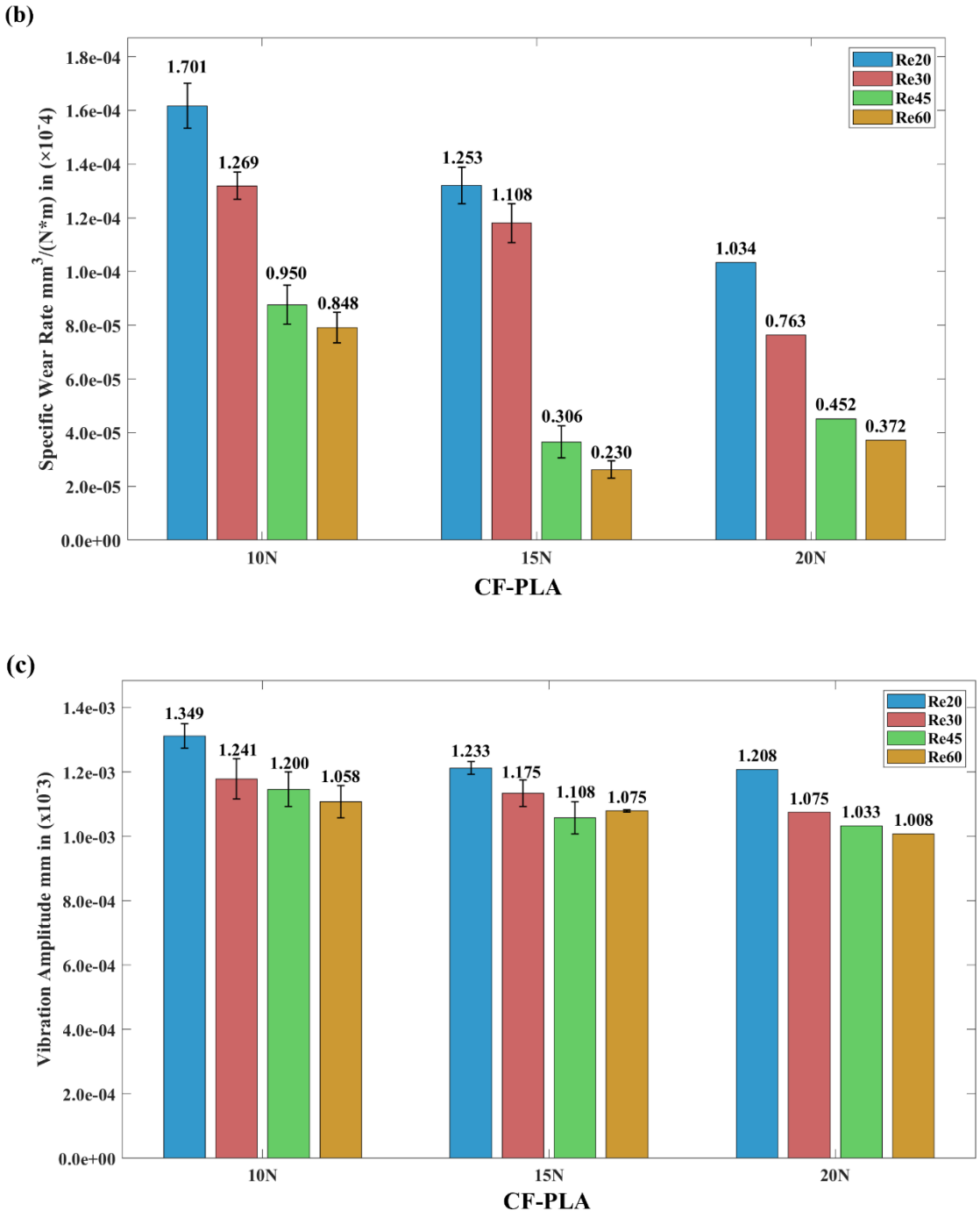

Fig 5.8 Effects of Re-entrant angles under different loads on the (a) CoF, (b) SWR, and (c) VA

5.3 Wear Modelling of CF-PLA with Re-entrant Structures

Fig 5.9 presents SEM images comparing the worn surfaces of CF-PLA specimens with and without embedded REAS structures under loads of 5 N and 10 N. As shown in Fig 5.9(a) and 5.9(c), the samples without re-entrant structures exhibited more severe fibre breakage,

primarily due to the intense oscillating impact forces. Additionally, a greater amount of wear debris was observed, especially at the higher load. As a result, serious fiber removal happened at higher loading conditions, leaving large grooves on the worn surfaces. In contrast, the specimens embedded with REAS showed milder abrasive wear, characterized by continuous grooves and significantly smoother worn surfaces. Severe fibre breakage was effectively mitigated, with fibre thinning emerging as the dominant wear feature—suggesting a more gradual fibre removal process. It is well established that the wear performance of fibre-reinforced polymers is largely governed by the manner in which fibres are removed from the composite matrix [219]. During wear, the fibres bear the majority of the load. Therefore, to maximize the reinforcing effect of short fibres, it is crucial that they are removed gradually rather than fractured abruptly. Thus, the re-entrant structure's ability to absorb energy played a key role in reducing fibre impact vibrations (FIV), thereby minimizing cyclic impact damage. This is likely a major contributing factor to the lower wear rate observed in CF-PLA specimens containing the re-entrant structures.

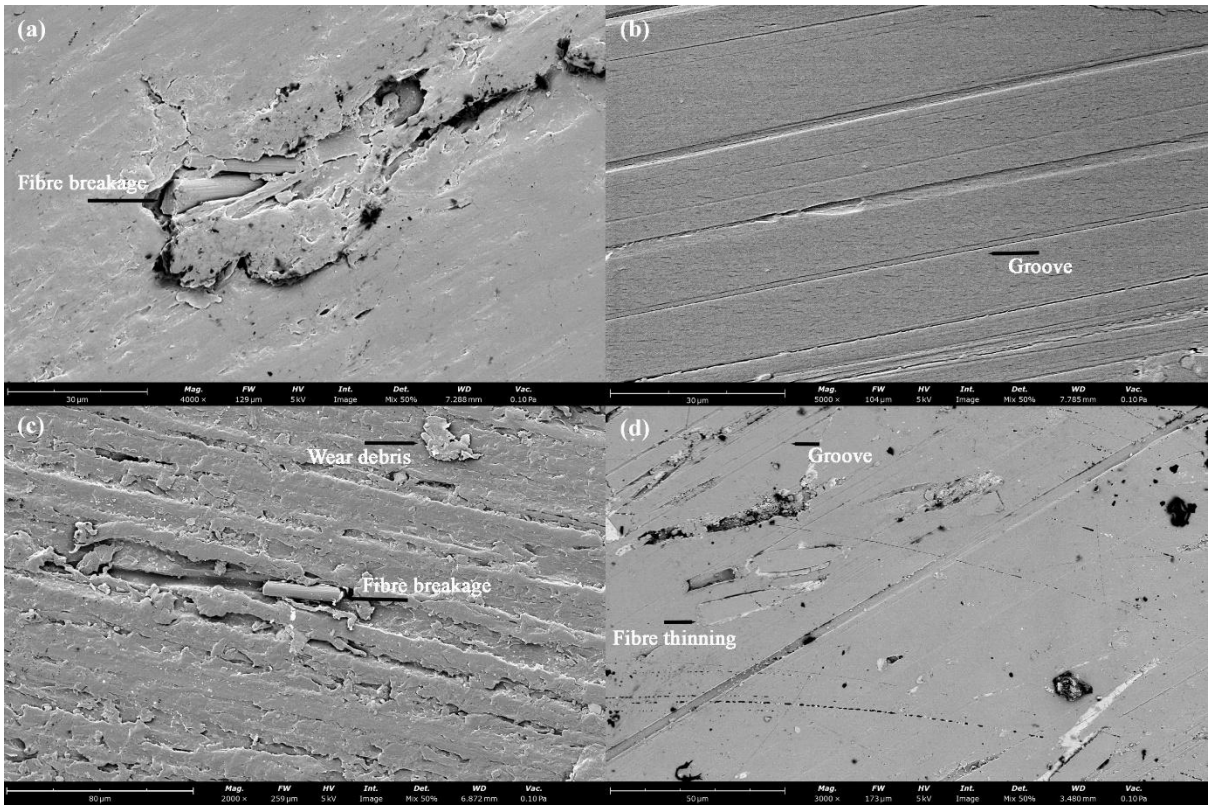

Fig 5.9 SEM of the contact surface of solid benchmark and re-entrant auxetic structures in CF-PLA: (a) solid benchmark-5N, (b) Re60-5N, (c) solid benchmark-10N, (d), Re60-10N

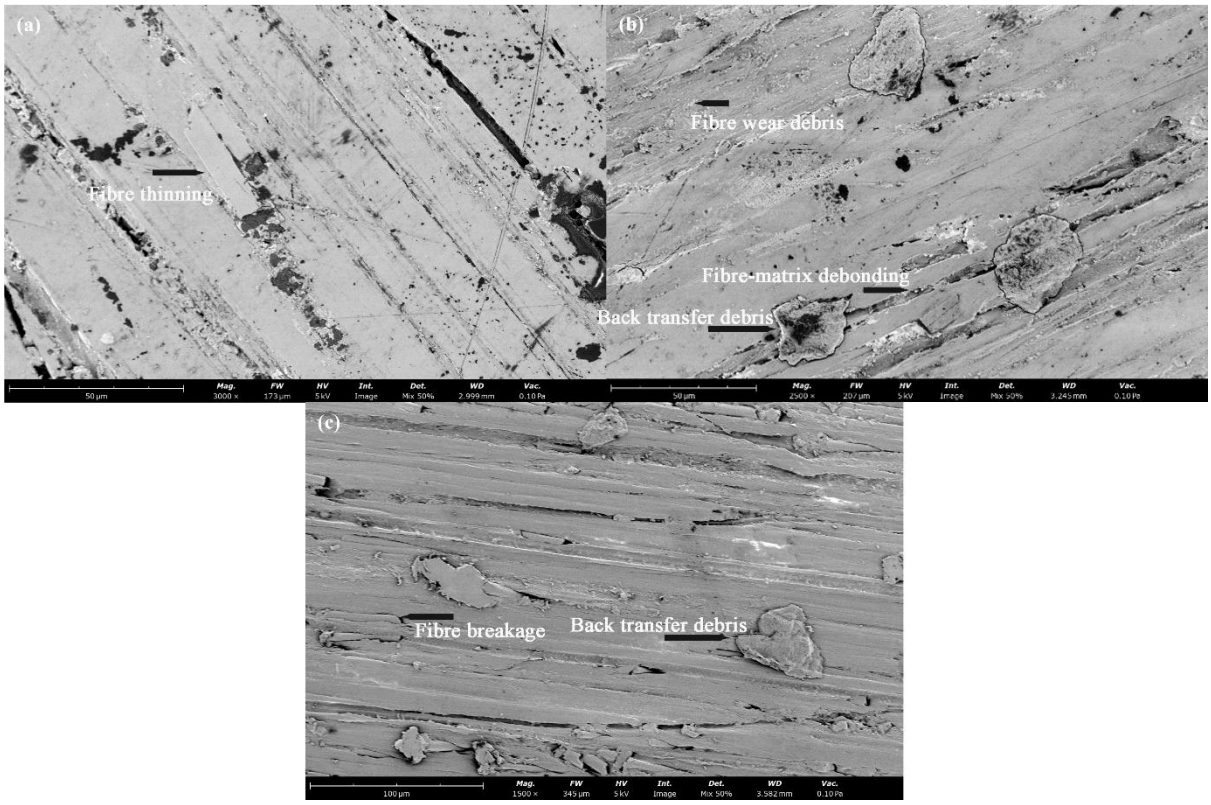

Fig 5.10 SEM of the contact surface of re-entrant auxetic 20 degrees under the applied normal load: (a) 10N, (b) 15N, (c) 20N

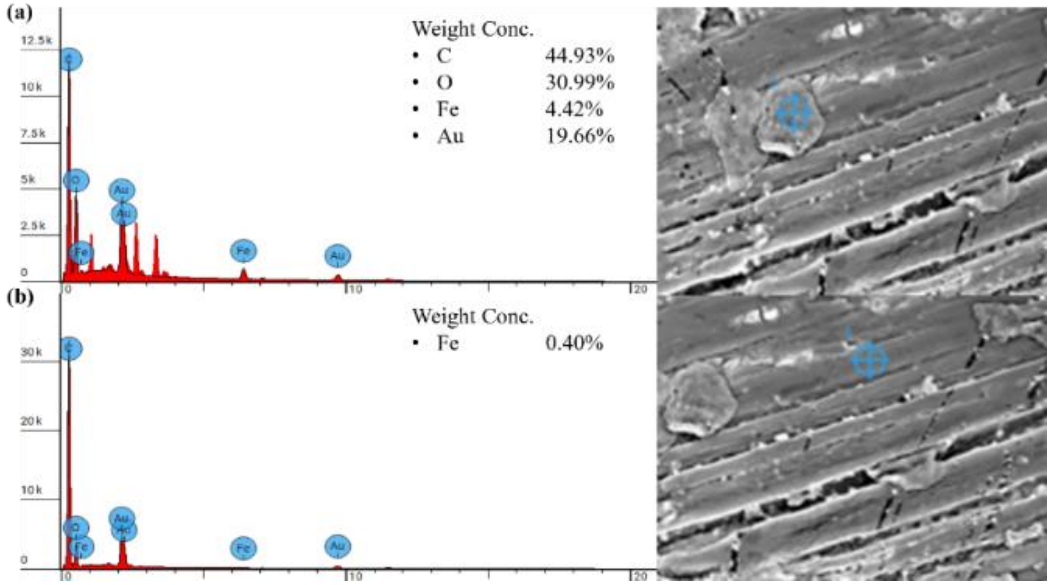

Fig 5.11 EDS result of re-entrant auxetic 20 degrees in CF-PLA under 20N: (a) wear debris, (b) worn surface

To further investigate the tribological effects of the selected re-entrant angles, Fig 5.10 and Fig 5.12 compare the worn surfaces of CF-PLA specimens with re-entrant structures at angles of

20° and 60°, subjected to different loads. As previously discussed, the reduction in fibre impact vibrations (FIV) increases with the re-entrant angle, due to enhanced energy absorption capacity. This led to distinct surface wear patterns for the two re-entrant configurations. As shown in Fig 5.10, with increasing load, smearing of wear debris and fibre debonding were observed. When the load reached 20 N, as seen in Fig 5.10(c), noticeable fibre breakage occurred, accompanied by larger wear debris adhered to the worn surface. EDS analysis revealed that the attached debris contained significantly higher iron (Fe) content (~4%), which was considerably higher than in other areas of the worn surface (Figure 5.11). In general, in polymer-steel sliding pairs, material transfer predominantly occurs from the polymer to the steel, due to the higher surface energy of the steel. Therefore, only minimal Fe content is typically found on the worn surface of the polymer specimen. The higher Fe content in the attached debris suggests that some material has been transferred back from the metal counterface.

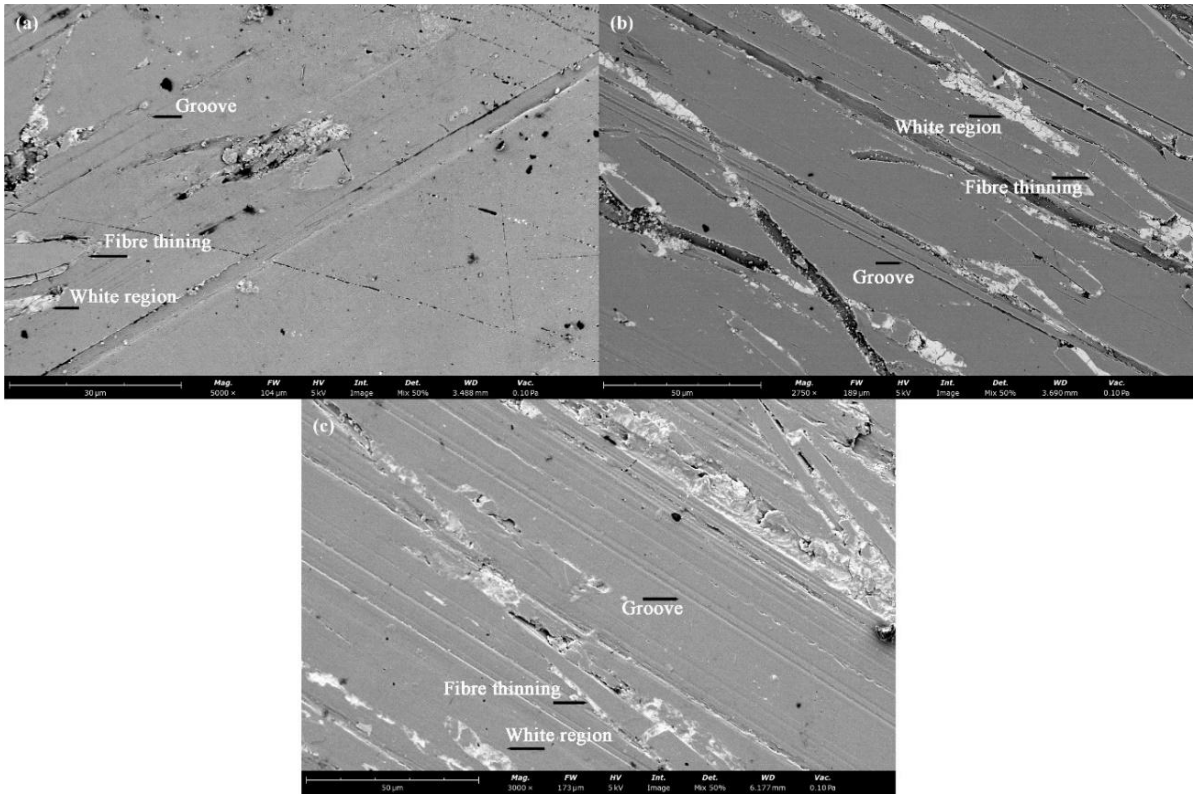

Fig 5.12 SEM of the contact surface of re-entrant auxetic 60 degrees under the applied normal load: (a) 10N, (b) 15N, (c) 20N

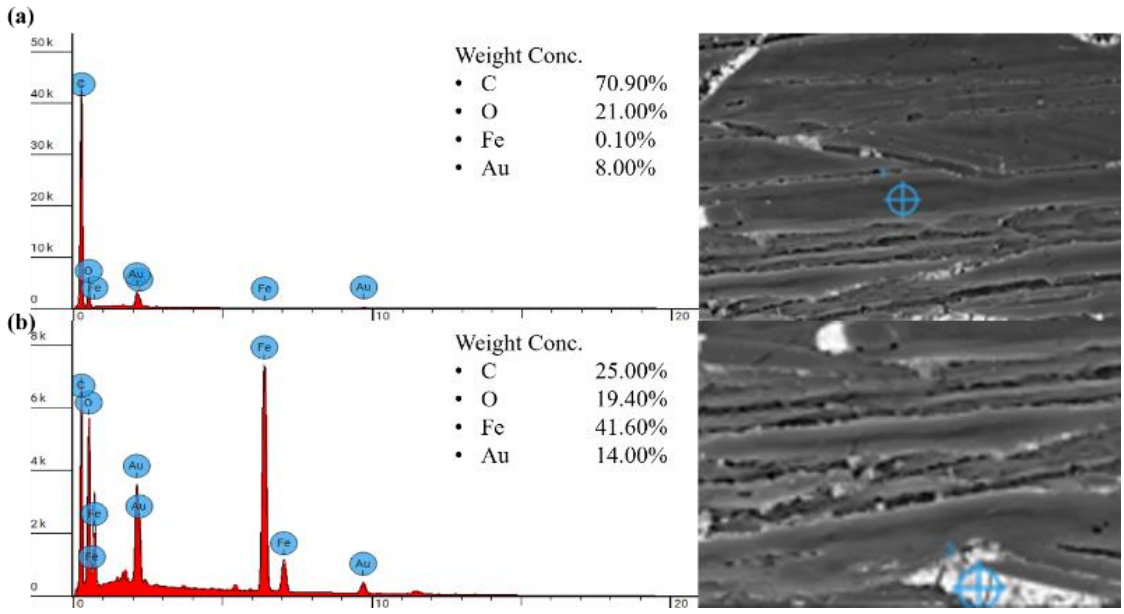

Fig 5.13 EDS result of re-entrant auxetic 60 degrees in CF-PLA under 15N: (a) worn surface, (b) "white" debris

For the re-entrant auxetic structure with a 60° angle, at relatively low loads, the CF-PLA samples exhibited similar dominant wear characteristics to those at 20°, but with fewer grooves and less wear debris accumulation. This was attributed to the more stable vibrations induced in the fibres (Figure 5.12a). As the load increased to 20 N, the worn surfaces remained smooth, with fibre thinning becoming the predominant wear feature. Bright white regions were observed near the fibres, particularly under higher loads. EDS analysis revealed extremely high iron (Fe) content in these areas, exceeding 40% (cf. Figure 5.13), which is two orders of magnitude higher than in other regions of the worn surfaces. It is proposed that during the wear process, the harder fibres protrude from the polymer matrix and become fully exposed to the steel counterface. In this scenario, the fibres bear most of the load, undergoing thinning and breakage. Simultaneously, the fibres scratch the steel surface, leaving metal debris in the contact regions. To validate this proposed mechanism, the surface profiles of the steel counterfaces were further examined using both a laser profilometer and high-resolution AFM and results are shown in Fig 5.14.

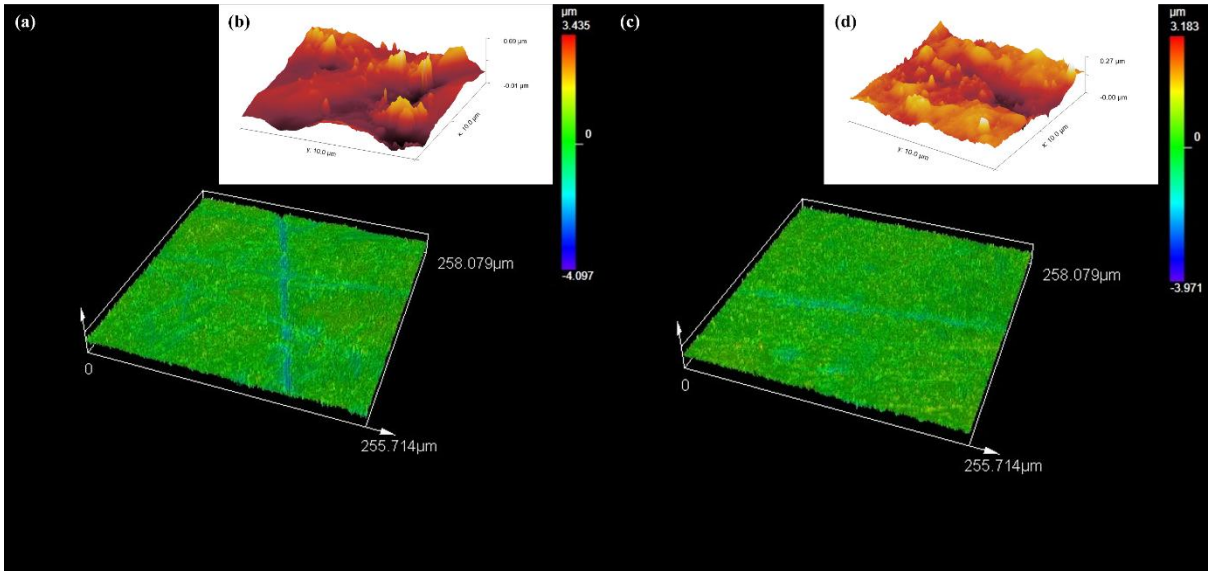

Fig 5.14 Worn surface of metal disk ring to the re-entrant auxetic structure in CF-PLA under 20N: (a) metal disk ring of Re20, (b) AFM metal disk ring of Re20, (c) metal disk ring of Re60, (d) AFM metal disk ring of Re60

It was observed that the metal disk ring in contact with the CF-PLA specimen featuring the re-entrant auxetic structure at 60° exhibited a much lower surface roughness (0.281 μm) compared to the steel ring in contact with the specimen at 20° (0.402 μm). High-resolution AFM images revealed that the surface of the steel ring was smoother, with fewer high, steep roughness peaks. This can be attributed to the proposed scratching or polishing effects of the fibres during wear. Based on these observations, a wear model for CF-PLA with re-entrant structures was proposed and illustrated in Fig 5.15**.** At higher re-entrant angles, FIV was more effectively suppressed. In this case, the continuous sliding contact between the fibres and the steel resulted in a mild abrasion process, leading to fibre thinning and a polishing effect on the steel surface. However, at lower re-entrant angles (or no re-entrant structures), with higher FIV, more fibre damage occurred due to oscillation impacts from the hard asperities, while the surface of the steel counterpart showed minimal modification. The resultant fibre debris could further increase the wear loss by introducing three-body abrasive wear. It is important to note that friction oscillation is closely linked to FIV (see Figure 5.3). In general, larger FIVs correspond to higher friction fluctuations, which progressively exacerbate surface damage, particularly in the form of fatigue and fretting. As a result, more polymeric wear debris would be generated in the interface region. Under the shear and oscillation conditions, material transfer occurred between the contact pairs, with back-transfer from the steel counterface to the polymer surface.

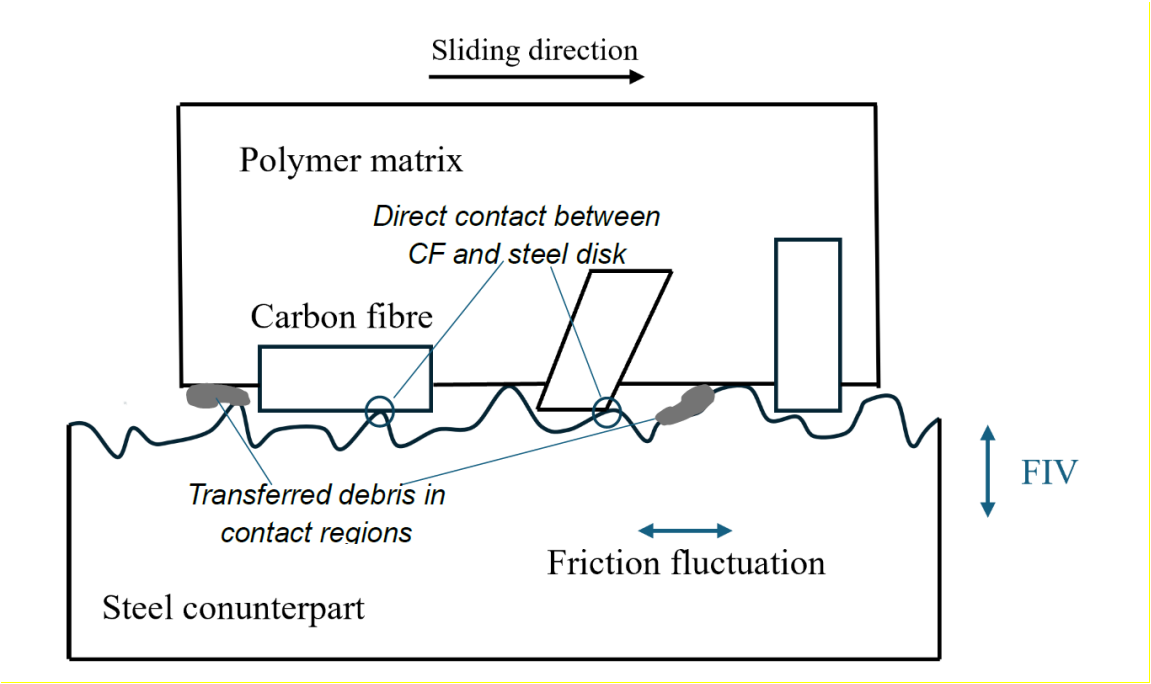

Fig 5.15 Schematic illustration of the contact mode for the sliding wear of carbon fibre with the steel counterpart. During the wear process, the carbon fibre in CFRPs undergo the main load but different levels of vibration. In this case, the higher vibration of re-entrant auxetic 20 degrees (colour of blue, cf Fig 5.8c) intensified the fibre metal interactions, promoting the fibre damage and metal transfer. Whereas the stable contact of 60 degrees (colour of red, cf Fig 5.8c) in a lower vibration promotes the gradual fibre thinning and localized metal accumulation

5.4 Conclusions

This chapter studies the use of embedded re-entrant auxetic structures to improve the tribological performance of CF-PLA composite through 3D printing technology. In particular, the effects of the re-entrant auxetic structure on FIV and wear properties of CF-PLA against steel counterparts were investigated under different loading conditions. The following conclusions can be drawn:

(1) The embedded re-entrant auxetic structure effectively reduces friction-induced vibration (FIV) and associated noise in polymer-steel sliding pairs. This effect is more pronounced when larger auxetic angles are used, as they produce more negative Poisson's ratios and, consequently, higher energy absorption capacity. However, these larger angles also create higher stress concentrations within the re-entrant structures, especially at nodes and joints, increasing the risk of premature

failure. Therefore, selecting the appropriate auxetic structure requires careful consideration of both its energy absorption capabilities and load-bearing capacity, tailored to the specific application requirements.

(2) The wear mode of vibration driven dynamic contact region was built based on microscopy observations. In general, higher FIV levels intensify fiber-metal interactions, exacerbating surface damage and fiber removal, which reduces load-bearing capacity. However, by incorporating re-entrant structures—particularly those with higher auxetic degrees that more effectively suppress FIV—stable, continuous sliding contact between the fiber and steel is achieved. This results in a mild abrasion process, leading to fiber thinning and a polishing effect.

This research demonstrates an innovative approach for designing high-performance engineering components, combining advanced material selection, functional structural design, and lightweight features for diverse operational environments, all facilitated by additive manufacturing technology.

Chapter 6 Effects of environmental temperatures on tribological performance of 3D-printed PLA & PEEK structures

In the previous Chapter, the effect of usage of carbon fibre reinforced PLA composites with complex structures on reducing the friction-induced vibration and wear was systematically investigated. As noted in Chapter 1 Introduction, the works of literature indicates a growing research interest on investigating the thermal behaviour and environmental performance of the FDM-printed parts under the influenced of temperature effects [220], [221]. Such investigations are critical for ensuring the long-term service life of the FDM-fabricated parts in the engineering applications of aerospace, medical, automotive, and microelectronics operating at elevated temperatures [169], [222]. Further, the temperature has a major influence on the wear behaviour, and its effect on the tribological performance of high-performance polymers needs to be further explored, particular with the involvement of complex structure design [63], [64], [223]. Therefore, building upon previous chapters, the effects of the environmental temperatures to the tribological performance of 3D-printed PLA and PEEK structures were systematically investigated in this Chapter.

Neat polylactic acid (PLA) and polyether ether ketone (PEEK) was employed, and the re-entrant auxetic structures were embedded into the printed wear model to suppress the friction-induced vibrations. The experimental results showed that integrating the re-entrant wear model with high-performance polymers ensure the functionality at elevated temperatures. However, the environmental temperatures had complex effects on the wear performance of the two polymers. The specific wear rate of PLA generally increased from 0.0000236 $mm^3/(N \cdot m)$ at room temperature to 0.000472 $mm^3/(N \cdot m)$ operating at 60°C, whereas it had an initial decreased from 0.00000318 $mm^3/(N \cdot m)$ at room temperature to 0.00000292 $mm^3/(N \cdot m)$ operating at 90°C, but a sudden rise to 0.0000135 $mm^3/(N \cdot m)$ at higher environmental temperatures at 110°C for PEEK. The SEM revealed that this difference was attributed to the glass transition state and viscoelastic behaviour in accordance with the change of loss modulus, Tan(delta), and storage modulus at different temperatures. This finding demonstrated that an essential guidance for the designing high-performance engineering components by integrating temperature-responsive advanced material selection with functional structural design and lightweight features dedicated to the service life at different temperature regimes, all facilitated by additive manufacturing technology.

6.1 Test Settings

As seen in Fig 6.1, a heating oven was placed to enclose the wear model, fixtures, steel counterparts, fixtures, and the rotation platform, thereby enabling controlled elevation and stabilization of the testing environmental temperature. All wear models were tested below or near the T_g (glass transition temperature) of neat PLA and PEEK, as identified in Fig 3.2 above.

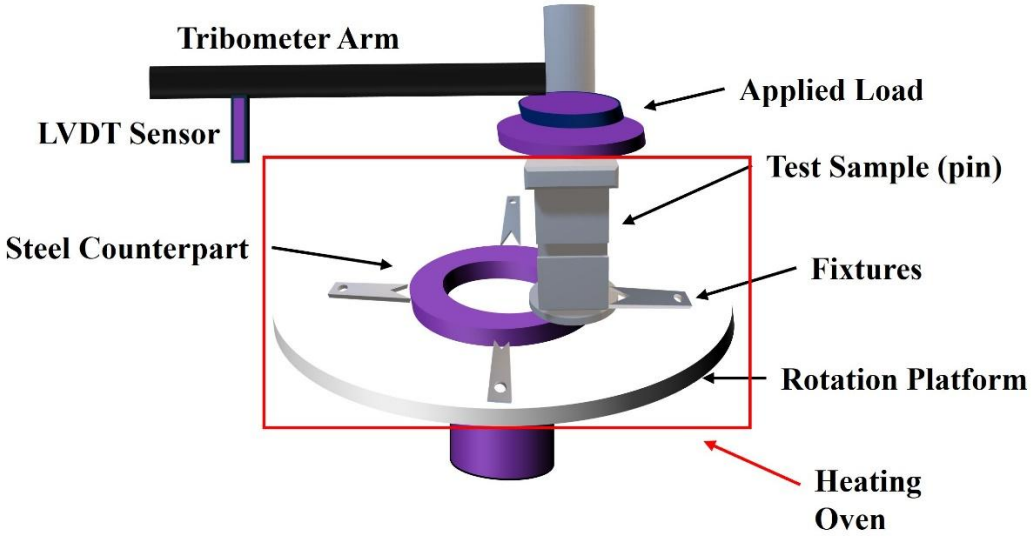

Fig 6.1 Schematic of pin-on-disk wear test machine and setup with heating oven

Table 6.1 presents the material selection, applied normal loads, and the testing environmental temperature of the pin-on-disk wear test. All wear models were tested below or near the T_g (glass transition temperature) of neat PLA and PEEK, as identified in Fig 3.2. As T_g marks the transition state from a rigid glassy to a softer viscoelastic state, it significant influences the material modulus and mechanical stability, and promoting the plastic deformation and adhesive wear. Consequently, the friction and wear behaviour were strongly influenced by temperature approaching T_g. The selection of applied normal loads of 5N for PLA and 25N for PEEK was followed by the established testing conditions of PLA and PEEK structures in Chapter 4, allowing direct comparison of the influence of the external environmental temperature. The test duration was settled 270 mins. The variation of the test duration may observe due to the temperature stabilization requirements of heat oven at different targeted temperatures. Nevertheless, the sliding duration in all testes was sufficient to reach steady-state wear conditions, ensuring the comparability of the tribological results.

Table 6.1 Test Setup

No. of tests	Material	Applied Normal Load (N)	Testing Temperature (°C)
1	Neat PLA	5N	40
2			60
3	Neat PEEK		40
4		25N	Room
5			40
6			60
7			90
8			110

6.2 Effects of environmental temperature on wear behaviour of the wear mode in PLA

Fig 6.2 compares the typical friction responses of the printed re-entrant auxetic wear model in PLA under different testing temperatures. All tests were carried out under the applied load at 5N and a constant disk rotation speed of 120 rpm. For the re-entrant wear model tested at both room temperature and elevated to 40°C, the CoF was observed slightly increased at the initial stage, likely due to the enlarged real contact area by the wear of surface asperities, as seen in Fig 6.2(a). Nevertheless, the increased CoF has been shortened from 200 min at room temperature to approximately 72 min with the increase of the environmental temperature to 40°C. Similarly, a slight increase in CoF at the initial stage was also observed but the duration of this period was further reduced to approximately 30 min when the environmental temperature was further increased to 60°C, as shown in Fig 6.2(b). Notably, the re-entrant wear model in 40°C and 60°C shared a similar CoF pattern, but more intensive CoF oscillation beyond 150 min observed in the condition of 60°C as illustrated in Fig 6.2(c). This phenomenon is likely to be associated with thermo-softening and the glass transition of neat PLA due to the testing temperature near its glass transition temperature, which fundamentally changes the nature of the contact interface compared to the room temperature, leads to more CoF fluctuation during sliding [223], [224].

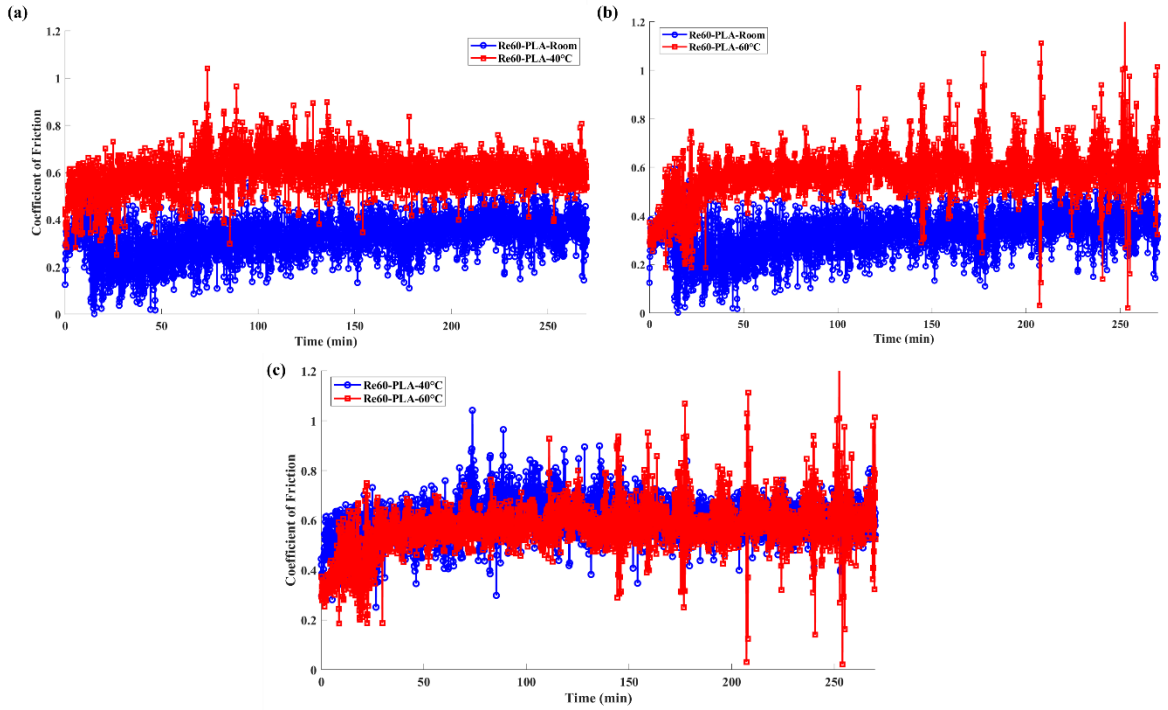

Fig 6.2 Coefficient of friction of re-entrant wear model in PLA under 5N: (a) room temperature and 40°C, (b) room temperature and 60°C, (c) 40°C and 60°C

The pronounced fluctuations in friction shown above are generally associated with vibrations, the FIV (friction-induced vibrations) in the sliding system [200], [201]. In this paper, the vibration amplitude was calculated in Eq.4 and Fig 2.7 using the captured the vertical displacement of sliding samples with LVDT sensor. Fig 6.3 compares the friction-induced vibration result of the re-entrant wear model influenced by the variable environmental temperature. It is clear that the re-entrant wear model under room temperature suppressed the FIV more effectively compared to higher temperatures, corresponding to the vibration amplitude in 0.00102 mm under room temperature, 0.00178 mm in 40°C, and 0.00206 mm in 60°C. The highest vibration amplitude at the 60°C was consistent with the observed stronger CoF fluctuations beyond 150 min at the same temperature, as shown in Fig 6.2(c). This behaviour is likely due to the thermomechanical responses of the printed PLA operating near its glass transition temperature, which the enhanced viscoelastic deformation and the mechanical instability promoted the pronounced interfacial friction fluctuations and the friction-induced vibration [225].

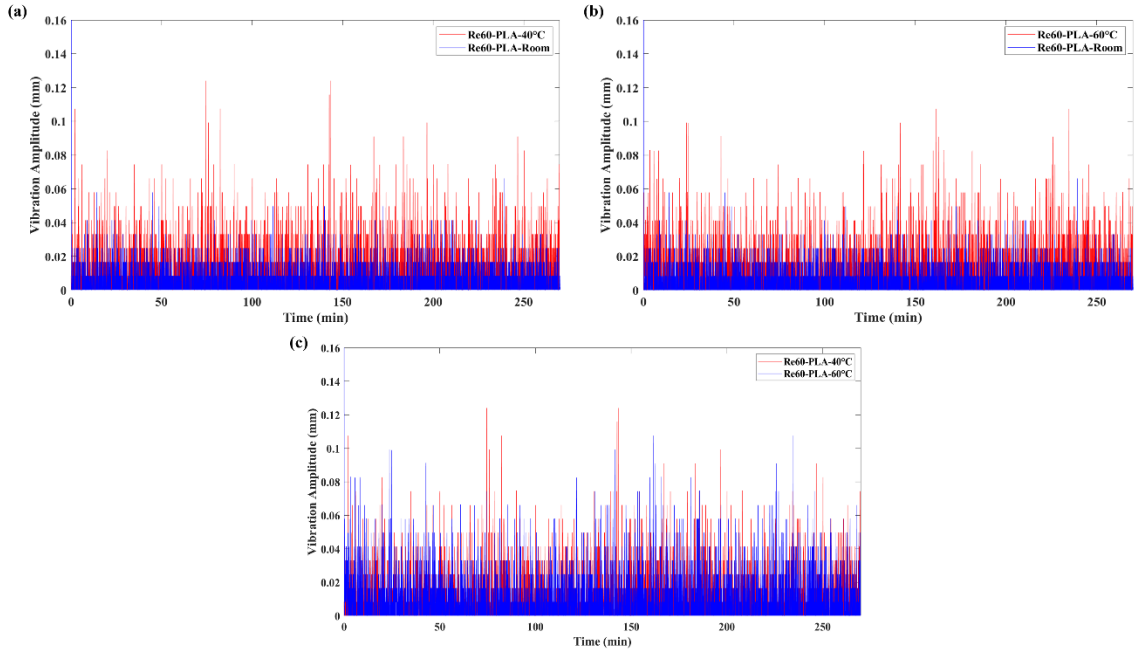

Fig 6.3 Vibration amplitude of re-entrant wear model in PLA under 5N: (a) room temperature and 40°C, (b) room temperature and 60°C, (c) 40°C and 60°C

Fig 6.4 demonstrates the SWR (specific wear rate) of the re-entrant wear models influenced by different environmental temperatures. As seen in Fig 6.4, the SWR of re-entrant wear models generally increased. Notably, the SWR in the test condition of 60°C had a significant increase from 0.0000236 $mm^3/(N \cdot m)$ to 0.000472 $mm^3/(N \cdot m)$.

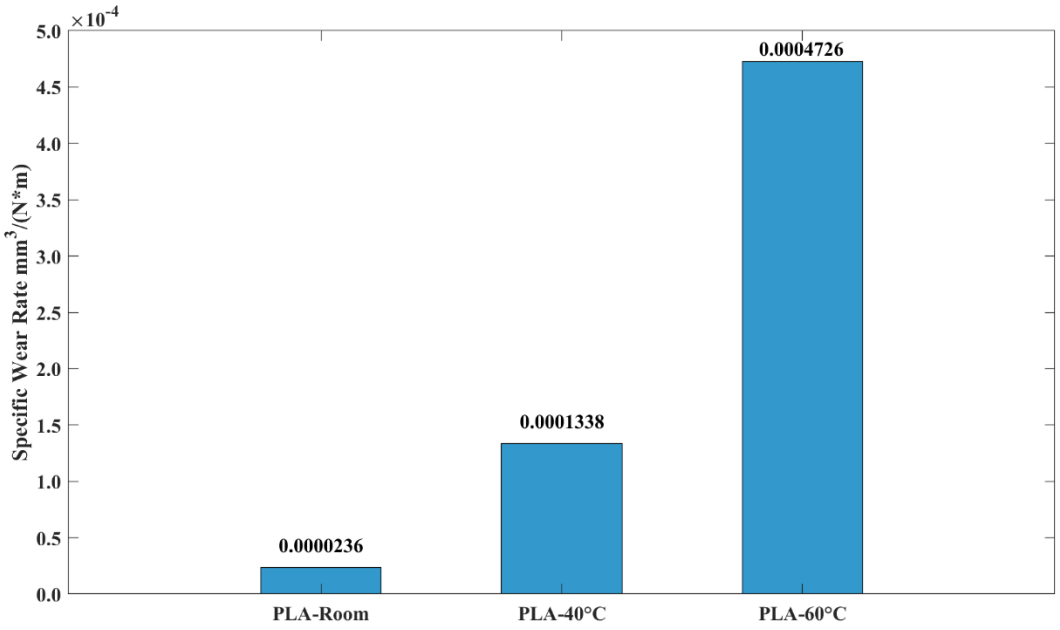

Fig 6.4 The effect of environmental temperature on re-entrant wear model in PLA at 5N

6.3 Effects of environmental temperature on wear behaviour of the wear mode in PEEK

Fig 6.5 compares the typical friction responses of the printed PEEK wear model tested under multiple environmental conditions. All tests were carried out under the applied load of 25N and the same disk rotation speed as the PLA sample. As seen in Fig 6.5(a), the coefficient of friction of re-entrant wear model tested at room temperature was slightly increased at the running-in stage which shared the similar reason of PLA due to the enlarged real contact area by the wear of the surface asperities. This period has been slightly reduced to approximately 160 min when the environmental temperature slightly increased to 40°C. Notably, a further increasing the environmental temperature led to different CoF patterns. Under the influence of environmental temperature at 90°C, the CoF displayed an initial reduction trend and a subsequently increased trend beyond 68 min until reaching the steady state at 240 min as seen in Fig 6.5(b). More interestingly, at 110°C, the slightly increased of CoF at the initial running-in stage extended to approximately 250 min as shown in Fig 6.5(c).

Fig 6.6 presents the vibration amplitude of re-entrant wear model under different environmental conditions printed in PEEK. As seen through Fig 6.6(a) to Fig 6.6(c), no substantial differences observed on the vibration amplitude at different temperatures, indicating that integrating the developed re-entrant wear model with the high-performance polymer was able to maintain functionality under a high operating temperature environment. In addition, it is worth to note that the vibration amplitude was slightly increased from 0.00109 mm to 0.00140 mm when the testing environmental temperature elevated to 110°C. This behaviour is likely due to the thermomechanical responses of neat PEEK, which the partial softening of the material increases the viscoelastic behaviours and reduction of the inherently damping capacity, leading to the more pronounced friction-induced vibration [226], [227].

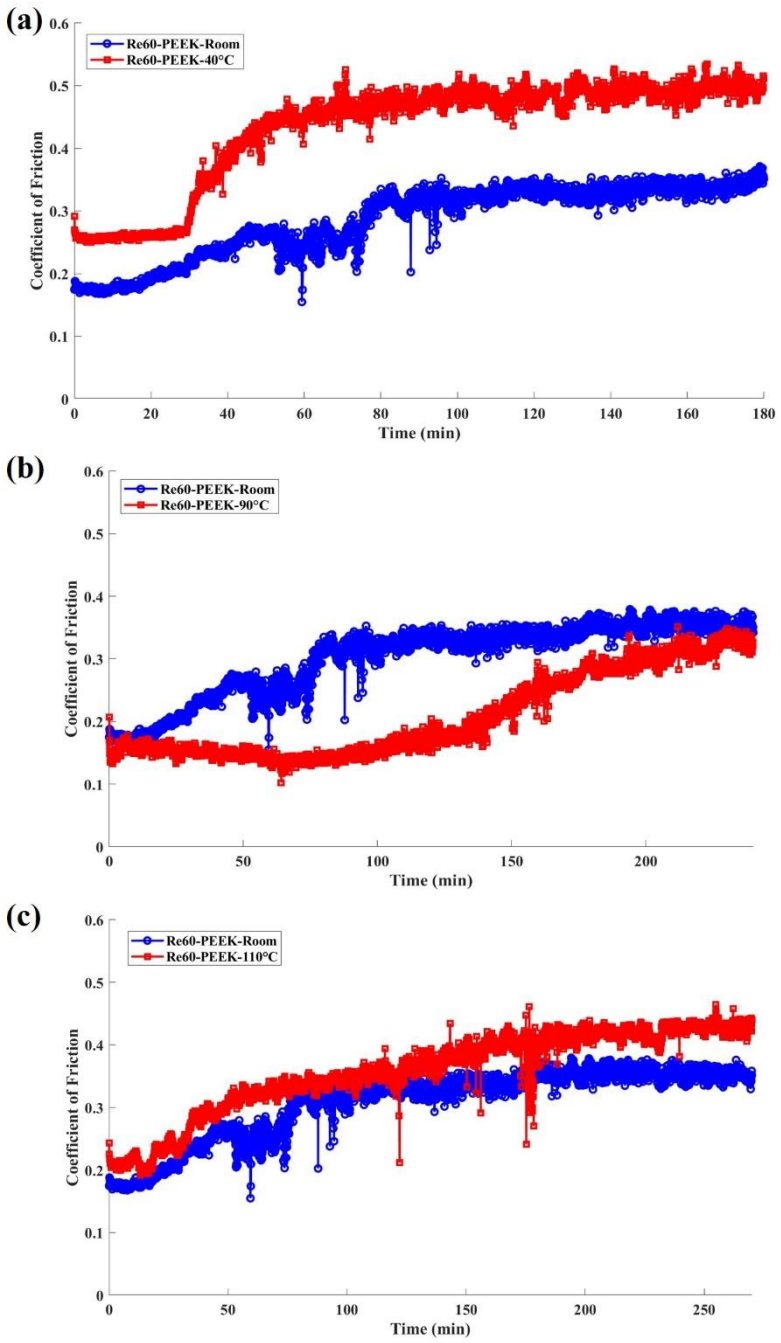

Fig 6.5 Coefficient of friction of re-entrant wear model in PEEK under 25N: (a) room temperature and 40°C, (b) room temperature and 90°C, (c) room temperature and 110°C

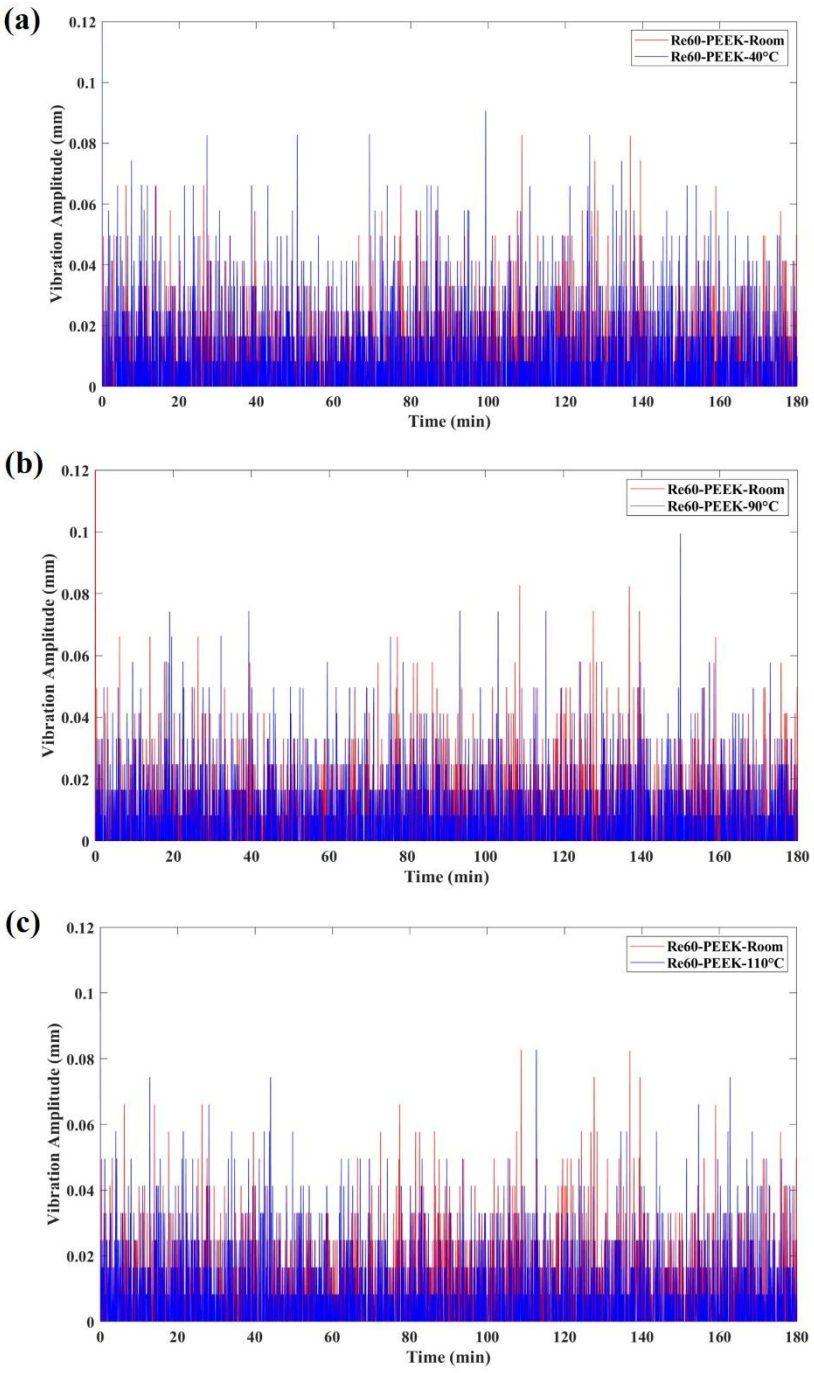

Fig 6.6 Vibration amplitude of re-entrant wear model in PEEK under 25N: (a) room temperature and 40°C, (b) room temperature and 90°C, (c) room temperature and 110°C

Operating with the elevated temperature, specifically near the glass transition temperature, had the detrimental effect on the wear model made in PLA, as shown in Fig 6.4. However, the PEEK sample exhibited a more complex trend. As seen in Fig 6.7, the specific wear rate of the re-entrant wear model was generally decreased below 90°C whereas a sudden escalation at 110°C, where the SWR of the re-entrant wear model increased from 0.00000318 $mm^3/(N \cdot m)$

at room temperature to 0.0000135 $mm^3/(N \cdot m)$ at 110°C. To further understand the underlying mechanism of this interesting SWR result shown in PLA and PEEK influenced by the environmental temperature, the worn surfaces were examined using SEM, as discussed in the following section.

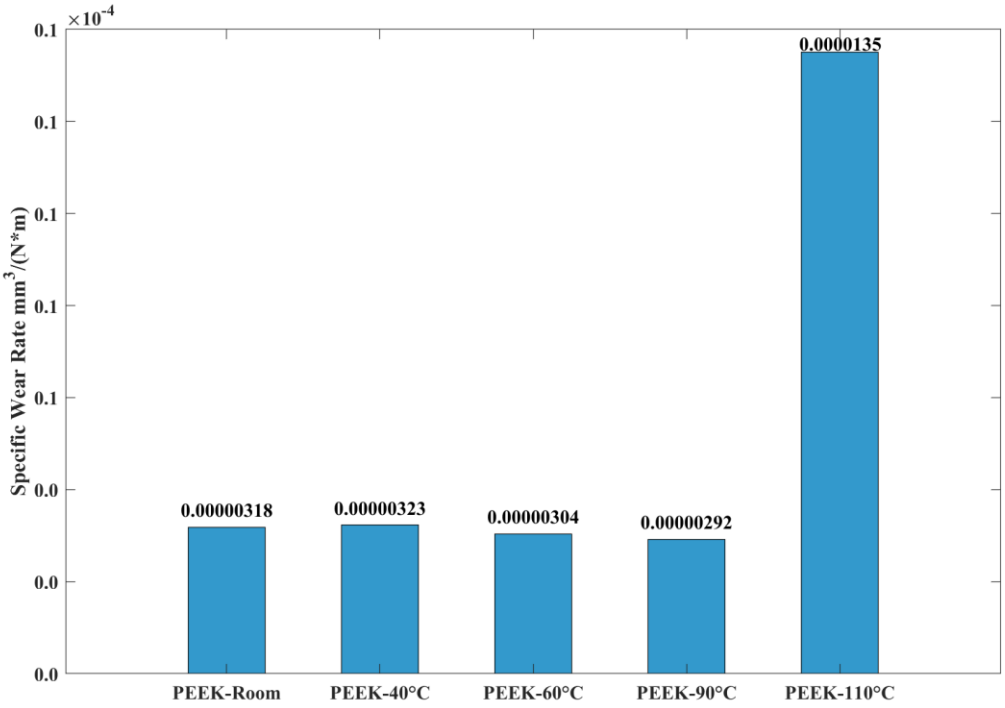

Fig 6.7 The effect of environmental temperature re-entrant wear model in PEEK at 25N

6.4 Wear features of the effect of environmental temperature on PLA and PEEK with re-entrant structures

Fig 6.8 presents the SEM images of the worn surfaces of the printed PLA under different environmental temperatures. As seen in Fig 6.8(a), with the stabilized CoF (cf Fig 4.13a) and suppressed FIV (cf Fig 4.14a) at room temperature, only uniform light grooves without observation of clear cracks shown on the worn surface of the re-entrant wear model. With the operating environmental temperature increased to 40°C, clear evidence of thermo-softening features with light grooves and a slightly increased distribution of the wear debris was observed on the worn surface. The increased loss modulus and Tan(delta) and decreased storage modulus shown in Fig 3.2(a) indicates the PLA had a transition from a glassy and rigid state to a softer state. This glass transition facilitates the plastic deformation and adhesive wear, thereby promotes the formation of the thermo-softening wear features [228]. With a temperature

elevation to 60°C, more distribution of wear debris and cracks were observed on the worn surface. Operating near the glass transition temperature, the PLA reached a highly viscoelastic state where the increased loss modulus nearly equals to the decreased storage modulus, leading to the reduction of the surface stiffness and maximum softening [229]. Consequently, the material breaks off easily sliding against the steel counterpart due to the intensified CoF oscillation (cf Fig 6.2b) and vertical impact on the contract surface from more pronounced friction-induced vibration (cf Fig 6.3b), leading to the production of more wear debris. Further, the repeated sliding on the softer polymer surface results in the formation of cracks [230].

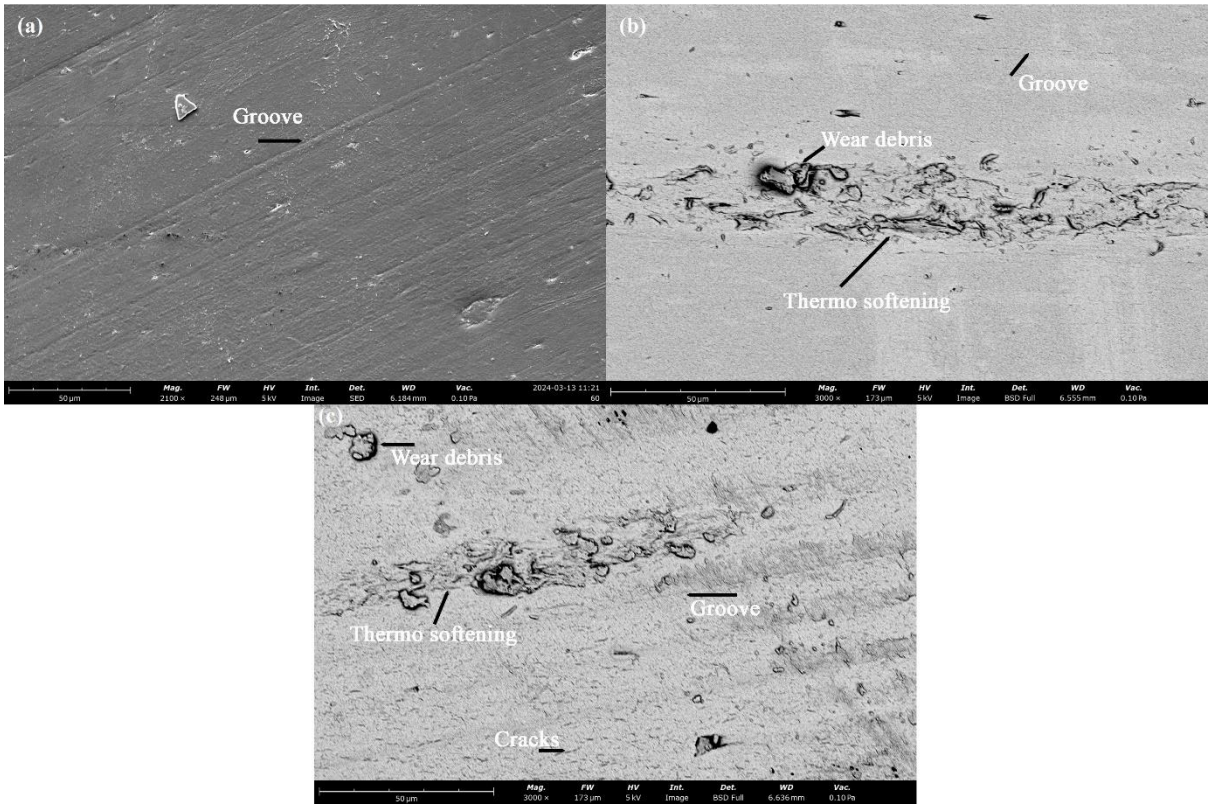

Fig 6.8 SEM of the contact surface re-entrant wear model in PLA at 5N: (a) room temperature, (b) 40°C, (c) 60°C

For comparison, thanks to inherently exceptional mechanical thermal stability of neat PEEK, only light grooves with no clear thermal softening wear features observed on the worn surface of re-entrant wear model at room temperature and 40°C, as shown in Fig 6.9(a) and Fig 6.9(b). With the increased of environmental temperatures to 90°C, uniform light grooves, a slight increased distribution of wear debris and a clear micro-ploughing feature was observed on the worn surface, as see in Fig 6.9(c). Although the decreased loss modulus and Tan(delta) reflected the reduced mechanical energy dissipation ability as heat, but the storage modulus remains

unchanged, indicating the elastic stiffness of the PEEK remain largely unaffected, as illustrated in Fig 3.2(b) [231]. In this case, the combination leads to the increased local stress at the counter interface, promoting the micro-ploughing sliding against the steel counterpart. Nevertheless, the unaffected stiffness ensures the resistance to an abrupt material removal. Further, at 90°C, the slight softening of the contract surface of polymer promotes a more extensive and adherent protective transfer film against wear [232]. Upon a further increased in temperature to 110°C, closer to the glass transition temperature, the SEM revealed wider and deeper grooves with a distribution of wear debris, as depicted in Fig 6.9(d). Notably, a distinct wear debris adhered on the steel counterpart after the test as seen in Fig 6.10(a). With a further reduction on the loss modulus and Tan(delta), the material became ductile, and the steel asperities were easier to penetrate and displace the softer PEEK material, leading to the formation of deep grooves. Meanwhile, the soften PEEK adhered on the steel counterpart forming a transfer film. This formation changes the local contact from polymer-metal to polymer-polymer, results in more localized heat and facilitated the accumulated the wear debris.

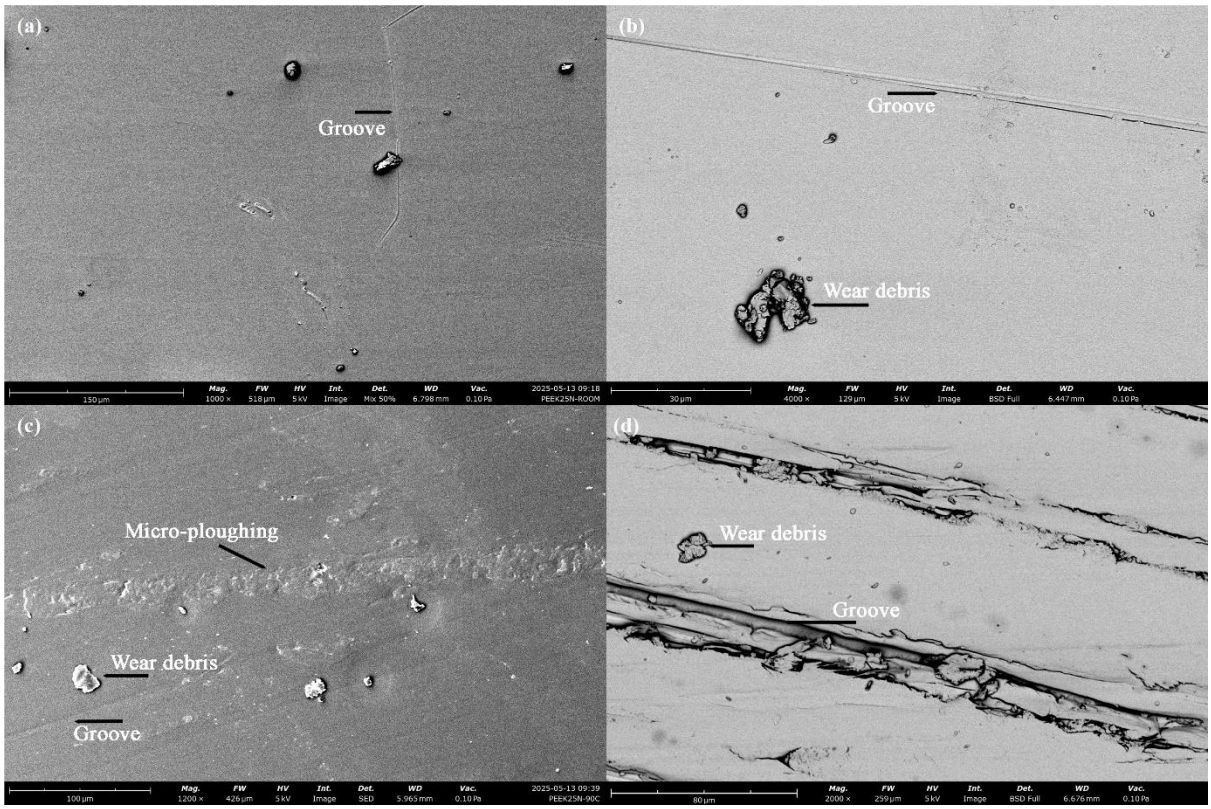

Fig 6.9 SEM of the contact surface re-entrant wear model in PEEK at 25N: (a) room temperature, (b) 40°C, (c) 90°C, (d) 110°C

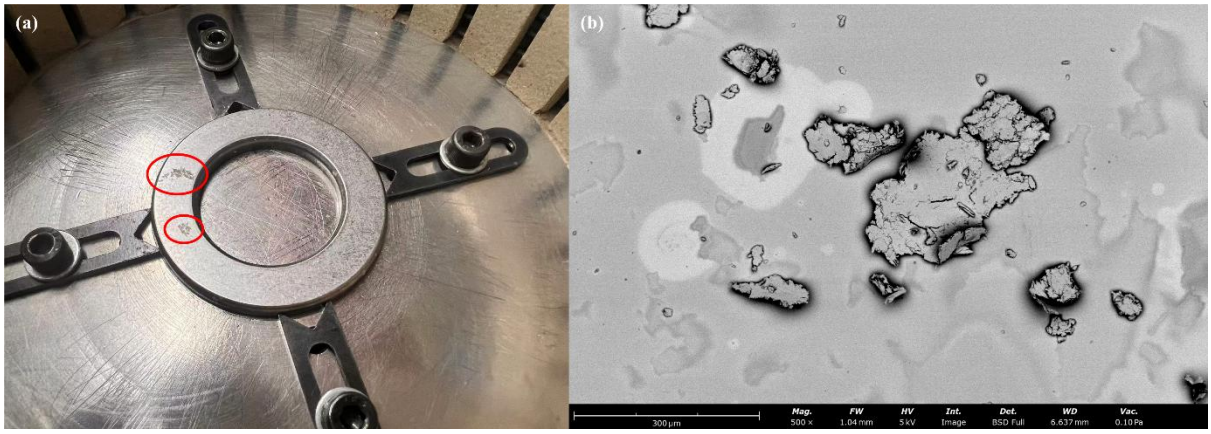

Fig 6.10 Attached wear debris of re-entrant wear model at 25N in PEEK at 110°C: (a) Image on steel counterpart, (b) SEM adhered on the polymer counterface

6.5 Conclusions

This paper applied the effects of the environmental temperature to PLA and PEEK materials and structures fabricated with FDM method. The effects of environmental temperature on the tribological performance of the printed re-entrant wear models was compared. The following conclusions can be drawn:

(1) Under all testing conditions, the friction-induced vibration can be effectively suppressed with the embedded re-entrant auxetic structures due to their high energy absorption and vibration damping ability. With the elevated environmental temperatures, the thermomechanical responses of the materials lead to a more pronounced FIV of printed specimens.

(2) The environmental temperature had complex effects on the specific wear rate (SWR) of the materials. Operating near the glass transition temperature of the polymer influenced the wear behaviour of the printed samples, leading to a significant increase in the specific wear rate. In PLA, the specific wear rate had a generally increasing trend with temperature 0.0000236 $mm^3/(N \cdot m)$ at room temperature to 0.000472 $mm^3/(N \cdot m)$ operating at 60°C. In contrast, for PEEK, the specific wear rate exhibited an initial decreased trend from 0.00000318 $mm^3/(N \cdot m)$ at room temperature to 0.00000292 $mm^3/(N \cdot m)$ operating at 90°C, but a sudden rise to 0.0000135 $mm^3/(N \cdot m)$ at higher environmental temperatures at 110°C. The SEM reveals that glass transition state and viscoelastic behaviour in accordance with the change of loss modulus, Tan(delta), and storage modulus at different temperatures contribute to different worn surface conditions.

Chapter 7 Conclusions and Outlook

7.1 Conclusions

In the present research, a series of testing specimens manufactured from neat polylactic acid (PLA), carbon fibre reinforced polylactic acid (CF-PLA), and polyether ether ketone (PEEK) were fabricated with FDM method. The post-heat treatment was subsequently applied. A systemically investigation was conducted initially to evaluate effects of post-heat treatment on the dimensional accuracy and mechanical properties on the 3D-printed PLA and PEEK, as well as the tribological performance incorporating with complex structures design. Meanwhile, the factors of material selections and structure design with the utilization of CFRPs were investigated to address the identified limitation. Furthermore, the influence of external environmental stimuli, specifically the environmental temperature, on the complex structure design performance was evaluated and compared. The summary of key findings and conclusions of the thesis work are drawn as follows.

The sample after the heat treatment exhibited a higher result of introduced mean absolute deviation (MAD), indicating the fact of the systematically shrinkage of the heat-treated sample which is primarily attributed to the increased degree of crystallization and relief of internal stress. Meanwhile, the proposed heat treatment resulted in a higher degree of crystallinity and, consequently, improved strength for both printed materials. For PLA, the tensile strength was enhanced from 44.14 MPa to 47.66 MPa, as well as the compressive strength improved from 68 MPa to 82 MPa. A similar trend was observed in heat-treated PEEK. The tensile strength increased from 75.53 MPa to 84.91 MPa and the compressive strength enhanced from 106 MPa to 123 MPa. Nevertheless, the post-heat treatment reduced the ductility of PLA while enhancing the ductility of PEEK, which in turn affected their tribological performance subsequently.

The exploration to on the 3D-printed PLA embedded with complex structures in tribological applications was studied initially in order to build the understanding of the wear mechanism for the later comparison between heat-treated PLA and PEEK structures. In the study, for the first time made attempts to use auxetic materials as a new self-tunning absorber for friction vibration control. The results showed that tailoring the re-entrant angles to achieve the desired value of negative Poisson's ratio, the specimen exhibited less vibration with a lower average CoF during the sliding wear process. As a result, the wear resistance of the wear model embedded with re-entrant auxetic structures was clearly improved. The SEM revealed that the

surface fatigue wear was effectively prevented with the employment of the re-entrant auxetic structures owing to their energy absorption and vibration isolation capabilities. Following the successful exploration of AM-fabricated parts incorporating with complex structures for tribological applications, the effects of post-heat treatment on the printed PLA and PEEK structures were studied and compared. The results revealed that the improved material stiffness enabled the re-entrant auxetic structure to reduce the friction-induced vibration (FIV) more effectively. However, the heat treatment resulted in the contrasting effects on the wear resistance of two polymers. The specific wear rate of the heat-treated PLA sample with the re-entrant structure increased from $2.36 \times 10^{-5}\ mm^3/(N \cdot m)$ to $4.5 \times 10^{-4}\ mm^3/(N \cdot m)$, while it decreased for the PEEK sample from $3.18 \times 10^{-6}\ mm^3/(N \cdot m)$ to $6.2 \times 10^{-7}\ mm^3/(N \cdot m)$. The microscopic observation revealed that the change in brittleness, the reduction and improvement in ductility of two polymers after heat treatment, influenced the formation of wear debris and the development of transfer films on the steel counterpart.

Building upon these findings, it was clear that the post-heat treatment enhanced the material strength while simultaneously influencing the dimensional accuracy and inducing complex tribological performance on the FDM-fabricated polymers structures. However, a limitation emerged during the study, which the advantageous energy absorption due to the auxeticity required a significant structural deformation. Given the inherently low strength of PLA, only a relatively low load 5N applied to ensure the auxetic structure deformed within the elastic range. In contrast, the utilization of PEEK enabled a remarkable increase in the applied load, up to 25N. To overcome this constraint and broad the application with a wide range of material selections, the structural design and material selection in the employment of high-performance carbon fibre reinforced composites (CFRPs) under different loading conditions was systematically investigated. The results revealed that incorporating the complex structure designs with CFRPs effectively reduced the friction-induced vibration and associated noise in high loadings in polymer-steel sliding pairs, explained by the proposed wear model of the vibration driven dynamic contact region built from SEM observations. Nevertheless, selecting the appropriate auxetic structures to the specific application requirements takes a careful consideration of the balance between the stress concentration effects and the advanced performance capabilities.

Further, considering the high sensitivity of the AM-fabricated parts to the external environmental stimuli, particularly the environmental temperature factor and its importance for ensuring long-term service life in the engineering applications, the influence of environmental

temperature on the FDM-printed PLA and PEEK structures was systematically investigated. The environmental temperature regimes were determined in accordance with measured glass transition temperature of the selected polymers from the DMA test. The result revealed that integrating the complex structure designs with high-performance polymer effectively suppressed the FIV at elevated environmental temperatures. Notably, the effect of the thermomechanical responses of the materials requires to be considered, as it can lead to a more pronounced FIV of printed specimens. Nevertheless, the environmental temperatures had complex effects on the specific wear rate of the materials, particularly operating near the glass transition temperature. The PLA exhibited a generally increased trend, whereas the PEEK had a decreased trend at first but a sudden rise at higher temperatures. This behaviour is likely attributed to the glass transition state and viscoelastic behaviour in accordance with the change of loss modulus, Tan(delta), and storage modulus at different temperatures based on the microscopy observations.

7.2 Outlook

In the present research, new insights into the utilization of post-heat treatment for tailoring and optimizing the mechanical behaviour of printed polymers while also emphasizing the necessity of systemically evaluating its influence on the tribological performance of AM-fabricated engineering parts subjected to different sliding conditions and thermally demanding environments have been achieved. Nevertheless, certain points can be further studied to deepen the understanding of the achieved main objectives illustrated in Chapter 1.4. Such efforts will further expand the applicability of AM-fabricated parts enhanced with post-processing techniques across different applications fields.

The post-heat treatment was selected as a widely used and cost-effective post-processing techniques for AM-fabricated parts. As summarized in the literature review in Chapter 1.2, other post-processing techniques, such as the chemical treatment, surface coating are also available. Therefore, one of the future works will be carried out to further explore the effects of additional post-processing techniques on the dimensional accuracy, mechanical properties and tribological performance of the 3D-printed polymer structures. In particular, the combination of multiple treatments method may allow further tailoring and optimization of the discussed properties for variable engineering application.

Further, in this research thesis, the effects of external environmental temperature on the AM-fabricated polymer structures performance were systematically investigated. As reported by

literature in Chapter 1.3.3, other external stimuli, such as pressure and humidity also influenced the performance. Therefore, one of the future works will be carried out to further explore the effects of additional external stimuli on the discussed properties of 3D-printed polymer structures. In addition, the comparison group of the FDM-printed polymer structures after the proposed heat treatment could be made to compare the effects of environmental temperature to the heat-treated samples.

Meanwhile, the present research was performed in dry sliding conditions, and the research trend of the advanced polymer and polymer composites are widely utilized in tribological applications with lubricants and coating films. The friction and wear response and mechanisms differ from variable operating conditions. For instance, under the water lubricants, the formation of fluid film reduces the contact area and eliminates the adhesive junctions and facilitates the frictional heat dissipation. Also, coating the film on the counter interface introduced a protective interfacial layer to diminish the asperities contact and suppress the material-removal along with the sliding. Applying either of the condition could influence the tribological performance of the AM-fabricated material structures.

Finally, at the current stage, the FIV was captured using the LVDT sensor in the time-domain, which proved to be feasible and effective approach. As reported by literature, having the frequency domain analysis based on the FFT could help to identify and isolate the specific sources of FIV, such as the specific wear mechanism, noises caused by test rig itself.

Overall, further research could focus on integrating the material selections with functional complex structural design and utilization of post-processing techniques to further enhancing the mechanical behaviours of the AM-fabricated polymer parts while also emphasizing the long-term effects, particularly the tribological performance under external environmental stimuli, and to achieve the desire properties and broaden the applications of next generation AM-fabricated parts.

References

[1] B. C. Gross, J. L. Erkal, S. Y. Lockwood, C. Chen, and D. M. Spence, “Evaluation of 3D printing and its potential impact on biotechnology and the chemical sciences,” *Anal. Chem.*, vol. 86, no. 7, pp. 3240–3253, Apr. 2014, doi: 10.1021/AC403397R/ASSET/IMAGES/LARGE/AC-2013-03397R_0009.JPEG.

[2] R. Kumar, M. Kumar, and J. S. Chohan, “The role of additive manufacturing for biomedical applications: A critical review,” *J. Manuf. Process.*, vol. 64, pp. 828–850, Apr. 2021, doi: 10.1016/J.JMAPRO.2021.02.022.

[3] P. Wang *et al.*, “Preparation of short CF/GF reinforced PEEK composite filaments and their comprehensive properties evaluation for FDM-3D printing,” *Compos. B Eng.*, vol. 198, p. 108175, Oct. 2020, doi: 10.1016/J.COMPOSITESB.2020.108175.

[4] D. Fico, D. Rizzo, R. Casciaro, and C. E. Corcione, “A Review of Polymer-Based Materials for Fused Filament Fabrication (FFF): Focus on Sustainability and Recycled Materials,” *Polymers 2022, Vol. 14,* vol. 14, no. 3, Jan. 2022, doi: 10.3390/POLYM14030465.

[5] P. Jagadeesh *et al.*, “A comprehensive review on 3D printing advancements in polymer composites: technologies, materials, and applications,” *The International Journal of Advanced Manufacturing Technology 2022 121:1*, vol. 121, no. 1, pp. 127–169, May 2022, doi: 10.1007/S00170-022-09406-7.

[6] I. Plamadiala, C. Croitoru, M. A. Pop, and I. C. Roata, “Enhancing Polylactic Acid (PLA) Performance: A Review of Additives in Fused Deposition Modelling (FDM) Filaments,” *Polymers 2025, Vol. 17,* vol. 17, no. 2, Jan. 2025, doi: 10.3390/POLYM17020191.

[7] S. Farah, D. G. Anderson, and R. Langer, “Physical and mechanical properties of PLA, and their functions in widespread applications — A comprehensive review,” *Adv. Drug Deliv. Rev.*, vol. 107, pp. 367–392, Dec. 2016, doi: 10.1016/J.ADDR.2016.06.012.

[8] J. Zhang, G. Lin, U. Vaidya, and H. Wang, “Past, present and future prospective of global carbon fibre composite developments and applications,” *Compos. B Eng.*, vol. 250, p. 110463, Feb. 2023, doi: 10.1016/J.COMPOSITESB.2022.110463.

[9] P. Zhuo, S. Li, I. A. Ashcroft, and A. I. Jones, “Material extrusion additive manufacturing of continuous fibre reinforced polymer matrix composites: A review and outlook,” *Compos. B Eng.*, vol. 224, p. 109143, Nov. 2021, doi: 10.1016/J.COMPOSITESB.2021.109143.

[10] N. van de Werken, H. Tekinalp, P. Khanbolouki, S. Ozcan, A. Williams, and M. Tehrani, “Additively manufactured carbon fiber-reinforced composites: State of the art and perspective,” *Addit. Manuf.*, vol. 31, p. 100962, Jan. 2020, doi: 10.1016/J.ADDMA.2019.100962.

[11] B. Karaş, P. J. Smith, J. P. A. Fairclough, and K. Mumtaz, “Additive manufacturing of high density carbon fibre reinforced polymer composites,” *Addit. Manuf.*, vol. 58, p. 103044, Oct. 2022, doi: 10.1016/J.ADDMA.2022.103044.

[12] S. Adil and I. Lazoglu, “A review on additive manufacturing of carbon fiber-reinforced polymers: Current methods, materials, mechanical properties, applications and challenges,” *J. Appl. Polym. Sci.*, vol. 140, no. 7, p. e53476, Feb. 2023, doi: 10.1002/APP.53476.

[13] B. Ergene, Y. E. İnci, B. Çetintaş, and B. Daysal, “An experimental study on the wear performance of 3D printed polylactic acid and carbon fiber reinforced polylactic acid parts: Effect of infill rate and water absorption time,” *Polym. Compos.*, vol. 46, no. 1, pp. 372–386, Jan. 2025, doi: 10.1002/PC.28993.

[14] A. R. Zanjanijam, I. Major, J. G. Lyons, U. Lafont, and D. M. Devine, “Fused Filament Fabrication of PEEK: A Review of Process-Structure-Property Relationships,” *Polymers 2020, Vol. 12,* vol. 12, no. 8, Jul. 2020, doi: 10.3390/POLYM12081665.

[15] P. Kothavade, A. Kafi, K. Shanmuganathan, and S. Bateman, “High performance polyimides for additive manufacturing: A critical review,” *Prog. Polym. Sci.*, vol. 172, p. 102055, Jan. 2026, doi: 10.1016/J.PROGPOLYMSCI.2025.102055.

[16] M. Tafaoli-Masoule, M. Shakeri, S. A. Zahedi, and M. Vaezi, “Experimental investigation of process parameters in polyether ether ketone 3D printing,” *Proceedings of the Institution of Mechanical Engineers, Part E: Journal of Process Mechanical Engineering*, vol. 238, no. 1, pp. 267–279, Feb. 2024, doi: 10.1177/09544089221141554/ASSET/58938F69-4388-4A9F-ACD4-3482D7ED5F36/ASSETS/IMAGES/LARGE/10.1177_09544089221141554-FIG10.JPG.

[17] P. Wang, B. Zou, H. Xiao, S. Ding, and C. Huang, “Effects of printing parameters of fused deposition modeling on mechanical properties, surface quality, and microstructure of PEEK,” *J. Mater. Process. Technol.*, vol. 271, pp. 62–74, Sep. 2019, doi: 10.1016/J.JMATPROTEC.2019.03.016.

[18] S. Dallal, B. Eslami, and S. Tiari, “Recent Advances in PEEK for Biomedical Applications: A Comprehensive Review of Material Properties, Processing, and Additive Manufacturing,” *Polymers 2025, Vol. 17,* vol. 17, no. 14, Jul. 2025, doi: 10.3390/POLYM17141968.

[19] “4 Polymer-based nanocomposites,” 2021, doi: 10.1016/B978-0-12-821290-5.00009-5.

[20] I. V. Panayotov, V. Orti, F. Cuisinier, and J. Yachouh, “Polyetheretherketone (PEEK) for medical applications,” *J. Mater. Sci. Mater. Med.*, vol. 27, no. 7, Jul. 2016, doi: 10.1007/S10856-016-5731-4.

[21] “High-Temperature Polymers”, doi: 10.1016/B978-0-8155-1585-2.50012-1.

[22] G. Velu Kaliyannan, R. Gunasekaran, R. Rathanasamy, S. Kandasamy, and S. Sivaraj, “Polymer composites: types, processes, properties, and applications,” *Finite Element Analysis of Polymers and Composites*, pp. 19–39, Jan. 2024, doi: 10.1016/B978-0-443-14087-7.00002-1.

[23] T. Tariverdian, T. Navaei, P. B. Milan, A. Samadikuchaksaraei, and M. Mozafari, “Functionalized polymers for tissue engineering and regenerative medicines,” 2019, doi: 10.1016/B978-0-12-816349-8.00016-3.

[24] S. M. Kurtz and J. N. Devine, “PEEK biomaterials in trauma, orthopedic, and spinal implants,” *Biomaterials*, vol. 28, no. 32, pp. 4845–4869, Nov. 2007, doi: 10.1016/J.BIOMATERIALS.2007.07.013.

[25] P. P. Chu, C. S. Wu, P. C. Liu, T. H. Wang, and J. P. Pan, “Proton exchange membrane bearing entangled structure: Sulfonated poly(ether ether ketone)/bismaleimide hyperbranch,” *Polymer (Guildf).*, vol. 51, no. 6, pp. 1386–1394, Mar. 2010, doi: 10.1016/J.POLYMER.2010.01.042.

[26] Y. Li, Z. Wang, X. Cui, X. Han, and J. Zhang, “Tribological Properties of PEEK and Its Composite Material under Oil Lubrication,” *Lubricants 2024, Vol. 12, Page 264*, vol. 12, no. 8, p. 264, Jul. 2024, doi: 10.3390/LUBRICANTS12080264.

[27] “2 High Temperature/High Performance Polymers”, doi: 10.1016/B978-1-4557-2551-9.00012-8.

[28] K. U. K. Reddy, S. K. R. Narala, P. C. Verma, P. J. Babu, and P. Saravanan, “A Comprehensive Study on the Tribological Behavior of Extruded and 3D-Printed PEEK for Low-Cost Dental Implant Solutions Under Simulated Oral Conditions,” *Tribol. Lett.*, vol. 73, no. 2, pp. 67-, Jun. 2025, doi: 10.1007/S11249-025-02001-3/METRICS.

[29] Z. Jin, X. Zhang, Z. Hou, Z. Yao, and H. Shen, “Tribological Properties of Carbon Fiber-Reinforced PEEK against 304 Stainless Steel with Reticulate Surface Texture,” *Materials*, vol. 15, no. 24, p. 8789, Dec. 2022, doi: 10.3390/MA15248789.

[30] C. Feng *et al.*, “Tribological properties of PEEK composites reinforced by MoS2 modified carbon fiber and nano SiO2,” *Tribol. Int.*, vol. 181, p. 108315, Mar. 2023, doi: 10.1016/J.TRIBOINT.2023.108315.

[31] B. Sariyev *et al.*, “Thermal, hardness, and tribological assessment of PEEK/CoCr composites,” *Scientific Reports 2025 15:1*, vol. 15, no. 1, pp. 1–15, Aug. 2025, doi: 10.1038/s41598-025-14776-5.

[32] X. Lv, X. Pei, S. Yang, Y. Zhang, Q. Wang, and T. Wang, “Tribological behavior of PEEK based composites with alternating layered structure fabricated via fused deposition modeling,” *Tribol. Int.*, vol. 199, p. 109953, Nov. 2024, doi: 10.1016/J.TRIBOINT.2024.109953.

[33] M. L. Shofner, K. Lozano, F. J. Rodríguez-Macías, and E. V. Barrera, “Nanofiber-reinforced polymers prepared by fused deposition modeling,” *J. Appl. Polym. Sci.*, vol. 89, no. 11, pp. 3081–3090, Sep. 2003, doi: 10.1002/APP.12496.

[34] W. Seok, E. Jeon, and Y. Kim, “Effects of Annealing for Strength Enhancement of FDM 3D-Printed ABS Reinforced with Recycled Carbon Fiber,” *Polymers 2023, Vol. 15, Page 3110*, vol. 15, no. 14, p. 3110, Jul. 2023, doi: 10.3390/POLYM15143110.

[35] A. M. Ralls, P. Kumar, and P. L. Menezes, “Tribological properties of additive manufactured materials for energy applications: A review,” *Processes*, vol. 9, no. 1, pp. 1–33, 2021, doi: 10.3390/PR9010031.

[36] H. Zhang *et al.*, “Effect of Annealing on Structure and Mechanical Properties of 3D-Printed Polymer Composites,” *Polym. Compos.*, 2025, doi: 10.1002/PC.70286.

[37] G. Kumar and A. Malas, “Control of friction induced oscillation by displacement feedback with a second order filter,” *J. Sound Vib.*, vol. 578, p. 118345, May 2024, doi: 10.1016/J.JSV.2024.118345.

[38] J. J. Sinou and B. Chomette, “Active vibration control and stability analysis of a time-delay system subjected to friction-induced vibration,” *J. Sound Vib.*, vol. 500, p. 116013, May 2021, doi: 10.1016/J.JSV.2021.116013.

[39] S. Chatterjee, “On the Design Criteria of Dynamic Vibration Absorbers for Controlling Friction-Induced Oscillations,” *Journal of Vibration and Control*, vol. 14, no. 3, pp. 397–415, Mar. 2008, doi: 10.1177/1077546307080030.

[40] J. Nath and S. Chatterjee, “Tangential acceleration feedback control of friction induced vibration,” *J. Sound Vib.*, vol. 377, pp. 22–37, Sep. 2016, doi: 10.1016/J.JSV.2016.05.020.

[41] J. Das and A. K. Mallik, “Control of friction driven oscillation by time-delayed state feedback,” *J. Sound Vib.*, vol. 297, no. 3–5, pp. 578–594, Nov. 2006, doi: 10.1016/J.JSV.2006.04.013.

[42] B. Chomette and J. J. Sinou, “On the Use of Linear and Nonlinear Controls for Mechanical Systems Subjected to Friction-Induced Vibration,” *Applied Sciences 2020, Vol. 10, Page 2085*, vol. 10, no. 6, p. 2085, Mar. 2020, doi: 10.3390/APP10062085.

[43] L. Chow *et al.*, “3D Printing Auxetic Architectures for Hypertrophic Scar Therapy,” *Macromol. Mater. Eng.*, vol. 307, no. 5, May 2022, doi: 10.1002/MAME.202100866.

[44] J. J. Andrew, H. Alhashmi, A. Schiffer, S. Kumar, and V. S. Deshpande, “Energy absorption and self-sensing performance of 3D printed CF/PEEK cellular composites”, doi: 10.1016/j.matdes.2021.109863.

[45] F. Scarpa, P. Pastorino, A. Garelli, S. Patsias, and M. Ruzzene, “Auxetic compliant flexible PU foams: Static and dynamic properties,” *Phys. Status Solidi B Basic Res.*, vol. 242, no. 3, pp. 681–694, Mar. 2005, doi: 10.1002/PSSB.200460386.

[46] A. Bezazi and F. Scarpa, “Tensile fatigue of conventional and negative Poisson’s ratio open cell PU foams,” *Int. J. Fatigue*, vol. 31, no. 3, pp. 488–494, Mar. 2009, doi: 10.1016/J.IJFATIGUE.2008.05.005.

[47] X. Gao, J. Wei, J. Huo, Z. Wan, and Y. Li, “The Vibration Isolation Design of a Re-Entrant Negative Poisson’s Ratio Metamaterial,” *Applied Sciences 2023, Vol. 13, Page 9442*, vol. 13, no. 16, p. 9442, Aug. 2023, doi: 10.3390/APP13169442.

[48] J. Meng, Z. Deng, K. Zhang, X. Xu, and F. Wen, “Band gap analysis of star-shaped honeycombs with varied Poisson’s ratio,” *Smart Mater. Struct.*, vol. 24, no. 9, p. 095011, Aug. 2015, doi: 10.1088/0964-1726/24/9/095011.

[49] Z. Wu, F. Li, and C. Zhang, “Band-gap analysis of a novel lattice with a hierarchical periodicity using the spectral element method,” *J. Sound Vib.*, vol. 421, pp. 246–260, May 2018, doi: 10.1016/J.JSV.2018.02.009.

[50] H. Liu, F. Ren, K. Liu, and X. Li, “Multiple Re-Entrant Star-Shaped Honeycomb with Double Negative Parameters and Bandgap Properties,” *Phys. Status Solidi B Basic Res.*, vol. 259, no. 12, Dec. 2022, doi: 10.1002/PSSB.202200277.

[51] M. Periyasamy and N. Srinivasan, “A review on auxetic structures: Applications, properties, classifications, finite element analysis, manufacturing methods, and selective laser melting process parameters,” *Results in Engineering*, vol. 28, p. 107660, Dec. 2025, doi: 10.1016/J.RINENG.2025.107660.

[52] Z. Chen, X. Wu, Y. M. Xie, Z. Wang, and S. Zhou, “Re-entrant auxetic lattices with enhanced stiffness: A numerical study,” *Int. J. Mech. Sci.*, vol. 178, p. 105619, Jul. 2020, doi: 10.1016/J.IJMECSCI.2020.105619.

[53] A. P. Garland *et al.*, “Coulombic friction in metamaterials to dissipate mechanical energy,” *Extreme Mech. Lett.*, vol. 40, p. 100847, Oct. 2020, doi: 10.1016/J.EML.2020.100847.

[54] M. Smith, Z. Guan, and W. J. Cantwell, “Finite element modelling of the compressive response of lattice structures manufactured using the selective laser melting technique,” 2012, doi: 10.1016/j.ijmecsci.2012.12.004.

[55] N. Jin, F. Wang, Y. Wang, B. Zhang, H. Cheng, and H. Zhang, “Failure and energy absorption characteristics of four lattice structures under dynamic loading-NC-ND license (http:// creativecommons.org/licenses/by-nc-nd/4.0/),” 2019, doi: 10.1016/j.matdes.2019.107655.

[56] K. Wei, Q. Yang, B. Ling, H. Xie, Z. Qu, and D. Fang, “Mechanical responses of titanium 3D kagome lattice structure manufactured by selective laser melting,” *Extreme Mech. Lett.*, vol. 23, pp. 41–48, 2018, doi: 10.1016/j.eml.2018.07.001.

[57] X. Wan *et al.*, “Recent Advances in 4D Printing of Advanced Materials and Structures for Functional Applications,” *Advanced Materials*, vol. 36, no. 34, p. 2312263, Aug. 2024, doi: 10.1002/ADMA.202312263.

[58] K. Kanishka and B. Acherjee, “Revolutionizing manufacturing: A comprehensive overview of additive manufacturing processes, materials, developments, and challenges,” *J. Manuf. Process.*, vol. 107, pp. 574–619, Dec. 2023, doi: 10.1016/J.JMAPRO.2023.10.024.

[59] H. Chen, Y. Liu, Y. Wang, Z. Li, D. Wang, and K. Kosiba, “Temperature-dependent dynamic compressive properties and failure mechanisms of the additively manufactured CoCrFeMnNi high entropy alloy,” *Mater. Des.*, vol. 224, p. 111324, Dec. 2022, doi: 10.1016/J.MATDES.2022.111324.

[60] T. Wen, R. Fu, S. Xiao, L. Zhang, B. Song, and H. Lei, “Temperature-dependent performance and constitutive modeling of additively manufactured Ti600 alloy,” *Journal of Materials Research and Technology*, vol. 34, pp. 776–784, Jan. 2025, doi: 10.1016/J.JMRT.2024.12.100.

[61] J. Joshy and B. Kuriachen, “Investigations in to the wear behavior of additively manufactured Ti6Al4V at elevated temperatures,” *Wear*, vol. 571, p. 205774, Jun. 2025, doi: 10.1016/J.WEAR.2025.205774.

[62] M. Tripathy, K. Gaskell, J. Laureto, K. Davami, and A. Beheshti, “Elevated temperature fretting wear study of additively manufactured inconel 625 superalloy,” *Addit. Manuf.*, vol. 67, p. 103492, Apr. 2023, doi: 10.1016/J.ADDMA.2023.103492.

[63] A. Kurdi, W. H. Kan, and L. Chang, “Tribological behaviour of high performance polymers and polymer composites at elevated temperature,” *Tribol. Int.*, vol. 130, pp. 94–105, Feb. 2019, doi: 10.1016/J.TRIBOINT.2018.09.010.

[64] X. Li, R. Zhang, W. S. T. Hung, U. Olofsson, L. Manuel, and C. Duan, “The influence of temperature on the tribological properties of polyoxymethylene (POM) materials,” *Proceedings of the Institution of Mechanical Engineers, Part J: Journal of Engineering Tribology*, vol. 239, no. 4, pp. 410–422, Apr. 2025, doi: 10.1177/13506501241292506.

[65] A. Nazir *et al.*, “Multi-material additive manufacturing: A systematic review of design, properties, applications, challenges, and 3D printing of materials and cellular metamaterials,” *Mater. Des.*, vol. 226, p. 111661, Feb. 2023, doi: 10.1016/J.MATDES.2023.111661.

[66] P. Parandoush and D. Lin, “A review on additive manufacturing of polymer-fiber composites,” *Compos. Struct.*, vol. 182, pp. 36–53, Dec. 2017, doi: 10.1016/J.COMPSTRUCT.2017.08.088.

[67] L. J. Tan, W. Zhu, and K. Zhou, “Recent Progress on Polymer Materials for Additive Manufacturing,” *Adv. Funct. Mater.*, vol. 30, no. 43, p. 2003062, Oct. 2020, doi: 10.1002/ADFM.202003062.

[68] A. Mostafaei *et al.*, “Binder jet 3D printing—Process parameters, materials, properties, modeling, and challenges,” *Prog. Mater. Sci.*, vol. 119, p. 100707, Jun. 2021, doi: 10.1016/J.PMATSCI.2020.100707.

[69] D. Chekkaramkodi, L. Jacob, M. S. C, R. Umer, and H. Butt, “Review of vat photopolymerization 3D printing of photonic devices,” *Addit. Manuf.*, vol. 86, p. 104189, Apr. 2024, doi: 10.1016/J.ADDMA.2024.104189.

[70] I. Gibson, D. Rosen, and B. Stucker, “Powder Bed Fusion Processes,” *Additive Manufacturing Technologies*, pp. 107–145, 2015, doi: 10.1007/978-1-4939-2113-3_5.

[71] S. Kumar *et al.*, “Powder bed fusion 3D printing for drug delivery and healthcare applications,” *Annals of 3D Printed Medicine*, vol. 18, p. 100200, May 2025, doi: 10.1016/J.STLM.2025.100200.

[72] N. D. Dejene and H. G. Lemu, “Current Status and Challenges of Powder Bed Fusion-Based Metal Additive Manufacturing: Literature Review,” *Metals 2023, Vol. 13,* vol. 13, no. 2, Feb. 2023, doi: 10.3390/MET13020424.

[73] O. Gülcan, K. Günaydın, and A. Tamer, “The State of the Art of Material Jetting—A Critical Review,” *Polymers 2021, Vol. 13,* vol. 13, no. 16, Aug. 2021, doi: 10.3390/POLYM13162829.

[74] P.-A. Högström, S. Karlsson, and U. W. Gedde, “Effect of Aging on the Mechanical Properties of UV Curable Optical Fiber Coatings,” *International Journal of Polymeric Materials and Polymeric Biomaterials*, vol. 46, no. 3–4, pp. 403–421, 2000, doi: 10.1080/00914030008033884.

[75] A. Elkaseer, K. J. Chen, J. C. Janhsen, O. Refle, V. Hagenmeyer, and S. G. Scholz, “Material jetting for advanced applications: A state-of-the-art review, gaps and future directions,” *Addit. Manuf.*, vol. 60, p. 103270, Dec. 2022, doi: 10.1016/J.ADDMA.2022.103270.

[76] T. Ma *et al.*, “Advances in 3D printing for polymer composites: A review,” *InfoMat*, vol. 6, no. 6, p. e12568, Jun. 2024, doi: 10.1002/INF2.12568.

[77] J. Marzi *et al.*, “Non-Invasive Three-Dimensional Cell Analysis in Bioinks by Raman Imaging,” *ACS Appl. Mater. Interfaces*, vol. 14, no. 27, pp. 30455–30465, Jul. 2022, doi: 10.1021/ACSAMI.1C24463/ASSET/IMAGES/LARGE/AM1C24463_0008.JPEG.

[78] C. Parulski, O. Jennotte, A. Lechanteur, and B. Evrard, “Challenges of fused deposition modeling 3D printing in pharmaceutical applications: Where are we now?,” *Adv. Drug Deliv. Rev.*, vol. 175, p. 113810, Aug. 2021, doi: 10.1016/J.ADDR.2021.05.020.

[79] M. Baechle-Clayton, E. Loos, M. Taheri, and H. Taheri, “Failures and Flaws in Fused Deposition Modeling (FDM) Additively Manufactured Polymers and Composites,”

Journal of Composites Science 2022, Vol. 6, Page 202, vol. 6, no. 7, p. 202, Jul. 2022, doi: 10.3390/JCS6070202.

[80] S. Dev and R. Srivastava, "Experimental investigation and optimization of FDM process parameters for material and mechanical strength," *Mater. Today Proc.*, vol. 26, pp. 1995–1999, Jan. 2020, doi: 10.1016/J.MATPR.2020.02.435.

[81] D. Popescu, A. Zapciu, C. Amza, F. Baciu, and R. Marinescu, "Material Properties FDM process parameters influence over the mechanical properties of polymer specimens: A review," 2018, doi: 10.1016/j.polymertesting.2018.05.020.

[82] K. Wang, H. Long, Y. Chen, M. Baniassadi, Y. Rao, and Y. Peng, "Heat-treatment effects on dimensional stability and mechanical properties of 3D printed continuous carbon fiber-reinforced composites," *Compos. Part A Appl. Sci. Manuf.*, vol. 147, p. 106460, Aug. 2021, doi: 10.1016/J.COMPOSITESA.2021.106460.

[83] A. Boschetto and L. Bottini, "Design for manufacturing of surfaces to improve accuracy in Fused Deposition Modeling," *Robot. Comput. Integr. Manuf.*, vol. 37, pp. 103–114, Feb. 2016, doi: 10.1016/J.RCIM.2015.07.005.

[84] S. H. Siddique, P. J. Hazell, H. Wang, J. P. Escobedo, and A. A. H. Ameri, "Lessons from nature: 3D printed bio-inspired porous structures for impact energy absorption – A review," *Addit. Manuf.*, vol. 58, p. 103051, Oct. 2022, doi: 10.1016/J.ADDMA.2022.103051.

[85] S. Zhang *et al.*, "3D printing thermoplastic polyurethane hierarchical cellular foam with outstanding energy absorption capability," *Addit. Manuf.*, vol. 76, p. 103770, Aug. 2023, doi: 10.1016/J.ADDMA.2023.103770.

[86] X. Wang *et al.*, "Research progress in polylactic acid processing for 3D printing," *J. Manuf. Process.*, vol. 112, pp. 161–178, Feb. 2024, doi: 10.1016/J.JMAPRO.2024.01.038.

[87] I. Plamadiala, C. Croitoru, M. A. Pop, and I. C. Roata, "Enhancing Polylactic Acid (PLA) Performance: A Review of Additives in Fused Deposition Modelling (FDM) Filaments," *Polymers 2025, Vol. 17, Page 191*, vol. 17, no. 2, p. 191, Jan. 2025, doi: 10.3390/POLYM17020191.

[88] W. X. Ou, Y. Weng, J. B. Zeng, and Y. D. Li, "Fully biobased poly(lactic acid)/lignin composites compatibilized by epoxidized natural rubber," *Int. J. Biol. Macromol.*, vol. 236, p. 123960, May 2023, doi: 10.1016/J.IJBIOMAC.2023.123960.

[89] W. Wang *et al.*, "Development of bio-based PLA/cellulose antibacterial packaging and its application for the storage of shiitake mushroom," *Food Chem.*, vol. 429, p. 136905, Dec. 2023, doi: 10.1016/J.FOODCHEM.2023.136905.

[90] H. Kaczmarek, M. Nowicki, I. Vuković-Kwiatkowska, and S. Nowakowska, "Crosslinked blends of poly(lactic acid) and polyacrylates: AFM, DSC and XRD

studies," *Journal of Polymer Research*, vol. 20, no. 3, pp. 91-, Mar. 2013, doi: 10.1007/S10965-013-0091-Y/FIGURES/9.

[91] M. Khamvongsa, K. Milton, and T. R. Faisal, "Mechanical characterization of low-cost 3D FDM printed scaffolds fabricated with synthesized PLA/HA bio-composite filament," *Annals of 3D Printed Medicine*, vol. 18, p. 100194, May 2025, doi: 10.1016/J.STLM.2025.100194.

[92] A. Wang, J. Venezuela, and M. S. Dargusch, "Enhancing the corrodibility of biodegradable iron and zinc using poly(lactic) acid (PLA) coating for temporary medical implant applications," *Prog. Org. Coat.*, vol. 174, p. 107301, Jan. 2023, doi: 10.1016/J.PORGCOAT.2022.107301.

[93] L. Yang, X. Liu, Y. Xiao, B. Liu, Z. Xue, and Y. Wang, "Additive manufacturing of carbon nanotube/polylactic acid films with efficient electromagnetic interference shielding and electrical heating performance via fused deposition modeling," *Synth. Met.*, vol. 293, p. 117258, Mar. 2023, doi: 10.1016/J.SYNTHMET.2022.117258.

[94] V. DeStefano, S. Khan, and A. Tabada, "Applications of PLA in modern medicine," *Engineered Regeneration*, vol. 1, pp. 76–87, Jan. 2020, doi: 10.1016/J.ENGREG.2020.08.002.

[95] S. A. Raj, E. Muthukumaran, and K. Jayakrishna, "A Case Study of 3D Printed PLA and Its Mechanical Properties," *Mater. Today Proc.*, vol. 5, no. 5, pp. 11219–11226, Jan. 2018, doi: 10.1016/J.MATPR.2018.01.146.

[96] M. Olam and N. Tosun, "Assessment of 3D Printings Produced in Fused Deposition Modeling Printer Using Polylactic Acid/TiO2/Hydroxyapatite Composite Filaments," *J. Mater. Eng. Perform.*, vol. 31, no. 6, pp. 4554–4565, Jun. 2022, doi: 10.1007/S11665-021-06539-W/METRICS.

[97] S. L. Rodríguez-Reyna, J. H. Díaz-Aguilera, H. R. Acevedo-Parra, V. Escobar-Barrios, and F. Tapia, "Optimization of the mechanical behavior of ABS and PLA 3D printed using heat treatments," *MRS Adv.*, vol. 10, no. 6, pp. 780–788, Mar. 2025, doi: 10.1557/S43580-025-01236-5/METRICS.

[98] E. Taşcıoğlu, Ö. Kıtay, A. Ö. Keskin, and Y. Kaynak, "Effect of printing parameters and post-process on surface roughness and dimensional deviation of PLA parts fabricated by extrusion-based 3D printing," *Journal of the Brazilian Society of Mechanical Sciences and Engineering*, vol. 44, no. 4, Apr. 2022, doi: 10.1007/S40430-022-03429-7.

[99] Y. Tao, P. Li, J. Zhang, S. Wang, S. Q. Shi, and F. Kong, "A review of fused filament fabrication of continuous natural fiber reinforced thermoplastic composites: Techniques and materials," *Polym. Compos.*, vol. 44, no. 12, pp. 8200–8222, Dec. 2023, doi: 10.1002/PC.27477.

[100] R. A. Ilyas *et al.*, “Polylactic Acid (PLA) Biocomposite: Processing, Additive Manufacturing and Advanced Applications,” *Polymers 2021, Vol. 13, Page 1326*, vol. 13, no. 8, p. 1326, Apr. 2021, doi: 10.3390/POLYM13081326.

[101] K. tak Lau, P. yan Hung, M. H. Zhu, and D. Hui, “Properties of natural fibre composites for structural engineering applications,” *Compos. B Eng.*, vol. 136, pp. 222–233, Mar. 2018, doi: 10.1016/J.COMPOSITESB.2017.10.038.

[102] S. S. Yao, F. L. Jin, K. Y. Rhee, D. Hui, and S. J. Park, “Recent advances in carbon-fiber-reinforced thermoplastic composites: A review,” *Compos. B Eng.*, vol. 142, pp. 241–250, Jun. 2018, doi: 10.1016/J.COMPOSITESB.2017.12.007.

[103] H. Zhang *et al.*, “3D printing of continuous carbon fibre reinforced polymer composites with optimised structural topology and fibre orientation,” *Compos. Struct.*, vol. 313, p. 116914, Jun. 2023, doi: 10.1016/J.COMPSTRUCT.2023.116914.

[104] J. Lu, Y. Zhang, L. Duan, Y. Huo, and H. Liu, “Dynamic behavior of CFRP strengthen RC beams based on digital image correlation technology,” *Eng. Fract. Mech.*, vol. 271, p. 108597, Aug. 2022, doi: 10.1016/J.ENGFRACMECH.2022.108597.

[105] R. Harnden, D. Carlstedt, D. Zenkert, and G. Lindbergh, “Multifunctional Carbon Fiber Composites: A Structural, Energy Harvesting, Strain-Sensing Material,” *ACS Appl. Mater. Interfaces*, vol. 14, no. 29, pp. 33871–33880, 2022, doi: 10.1021/ACSAMI.2C08375/ASSET/IMAGES/LARGE/AM2C08375_0006.JPEG.

[106] M. Heidari-Rarani, M. Rafiee-Afarani, and A. M. Zahedi, “Mechanical characterization of FDM 3D printing of continuous carbon fiber reinforced PLA composites,” *Compos. B Eng.*, vol. 175, p. 107147, Oct. 2019, doi: 10.1016/J.COMPOSITESB.2019.107147.

[107] Z. Man, H. Wang, Q. He, D. E. Kim, and L. Chang, “Friction and wear behaviour of additively manufactured continuous carbon fibre reinforced PA6 composites,” *Compos. B Eng.*, vol. 226, p. 109332, Dec. 2021, doi: 10.1016/J.COMPOSITESB.2021.109332.

[108] L. Lin, N. Ecke, M. Huang, X. Q. Pei, and A. K. Schlarb, “Impact of nanosilica on the friction and wear of a PEEK/CF composite coating manufactured by fused deposition modeling (FDM),” *Compos. B Eng.*, vol. 177, p. 107428, Nov. 2019, doi: 10.1016/J.COMPOSITESB.2019.107428.

[109] Y. Deng, Y. Zhao, B. Wan, and L. Chang, “Effects of re-entrant auxetic structure on friction-induced vibrational behaviour of 3D printed PLA in sliding wear process,” *Friction*, Aug. 2025, doi: 10.26599/FRICT.2025.9441172.

[110] Z. Weng, J. Wang, T. Senthil, and L. Wu, “Mechanical and thermal properties of ABS/montmorillonite nanocomposites for fused deposition modeling 3D printing,” 2016, doi: 10.1016/j.matdes.2016.04.045.

[111] M. Etchegaray-Bello *et al.*, “Experimental thermal runaway degradation and residual performance of fiber-reinforced PEEK and PPS composites for battery enclosure applications,” *Eng. Fail. Anal.*, vol. 185, p. 110430, Mar. 2026, doi: 10.1016/J.ENGFAILANAL.2025.110430.

[112] A. Rosa-Sainz, M. L. García-Romeu, I. Ferrer, M. B. Silva, and G. Centeno, “On the effective peek application for customized cranio-maxillofacial prostheses: An experimental formability analysis,” *J. Manuf. Process.*, vol. 86, pp. 66–84, Jan. 2023, doi: 10.1016/J.JMAPRO.2022.12.044.

[113] Q. Feng, W. Maier, and H. C. Möhring, “Application of machine learning to optimize process parameters in fused deposition modeling of PEEK material,” *Procedia CIRP*, vol. 107, pp. 1–8, Jan. 2022, doi: 10.1016/J.PROCIR.2022.04.001.

[114] M. Adamson and B. Eslami, “Post-Processing PEEK 3D-Printed Parts: Experimental Investigation of Annealing on Microscale and Macroscale Properties,” *Polymers (Basel).*, vol. 17, no. 6, p. 744, Mar. 2025, doi: 10.3390/POLYM17060744.

[115] P. Sikder, “A comprehensive review on the State of the Art in the research and development of poly-ether-ether-ketone (PEEK) biomaterial-based implants,” *Acta Biomater.*, vol. 191, pp. 29–52, Jan. 2025, doi: 10.1016/J.ACTBIO.2024.11.033.

[116] M. Thiruchitrambalam, D. Bubesh Kumar, D. Shanmugam, and M. Jawaid, “A review on PEEK composites – Manufacturing methods, properties and applications,” *Mater. Today Proc.*, vol. 33, pp. 1085–1092, Jan. 2020, doi: 10.1016/J.MATPR.2020.07.124.

[117] S. S. Abhay *et al.*, “Wear Resistance, Color Stability and Displacement Resistance of Milled PEEK Crowns Compared to Zirconia Crowns under Stimulated Chewing and High-Performance Aging,” *Polymers 2021, Vol. 13, Page 3761*, vol. 13, no. 21, p. 3761, Oct. 2021, doi: 10.3390/POLYM13213761.

[118] M. Hintze, N. Eliasen, and I. Sivebaek, “Wear and friction of PEEK composites, dry or lubricated,” *Wear*, vol. 534–535, p. 205135, Dec. 2023, doi: 10.1016/J.WEAR.2023.205135.

[119] M. Buciumeanu *et al.*, “Ti6Al4V cellular structures impregnated with biomedical PEEK - New material design for improved tribological behavior,” *Tribol. Int.*, vol. 119, pp. 157–164, Mar. 2018, doi: 10.1016/J.TRIBOINT.2017.10.038.

[120] A. Kantaros, T. Ganetsos, F. I. T. Petrescu, L. M. Ungureanu, and I. S. Munteanu, “Post-Production Finishing Processes Utilized in 3D Printing Technologies,” *Processes 2024, Vol. 12,* vol. 12, no. 3, Mar. 2024, doi: 10.3390/PR12030595.

[121] S. Dev and R. Srivastava, “Experimental investigation and optimization of FDM process parameters for material and mechanical strength,” *Mater. Today Proc.*, vol. 26, pp. 1995–1999, Jan. 2020, doi: 10.1016/J.MATPR.2020.02.435.

[122] B. Li, J. Yang, H. Gu, J. Jiang, J. Zhang, and J. Sun, “Surface roughness of PLA parts by FDM with chemical treatment,” *J. Phys. Conf. Ser.*, vol. 1948, no. 1, p. 012199, Jun. 2021, doi: 10.1088/1742-6596/1948/1/012199.

[123] A. Pricci and G. Percoco, “Towards a digital twin of extrusion-based additive manufacturing: an experimentally validated numerical model of ironing process,” *Progress in Additive Manufacturing*, vol. 10, no. 9, pp. 6491–6506, Sep. 2025, doi: 10.1007/S40964-025-00988-8/TABLES/7.

[124] M. Moradi, M. K. Moghadam, M. Shamsborhan, M. Bodaghi, and H. Falavandi, “Post-Processing of FDM 3D-Printed Polylactic Acid Parts by Laser Beam Cutting,” *Polymers 2020, Vol. 12,* vol. 12, no. 3, Mar. 2020, doi: 10.3390/POLYM12030550.

[125] E. Maleki, S. Bagherifard, M. Bandini, and M. Guagliano, “Surface post-treatments for metal additive manufacturing: Progress, challenges, and opportunities,” *Addit. Manuf.*, vol. 37, p. 101619, Jan. 2021, doi: 10.1016/J.ADDMA.2020.101619.

[126] A. Shrivastava, S. Anand Kumar, B. K. Nagesha, and T. N. Suresh, “Electropolishing of Inconel 718 manufactured by laser powder bed fusion: Effect of heat treatment on hardness, 3D surface topography and material ratio curve,” *Opt. Laser Technol.*, vol. 144, p. 107448, Dec. 2021, doi: 10.1016/J.OPTLASTEC.2021.107448.

[127] E. M. Beamud-González, P. J. Núñez-López, and E. García-Plaza, “Electropolishing Stainless Steel Optimization Using Surface Quality, Dimensional Accuracy, and Electrical Consumption Criteria,” *Materials 2023, Vol. 16,* vol. 16, no. 5, Feb. 2023, doi: 10.3390/MA16051770.

[128] W. Han and F. Fang, “Fundamental aspects and recent developments in electropolishing,” *Int. J. Mach. Tools Manuf.*, vol. 139, pp. 1–23, Apr. 2019, doi: 10.1016/J.IJMACHTOOLS.2019.01.001.

[129] K. L. Tan and S. H. Yeo, “Surface modification of additive manufactured components by ultrasonic cavitation abrasive finishing,” *Wear*, vol. 378–379, pp. 90–95, May 2017, doi: 10.1016/J.WEAR.2017.02.030.

[130] J. Wang, J. Wang, J. Wang, Q. Cui, and P. J. Liew, “Ultrasonic cavitation finishing of 316 L stainless steel using different abrasive particles: A combined SPH simulation and experimental study,” *Mater. Today Commun.*, vol. 42, p. 111168, Jan. 2025, doi: 10.1016/J.MTCOMM.2024.111168.

[131] M. Rezanejad, S. Rezanezhad, and M. Azadi, “Effect of 3D-printed PLA coating on the wear characteristics in AM60 magnesium alloy,” *Results in Engineering*, vol. 27, p. 106596, Sep. 2025, doi: 10.1016/J.RINENG.2025.106596.

[132] L. Chen *et al.*, “Enhancing mechanical properties and electrochemical behavior of equiatomic FeNiCoCr high-entropy alloy through sintering and hot isostatic pressing for binder jet 3D printing,” *Addit. Manuf.*, vol. 81, p. 103999, Feb. 2024, doi: 10.1016/J.ADDMA.2024.103999.

[133] M. Lopez *et al.*, “Effects of Postprocess Hot Isostatic Pressing Treatments on the Mechanical Performance of EBM Fabricated TI-6Al-2Sn-4Zr-2Mo,” *Materials 2020, Vol. 13,* vol. 13, no. 11, Jun. 2020, doi: 10.3390/MA13112604.

[134] Z. Xu, B. Zou, S. Ding, Y. Zhuang, and X. Wang, “Study on the hot isostatic pressing post-treatment of FDM-3D printed continuous carbon fiber reinforced composites,” *J. Manuf. Process.*, vol. 104, pp. 205–217, Oct. 2023, doi: 10.1016/J.JMAPRO.2023.08.060.

[135] G. Wang, D. Zhang, B. Li, G. Wan, G. Zhao, and A. Zhang, “Strong and thermal-resistance glass fiber-reinforced polylactic acid (PLA) composites enabled by heat treatment,” *Int. J. Biol. Macromol.*, vol. 129, pp. 448–459, May 2019, doi: 10.1016/J.IJBIOMAC.2019.02.020.

[136] C. Yang, X. Tian, D. Li, Y. Cao, F. Zhao, and C. Shi, “Influence of thermal processing conditions in 3D printing on the crystallinity and mechanical properties of PEEK material,” *J. Mater. Process. Technol.*, vol. 248, pp. 1–7, Oct. 2017, doi: 10.1016/J.JMATPROTEC.2017.04.027.

[137] J. Li, Y. Fu, W. Pi, Y. Li, and S. Fu, “Improving mechanical performances at room and elevated temperatures of 3D printed polyether-ether-ketone composites by combining optimal short carbon fiber content and annealing treatment,” *Compos. B Eng.*, vol. 267, p. 111067, Dec. 2023, doi: 10.1016/J.COMPOSITESB.2023.111067.

[138] A. El Magri, K. El Mabrouk, S. Vaudreuil, H. Chibane, and M. E. Touhami, “Optimization of printing parameters for improvement of mechanical and thermal performances of 3D printed poly(ether ether ketone) parts,” *J. Appl. Polym. Sci.*, vol. 137, no. 37, Oct. 2020, doi: 10.1002/APP.49087.

[139] C. Y. Liaw, J. W. Tolbert, L. W. Chow, and M. Guvendiren, “Interlayer bonding strength of 3D printed PEEK specimens,” *Soft Matter*, vol. 17, no. 18, pp. 4775–4789, May 2021, doi: 10.1039/D1SM00417D.

[140] T. König, E. Wolf, P. Daum, D. Kürten, A. Kailer, and M. Dienwiebel, “Influencing factors on high temperature tribology,” *Wear*, vol. 566–567, p. 205758, Apr. 2025, doi: 10.1016/J.WEAR.2025.205758.

[141] K. S. Kumar, R. Soundararajan, G. Shanthosh, P. Saravanakumar, and M. Ratteesh, “Augmenting effect of infill density and annealing on mechanical properties of PETG and CFPETG composites fabricated by FDM,” *Mater. Today Proc.*, vol. 45, pp. 2186–2191, Jan. 2021, doi: 10.1016/J.MATPR.2020.10.078.

[142] H. Zhen, B. Zhao, L. Quan, and J. Fu, “Effect of 3D Printing Process Parameters and Heat Treatment Conditions on the Mechanical Properties and Microstructure of PEEK Parts,” *Polymers (Basel).*, vol. 15, no. 9, p. 2209, May 2023, doi: 10.3390/POLYM15092209.

[143] J. Dong, C. Mei, J. Han, S. Lee, and Q. Wu, “3D printed poly(lactic acid) composites with grafted cellulose nanofibers: Effect of nanofiber and post-fabrication annealing treatment on composite flexural properties,” *Addit. Manuf.*, vol. 28, pp. 621–628, Aug. 2019, doi: 10.1016/J.ADDMA.2019.06.004.

[144] M. A. Islam *et al.*, “Additive manufacturing in polymer research: Advances, synthesis, and applications,” *Polym. Test.*, vol. 132, p. 108364, Mar. 2024, doi: 10.1016/J.POLYMERTESTING.2024.108364.

[145] Y. Tao, M. Ren, H. Zhang, and T. Peijs, “Recent progress in acoustic materials and noise control strategies – A review,” *Appl. Mater. Today*, vol. 24, p. 101141, Sep. 2021, doi: 10.1016/J.APMT.2021.101141.

[146] L. Yang, O. Harrysson, H. West, and D. Cormier, “Mechanical properties of 3D re-entrant honeycomb auxetic structures realized via additive manufacturing,” *Int. J. Solids Struct.*, vol. 69–70, pp. 475–490, Sep. 2015, doi: 10.1016/J.IJSOLSTR.2015.05.005.

[147] N. Namvar, A. Zolfagharian, F. Vakili-Tahami, and M. Bodaghi, “Reversible energy absorption of elasto-plastic auxetic, hexagonal, and AuxHex structures fabricated by FDM 4D printing,” 2022, doi: 10.1088/1361-665X/ac6291.

[148] W. Yan, X. Tian, D. Zhang, Y. Zhou, and Q. Wang, “3D Printing of Stretchable Strain Sensor Based on Continuous Fiber Reinforced Auxetic Structure,” *Chinese Journal of Mechanical Engineering: Additive Manufacturing Frontiers*, vol. 2, no. 2, p. 100073, Jun. 2023, doi: 10.1016/J.CJMEAM.2023.100073.

[149] Q. Gao, C. A. Tan, G. Hulbert, and L. Wang, “Geometrically nonlinear mechanical properties of auxetic double-V microstructures with negative Poisson’s ratio,” *Eur. J. Mech. A Solids*, vol. 80, p. 103933, 2020, doi: 10.1016/j.euromechsol.2019.103933.

[150] L. Zhang *et al.*, “3D direct printing of mechanical and biocompatible hydrogel meta-structures,” 2021, doi: 10.1016/j.bioactmat.2021.08.015.

[151] H. Ni, J. Liu, L. Guo, T. Zeng, and G. Pan, “A novel Star-4 honeycomb with the inclined ligaments for enhanced tunability of wave propagation behaviors,” *Compos. Struct.*, vol. 346, p. 118405, Oct. 2024, doi: 10.1016/J.COMPSTRUCT.2024.118405.

[152] A. Bezazi and F. Scarpa, “Mechanical behaviour of conventional and negative Poisson’s ratio thermoplastic polyurethane foams under compressive cyclic loading,” *Int. J. Fatigue*, vol. 29, no. 5, pp. 922–930, May 2007, doi: 10.1016/J.IJFATIGUE.2006.07.015.

[153] F. Scarpa, W. A. Bullough, and P. Lumley, “Trends in acoustic properties of iron particle seeded auxetic polyurethane foam,” *Proc. Inst. Mech. Eng. C J. Mech. Eng. Sci.*, vol. 218, no. 2, pp. 241–244, 2004, doi: 10.1243/095440604322887099.

[154] T. Wang, J. An, H. He, X. Wen, and X. Xi, “A novel 3D impact energy absorption structure with negative Poisson’s ratio and its application in aircraft crashworthiness,”

Compos. Struct., vol. 262, p. 113663, Apr. 2021, doi: 10.1016/J.COMPSTRUCT.2021.113663.

[155] P. Munyensanga and K. El Mabrouk, "Elemental and experimental analysis of modified stent's structure under uniaxial compression load," *J. Mech. Behav. Biomed. Mater.*, vol. 143, p. 105903, Jul. 2023, doi: 10.1016/J.JMBBM.2023.105903.

[156] B. R. Krishnan, A. N. Biswas, K. V. Ahalya Kumar, and P. S. Rama Sreekanth, "Auxetic structure metamaterial for crash safety of sports helmet," *Mater. Today Proc.*, vol. 56, pp. 1043–1049, Jan. 2022, doi: 10.1016/J.MATPR.2021.09.110.

[157] D. Qi, H. Yu, W. Hu, C. He, W. Wu, and Y. Ma, "Bandgap and wave attenuation mechanisms of innovative reentrant and anti-chiral hybrid auxetic metastructure," *Extreme Mech. Lett.*, vol. 28, pp. 58–68, Apr. 2019, doi: 10.1016/J.EML.2019.02.005.

[158] Z. Tao *et al.*, "A novel re-entrant honeycomb metamaterial with tunable bandgap," *Smart Mater. Struct.*, vol. 31, no. 9, p. 095024, Jul. 2022, doi: 10.1088/1361-665X/AC812B.

[159] K. Pan, W. Zhang, and J. Ding, "Negative Poisson's Ratio Re-Entrant Base Modeling and Vibration Isolation Performance Analysis," *Symmetry 2022, Vol. 14, Page 1356*, vol. 14, no. 7, p. 1356, Jun. 2022, doi: 10.3390/SYM14071356.

[160] H. Qin and D. Yang, "Vibration reduction design method of metamaterials with negative Poisson's ratio," *J. Mater. Sci.*, vol. 54, no. 22, pp. 14038–14054, Nov. 2019, doi: 10.1007/S10853-019-03903-Z/FIGURES/20.

[161] J. Bai, "Fiber-reinforced polymer types and properties," *Advanced Fibre-Reinforced Polymer (FRP) Composites for Structural Applications*, pp. 93–99, Jan. 2023, doi: 10.1016/B978-0-12-820346-0.00014-9.

[162] E. Askari, P. Flores, D. Dabirrahmani, and R. Appleyard, "Study of the friction-induced vibration and contact mechanics of artificial hip joints," *Tribol. Int.*, vol. 70, pp. 1–10, Feb. 2014, doi: 10.1016/J.TRIBOINT.2013.09.006.

[163] G. Zhou, P. Li, D. Liao, Y. Zhang, and P. Zhong, "The Friction-Induced Vibration of Water-Lubricated Rubber Bearings during the Shutdown Process," *Materials 2020, Vol. 13, Page 5818*, vol. 13, no. 24, p. 5818, Dec. 2020, doi: 10.3390/MA13245818.

[164] C. G. Lin, M. S. Zou, C. Sima, S. X. Liu, and L. W. Jiang, "Friction-induced vibration and noise of marine stern tube bearings considering perturbations of the stochastic rough surface," *Tribol. Int.*, vol. 131, pp. 661–671, Mar. 2019, doi: 10.1016/J.TRIBOINT.2018.11.026.

[165] R. Lakes, "Foam structures with a negative poisson's ratio," *Science (1979).*, vol. 235, no. 4792, pp. 1038–1040, 1987, doi: 10.1126/SCIENCE.235.4792.1038.

[166] H. J. O'Connor and D. P. Dowling, "Evaluation of the influence of low pressure additive manufacturing processing conditions on printed polymer parts," *Addit. Manuf.*, vol. 21, pp. 404–412, May 2018, doi: 10.1016/J.ADDMA.2018.04.007.

[167] Y. Hou and A. Panesar, "The moisture absorption of additively manufactured short carbon fibre reinforced polyamide," *Compos. Part A Appl. Sci. Manuf.*, vol. 188, p. 108528, Jan. 2025, doi: 10.1016/J.COMPOSITESA.2024.108528.

[168] A. Kaptan, "Investigation of the Effect of Exposure to Liquid Chemicals on the Strength Performance of 3D-Printed Parts from Different Filament Types," *Polymers (Basel).*, vol. 17, no. 12, p. 1637, Jun. 2025, doi: 10.3390/POLYM17121637.

[169] A. Das *et al.*, "Current understanding and challenges in high temperature additive manufacturing of engineering thermoplastic polymers," *Addit. Manuf.*, vol. 34, p. 101218, Aug. 2020, doi: 10.1016/J.ADDMA.2020.101218.

[170] A. Chandra Shekar, A. Hadj Djilani, R. Zitoune, L. Toubal, and L. A. Hof, "Effect of input variables on the mechanical properties of additively manufactured PEEK thermoplastics," *Mater. Today Proc.*, Sep. 2023, doi: 10.1016/J.MATPR.2023.09.101.

[171] T. A. Abualbandora, M. G. Alshneeqat, and A. H. I. Mourad, "Impact of 3D printing parameters of short carbon fiber reinforced polymer CFRP on the mechanical and failure performance: Review and future perspective," *Next Materials*, vol. 8, p. 100645, Jul. 2025, doi: 10.1016/J.NXMATE.2025.100645.

[172] H. Li *et al.*, "Interlayer enhancement of 3D printed CF/PLA composites via localized microwave welding and annealing-induced crystallization," *Compos. B Eng.*, vol. 284, p. 111737, Sep. 2024, doi: 10.1016/J.COMPOSITESB.2024.111737.

[173] H. Dong, H. Wang, P. J. Hazell, N. Sun, H. B. Dura, and J. P. Escobedo-Diaz, "Effects of printing parameters on the quasi-static and dynamic compression behaviour of 3D-printed re-entrant auxetic structures," *Thin-Walled Structures*, vol. 210, p. 113000, May 2025, doi: 10.1016/J.TWS.2025.113000.

[174] T. Wang, L. Wang, Z. Ma, and G. M. Hulbert, "Elastic analysis of auxetic cellular structure consisting of re-entrant hexagonal cells using a strain-based expansion homogenization method," *Mater. Des.*, vol. 160, pp. 284–293, Dec. 2018, doi: 10.1016/J.MATDES.2018.09.013.

[175] W. T. Nugroho, Y. Dong, A. Pramanik, M. Chithirai Pon Selvan, Z. Zhang, and S. Ramakrishna, "Additive manufacturing of re-entrant structures: Well-tailored structures, unique properties, modelling approaches and real applications," *Addit. Manuf.*, vol. 78, p. 103829, Sep. 2023, doi: 10.1016/J.ADDMA.2023.103829.

[176] M. H. Fu, O. T. Xu, L. L. Hu, and T. X. Yu, "Nonlinear shear modulus of re-entrant hexagonal honeycombs under large deformation," *Int. J. Solids Struct.*, vol. 80, pp. 284–296, Feb. 2016, doi: 10.1016/J.IJSOLSTR.2015.11.015.

[177] N. K. Choudhry, B. Panda, and S. Kumar, “In-plane energy absorption characteristics of a modified re-entrant auxetic structure fabricated via 3D printing,” *Compos. B Eng.*, vol. 228, p. 109437, Jan. 2022, doi: 10.1016/J.COMPOSITESB.2021.109437.

[178] E. O. Momoh *et al.*, “A state-of-the-art review on the application of auxetic materials in cementitious composites,” *Thin-Walled Structures*, vol. 196, p. 111447, Mar. 2024, doi: 10.1016/J.TWS.2023.111447.

[179] X. C. Teng *et al.*, “A simple 3D re-entrant auxetic metamaterial with enhanced energy absorption,” *Int. J. Mech. Sci.*, vol. 229, pp. 1–13, Sep. 2022, doi: 10.1016/J.IJMECSCI.2022.107524.

[180] H. Dong and L. Chang, “The effects of printing directions on the compression behavior of the Re-entrant structure produced by 3D printing technology,” *J. Micromech. Mol. Phys.*, vol. 6, no. 2, 2021, doi: 10.1142/S2424913021410046.

[181] J. A. Travieso-Rodriguez, R. Jerez-Mesa, J. Llumà, O. Traver-Ramos, G. Gomez-Gras, and J. J. R. Rovira, “Mechanical Properties of 3D-Printing Polylactic Acid Parts subjected to Bending Stress and Fatigue Testing,” *Materials*, vol. 12, no. 23, p. 3859, Dec. 2019, doi: 10.3390/MA12233859.

[182] R. V. Pazhamannil, H. M. Hadidi, A. Edacherian, and G. Puthumana, “Prediction of the mechanical properties of heat-treated fused filament fabrication thermoplastics using adaptive neuro-fuzzy inference system,” *Journal of Thermoplastic Composite Materials*, vol. 37, no. 4, pp. 1385–1406, Apr. 2024, doi: 10.1177/08927057231195610/ASSET/280196B2-22A2-45A9-9B35-99B10C1A333D/ASSETS/IMAGES/LARGE/10.1177_08927057231195610-FIG10.JPG.

[183] S. J. Park, J. E. Lee, J. Park, N. K. Lee, Y. Son, and S. H. Park, “High-temperature 3D printing of polyetheretherketone products: Perspective on industrial manufacturing applications of super engineering plastics,” *Mater. Des.*, vol. 211, p. 110163, Dec. 2021, doi: 10.1016/J.MATDES.2021.110163.

[184] “KetaSpire ® PEEK Design & Processing Guide KetaSpire ® KetaSpire® PEEK Design and Processing Guide Introduction and Typical Properties”.

[185] “ISO 527-1:2019 - Plastics — Determination of tensile properties — Part 1: General principles.” Accessed: Jan. 26, 2026. [Online]. Available: https://www.iso.org/standard/527-1

[186] “Test Method for Compressive Properties of Rigid Plastics,” Aug. 2023, doi: 10.1520/D0695-23.

[187] M. Nikonovich, J. F. S. Costa, A. C. Fonseca, A. Ramalho, and N. Emami, “Structural, thermal, and mechanical characterisation of PEEK-based composites in cryogenic temperature,” *Polym. Test.*, vol. 125, p. 108139, Aug. 2023, doi: 10.1016/J.POLYMERTESTING.2023.108139.

[188] S. K. Ray, A. Banerjee, B. K. Bhangi, D. Pyne, and B. Dutta, “Tribological analysis—general test standards,” *Tribology of Polymers, Polymer Composites, and Polymer Nanocomposites*, pp. 17–50, Jan. 2023, doi: 10.1016/B978-0-323-90748-4.00001-7.

[189] I. Tulpan, S. Halevi, A. Shirizly, and G. Katarivas Levy, “Beyond layered limitations: A novel multi-thermal optimization framework of 3D-printed short carbon fiber-reinforced polyether-ether-ketone (SCF-PEEK),” *Compos. Part A Appl. Sci. Manuf.*, vol. 196, p. 108948, Sep. 2025, doi: 10.1016/J.COMPOSITESA.2025.108948.

[190] J. Butt, R. Bhaskar, J. Butt, and R. Bhaskar, “Investigating the Effects of Annealing on the Mechanical Properties of FFF-Printed Thermoplastics,” *Journal of Manufacturing and Materials Processing 2020, Vol. 4,* vol. 4, no. 2, Apr. 2020, doi: 10.3390/JMMP4020038.

[191] W. Yu, X. Wang, X. Yin, E. Ferraris, and J. Zhang, “The effects of thermal annealing on the performance of material extrusion 3D printed polymer parts,” *Mater. Des.*, vol. 226, p. 111687, Feb. 2023, doi: 10.1016/J.MATDES.2023.111687.

[192] X. Tardif *et al.*, “Experimental study of crystallization of PolyEtherEtherKetone (PEEK) over a large temperature range using a nano-calorimeter,” *Polym. Test.*, vol. 36, pp. 10–19, Jun. 2014, doi: 10.1016/J.POLYMERTESTING.2014.03.013.

[193] M. Cristea, D. Ionita, and M. M. Iftime, “Dynamic Mechanical Analysis Investigations of PLA-Based Renewable Materials: How Are They Useful?,” *Materials*, vol. 13, no. 22, p. 5302, Nov. 2020, doi: 10.3390/MA13225302.

[194] A. Ghasemkhani, G. Pircheraghi, N. Rashidi Mehrabadi, and A. Eshraghi, “Effects of heat treatment on the mechanical properties of 3D-printed polylactic acid: Study of competition between crystallization and interlayer bonding,” *Mater. Today Commun.*, vol. 39, p. 109266, Jun. 2024, doi: 10.1016/J.MTCOMM.2024.109266.

[195] I. Vindokurov, Y. Pirogova, M. Tashkinov, and V. V. Silberschmidt, “Effect of Heat Treatment on Elastic Properties and Fracture Toughness of Fused Filament Fabricated PEEK for Biomedical Applications,” *Polymers 2022, Vol. 14, Page 5521*, vol. 14, no. 24, p. 5521, Dec. 2022, doi: 10.3390/POLYM14245521.

[196] E. de Avila, J. Eo, J. Kim, and N. P. Kim, “Heat Treatment Effect on Mechanical Properties of 3D Printed Polymers,” *MATEC Web of Conferences*, vol. 264, p. 02001, 2019, doi: 10.1051/MATECCONF/201926402001.

[197] Y. Deng, L. Chang, Y. Deng, and L. Chang, “Effects of Post-Heat Treatment on Mechanical and Tribological Properties of 3D-Printed PLA and PEEK Structures,” *Polymers 2026, Vol. 18,* vol. 18, no. 2, p. 253, Jan. 2026, doi: 10.3390/POLYM18020253.

[198] J. Zhang, G. Lu, Z. Wang, D. Ruan, A. Alomarah, and Y. Durandet, “Large deformation of an auxetic structure in tension: Experiments and finite element

analysis," *Compos. Struct.*, vol. 184, pp. 92–101, Jan. 2018, doi: 10.1016/J.COMPSTRUCT.2017.09.076.

[199] B. Ling, K. Wei, Z. Wang, X. Yang, Z. Qu, and D. Fang, "Experimentally program large magnitude of Poisson's ratio in additively manufactured mechanical metamaterials," *Int. J. Mech. Sci.*, vol. 173, p. 105466, May 2020, doi: 10.1016/J.IJMECSCI.2020.105466.

[200] Q. Zhang *et al.*, "Analysis of friction-induced vibration and wear characteristics during high-speed train friction braking process," *Tribol. Int.*, vol. 196, p. 109701, Aug. 2024, doi: 10.1016/J.TRIBOINT.2024.109701.

[201] M. M. John, M. Hanief, and M. J. Khan, "An approach to correlate friction-induced noise with coefficient of friction," *Tribol. Int.*, vol. 201, p. 110253, Jan. 2025, doi: 10.1016/J.TRIBOINT.2024.110253.

[202] A. D. Dimarogonas, "Vibration of cracked structures: A state of the art review," *Eng. Fract. Mech.*, vol. 55, no. 5, pp. 831–857, Nov. 1996, doi: 10.1016/0013-7944(94)00175-8.

[203] N. K. Myshkin, M. I. Petrokovets, and A. V. Kovalev, "Tribology of polymers: Adhesion, friction, wear, and mass-transfer," *Tribol. Int.*, vol. 38, no. 11–12, pp. 910–921, Nov. 2005, doi: 10.1016/J.TRIBOINT.2005.07.016.

[204] I. Tzanakis, M. Conte, M. Hadfield, and T. A. Stolarski, "Experimental and analytical thermal study of PTFE composite sliding against high carbon steel as a function of the surface roughness, sliding velocity and applied load," *Wear*, vol. 303, no. 1–2, pp. 154–168, Jun. 2013, doi: 10.1016/J.WEAR.2013.02.011.

[205] Y. Wang and F. Yan, "Tribological properties of transfer films of PTFE-based composites," *Wear*, vol. 261, no. 11–12, pp. 1359–1366, Dec. 2006, doi: 10.1016/J.WEAR.2006.03.050.

[206] J. F. Archard and R. A. Rowntree, "The temperature of rubbing bodies; part 2, the distribution of temperatures," *Wear*, vol. 128, no. 1, pp. 1–17, Nov. 1988, doi: 10.1016/0043-1648(88)90249-9.

[207] M. C. McC. Ettles, "Heat Generation and Friction in Rotating Bands," *ASLE TRANSACTIONS*, vol. 29, no. 3, pp. 312–320, 1986, doi: 10.1080/05698198608981691.

[208] B. Bhushan, "Modern Tribology Handbook, Two Volume Set," *Modern Tribology Handbook, Two Volume Set*, Dec. 2000, doi: 10.1201/9780849377877/MODERN-TRIBOLOGY-HANDBOOK-TWO-VOLUME-SET-BHARAT-BHUSHAN.

[209] L. Chang, Z. Zhang, H. Zhang, and A. K. Schlarb, "On the sliding wear of nanoparticle filled polyamide 66 composites," *Compos. Sci. Technol.*, vol. 66, no. 16, pp. 3188–3198, Dec. 2006, doi: 10.1016/J.COMPSCITECH.2005.02.021.

[210] S. V. Panin, L. A. Kornienko, V. O. Alexenko, D. G. Buslovich, S. A. Bochkareva, and B. A. Lyukshin, “Increasing Wear Resistance of UHMWPE by Loading Enforcing Carbon Fibers: Effect of Irreversible and Elastic Deformation, Friction Heating, and Filler Size,” *Materials 2020, Vol. 13, Page 338*, vol. 13, no. 2, p. 338, Jan. 2020, doi: 10.3390/MA13020338.

[211] S. V. Panin, J. Luo, D. G. Buslovich, V. O. Alexenko, F. Berto, and L. A. Kornienko, “Effect of Transfer Film on Tribological Properties of Anti-Friction PEI- and PI-Based Composites at Elevated Temperatures,” *Polymers (Basel).*, vol. 14, no. 6, Mar. 2022, doi: 10.3390/POLYM14061215.

[212] M. Odrobina, T. Deák, L. Székely, T. Mankovits, R. Z. Keresztes, and G. Kalácska, “The Effect of Crystallinity on the Toughness of Cast Polyamide 6 Rods with Different Diameters,” *Polymers (Basel).*, vol. 12, no. 2, p. 293, Feb. 2020, doi: 10.3390/POLYM12020293.

[213] W. Lv, P. Yu, and D. Li, “An energy dissipation metamaterial based on Coulomb friction and vibration,” *Int. J. Mech. Sci.*, vol. 263, p. 108764, Feb. 2024, doi: 10.1016/J.IJMECSCI.2023.108764.

[214] A. Gnatowski, R. Golebski, P. Sikora, J. Petru, and J. Hajnys, “Analysis of the Impact of Changes in Thermomechanical Properties of Annealed Semi-Crystalline Plastics on the Surface Condition after the Machining Process,” *Materials 2023, Vol. 16, Page 4816*, vol. 16, no. 13, p. 4816, Jul. 2023, doi: 10.3390/MA16134816.

[215] M. A. ; M. A. ; Baig *et al.*, “A Comprehensive Review on the Tribological Evaluation of Polyether Ether Ketone Pristine and Composite Coatings,” *Polymers 2024, Vol. 16, Page 2994*, vol. 16, no. 21, p. 2994, Oct. 2024, doi: 10.3390/POLYM16212994.

[216] J. Ye, D. L. Burris, and T. Xie, “A Review of Transfer Films and Their Role in Ultra-Low-Wear Sliding of Polymers,” *Lubricants 2016, Vol. 4, Page 4*, vol. 4, no. 1, p. 4, Feb. 2016, doi: 10.3390/LUBRICANTS4010004.

[217] S. Yuan *et al.*, “In situ experimental study on the synergistic strengthening and toughening mechanisms of multiple pore structures in deer antler,” *Mater. Des.*, vol. 224, p. 111306, Dec. 2022, doi: 10.1016/J.MATDES.2022.111306.

[218] Q. A. Liu, Z. Y. Xiang, J. L. Mo, Q. X. Zhang, and Y. G. Zhu, “The effects of the structural stiffness of vibration transfer path on friction-induced vibration and noise,” *Tribol. Int.*, vol. 173, p. 107687, Sep. 2022, doi: 10.1016/J.TRIBOINT.2022.107687.

[219] G. M. Lin, G. Y. Xie, G. X. Sui, and R. Yang, “Hybrid effect of nanoparticles with carbon fibers on the mechanical and wear properties of polymer composites,” *Compos. B Eng.*, vol. 43, no. 1, pp. 44–49, Jan. 2012, doi: 10.1016/J.COMPOSITESB.2011.04.029.

[220] V. Shanmugam, K. Babu, G. Kannan, R. A. Mensah, S. K. Samantaray, and O. Das, “The thermal properties of FDM printed polymeric materials: A review,” *Polym.*

Degrad. Stab., vol. 228, p. 110902, Oct. 2024, doi: 10.1016/J.POLYMDEGRADSTAB.2024.110902.

[221] M. Alhendi *et al.*, "Printed electronics for extreme high temperature environments," *Addit. Manuf.*, vol. 54, p. 102709, Jun. 2022, doi: 10.1016/J.ADDMA.2022.102709.

[222] L. Wang *et al.*, "Advances in polymers and composite dielectrics for thermal transport and high-temperature applications," *Compos. Part A Appl. Sci. Manuf.*, vol. 164, p. 107320, Jan. 2023, doi: 10.1016/J.COMPOSITESA.2022.107320.

[223] A. Jean-Fulcrand, M. A. Masen, T. Bremner, and J. S. S. Wong, "Effect of temperature on tribological performance of polyetheretherketone-polybenzimidazole blend," *Tribol. Int.*, vol. 129, pp. 5–15, Jan. 2019, doi: 10.1016/J.TRIBOINT.2018.08.001.

[224] C. Dong, C. Yuan, X. Bai, H. Qin, and X. Yan, "Investigating relationship between deformation behaviours and stick-slip phenomena of polymer material," *Wear*, vol. 376–377, pp. 1333–1338, Apr. 2017, doi: 10.1016/J.WEAR.2017.01.061.

[225] V. Slavković, B. Hanželič, V. Plesec, S. Milenković, and G. Harih, "Thermo-Mechanical Behavior and Strain Rate Sensitivity of 3D-Printed Polylactic Acid (PLA) below Glass Transition Temperature (Tg)," *Polymers (Basel).*, vol. 16, no. 11, p. 1526, Jun. 2024, doi: 10.3390/POLYM16111526/S1.

[226] R. Maier, A. M. Istrate, A. Despa, A. C. Mandoc, S. Bucaciuc, and R. Stoica, "Investigation into Thermomechanical Response of Polymer Composite Materials Produced through Additive Manufacturing Technologies," *Materials 2022, Vol. 15, Page 5069*, vol. 15, no. 14, p. 5069, Jul. 2022, doi: 10.3390/MA15145069.

[227] T. R. Giri and R. W. Mailen, "Thermomechanical behavior of polymeric periodic structures," *Addit. Manuf.*, vol. 49, p. 102512, Jan. 2022, doi: 10.1016/J.ADDMA.2021.102512.

[228] Z. Liu *et al.*, "Mechanistic Study on Rheological, Thermal, and Shape Memory Properties of Polyester-Type and Polyether-Type PLA/TPU Composites for 4D Printing," *Polym. Adv. Technol.*, vol. 36, no. 9, p. e70346, Sep. 2025, doi: 10.1002/PAT.70346.

[229] Z. Issabayeva and I. Shishkovsky, "Prediction of The Mechanical Behavior of Polylactic Acid Parts with Shape Memory Effect Fabricated by FDM," *Polymers (Basel).*, vol. 15, no. 5, p. 1162, Mar. 2023, doi: 10.3390/POLYM15051162/S1.

[230] H. Cao *et al.*, "Differences in adhesive wear mechanisms of soft/hard materials caused by varying loads during the friction process," *Tribol. Int.*, vol. 214, p. 111157, Feb. 2026, doi: 10.1016/J.TRIBOINT.2025.111157.

[231] S. Ravichandran, E. Vengatesan, and A. Ramakrishnan, "Synthesis and dynamic mechanical analysis of fiber reinforced low-density polyethylene hybrid polymer composites," *Mater. Today Proc.*, vol. 27, pp. 177–180, Jan. 2020, doi: 10.1016/J.MATPR.2019.09.216.

[232] S. V. Panin, J. Luo, D. G. Buslovich, V. O. Alexenko, F. Berto, and L. A. Kornienko, “Effect of Transfer Film on Tribological Properties of Anti-Friction PEI- and PI-Based Composites at Elevated Temperatures,” *Polymers (Basel).*, vol. 14, no. 6, p. 1215, Mar. 2022, doi: 10.3390/POLYM14061215.